ABSTRACT

Title of Document:	HIGH PRESSURE REDOX GEOCHEMISTRY OF TUNGSTEN IN METAL–SILICATE SYSTEMS: IMPLICATIONS FOR CORE FORMATION IN THE EARTH
	Gregory Allen Shofner, Ph.D., 2011
Directed By:	Adjunct Associate Professor, Andrew J. Campbell, Department of Geology

Geochemical models of core formation are commonly based on core and mantle abundances of siderophile elements. Because of the affinity of these elements for metallic phases, they are thought to be highly concentrated in Earth's core. Tungsten is a moderately siderophile element that may provide constraints on the pressure, temperature, composition, and oxygen fugacity conditions, and on the timing of core formation in the Earth. Previous experimental studies suggest that pressure exerts little influence over tungsten metal/silicate partitioning up to 20 gigapascals (GPa). But, core formation models, based on W, predict metal–silicate equilibration pressures outside the available experimental pressure range, thus, requiring extrapolation. Therefore, higher pressure experimental data on tungsten were needed to constrain this important parameter.

High pressure melting experiments were conducted to 50 GPa and 4400 K using a diamond anvil cell, and to 26 GPa and 2500 K using a multi-anvil press. Diamond

anvil cell samples were sectioned using a focused ion beam instrument. The W-WO_2 oxygen fugacity buffer was characterized to high pressure, also using diamond anvil cells and a multi-anvil press, combined with synchrotron x-ray diffraction. Combining the high pressure W-WO_2 oxygen fugacity buffer and the database of metal/silicate partitioning data, a new approach was taken to model the Fe-W exchange reaction. Compared to the common linear method of parameterizing metal-silicate partitioning data, this approach captures the non-linear pressure dependence on oxygen fugacity, and allows for modeling of the excess Gibbs energy of mixing based on the activity ratios of Fe, FeO, W, and WO_2.

Applying this non-linear parameterization to the problem of core formation in the Earth, a pressure–temperature solution of 38 GPa and 3100 K in a peridotite silicate composition for a single-stage, magma ocean core formation model was determined that constrains equilibrium core formation conditions in the Earth. This solution was further constrained by Ni, Co, and Mo parameterizations from the literature. The pressure and temperature conditions of this solution represents a combination of the averaged effects of a deepening magma ocean through time and the "Moon-forming" impact.

HIGH PRESSURE REDOX GEOCHEMISTRY OF TUNGSTEN IN METAL–SILICATE SYSTEMS: IMPLICATIONS FOR CORE FORMATION IN THE EARTH

By

Gregory Allen Shofner

Dissertation submitted to the Faculty of the Graduate School of the
University of Maryland, College Park, in partial fulfillment
of the requirements for the degree of
Doctor of Philosophy
2011

Advisory Committee:
Professor Richard J. Walker, Chair
Adjunct Associate Professor Andrew J. Campbell
Assistant Professor Saswata Hier-Majumder
Associate Research Scientist Philip M. Piccoli
Associate Professor Derek C. Richardson (Dean's Representative)

Dedication

I dedicate this dissertation to my wife Leslie. For the nine years we have been together, you have been a constant source of Love, Friendship, Happiness, Support and Encouragement. As I have said many times before, I would not be the person that I am today without you in my life, and the world is a better place because you are in it. I would not have achieved what I have, either academically or personally, without you. You have dealt with my temperament and the particular form of insanity that accompanies working on a graduate degree project and paper…twice in fact, first for the masters and now for the doctorate! And, to our son Matthew whom has born the greatest brunt of this adventure. I love you both as I love no others, and welcome our future together.

I offer dedication to my family. To my parents, who gave me life and who instilled in me the values that have guided me, and encouraged me to find my own path and achieve my goals, whatever they may be. To my parents-in-law, who have accepted me into their lives as part of the family and loved me as one of their own…even though I have still learned so little Spanish!

“I must not fear. Fear is the mind-killer. Fear is the little-death that brings total obliteration. I will face my fear. I will permit it to pass over me and through me. And when it has gone past I will turn the inner eye to see its path. Where the fear has gone there will be nothing. Only I will remain."

-The Bene Gesserit Littany against Fear, © 1965 Herbert Properties LLC.

Acknowledgements

I gratefully and sincerely acknowledge the NASA Graduate Student Researchers Program and the National Science Foundation for financial support of my doctoral research.

Andy Campbell is the best advisor I could have asked for. He has been infinitely patient with me, both in terms of the learning curves I faced coming to high pressure research from the low pressure world of surficial geology and in the challenges of having a family in the midst of doctoral research. I thank you for the doors you have opened for me that I never thought I would pass through.

I thank Kevin Righter, Lisa Danielson, and Zia Rahman at NASA for their patience and contributions to my work at Johnson Space Center doing research in the High-Pressure Petrology and FIB Laboratories.

To Phil Piccoli whose diligence, guidance, and patience provided me with the analytical data on my samples, without which my project would not have been possible.

I would not have been in this doctoral program without the recommendations of Steven Esling (SIUC), H. Wayne Leimer (TTU), and Jim Miner (ISGS), all of whom contributed to my development in the prior stages of my academic and professional careers.

Table of Contents

Dedication ii
Acknowledgements iii
Table of Contents iv
List of Tables vi
List of Figures vii
List of Appendices x
1 Introduction 1
1.1 Planetary Core Formation 1
1.2 Partitioning of Moderately Siderophile Elements 3
1.3 Constraints on Core Formation Conditions 5
1.4 Timing of Core Formation 9
1.5 Previous Experimental Work 11
1.5.1 Moderately Siderophile Elements 11
1.5.2 Tungsten 11
1.6 Oxygen Fugacity Buffers 15
1.6.1 Iron–wüstite 15
1.6.2 Tungsten–tungsten-dioxide 16
1.7 Present Experimental Work 17
1.8 Hypothesis 18
2 Experimental and Analytical Methods 19
2.1 Multi-anvil Press (MAP) 21
2.1.1 Sample Capsule Compositions 23
2.1.2 Sample Recovery and Preparation for Analysis 25
2.2 Laser-heated Diamond Anvil Cell (LHDAC) 27
2.2.1 Sample Loading and Pressure Media 27
2.2.2 Laser Heating 29
2.2.3 Temperature Measurement 31
2.2.4 Pressure Measurement 35
2.2.5 Sample Recovery and Preparation for Analysis 35
2.3 Piston Cylinder Press (PC) 37
2.4 Focused Ion Beam (FIB) 37
2.4.1 Locating the Region of Interest 40
2.5 Electron Microprobe 41
2.5.1 Analytical Element Suite 49
2.5.2 Standardization 49
2.5.3 LHDAC Samples 50
2.6 Synchrotron X-ray Diffraction 51
2.6.1 Room Temperature Compression 52
2.6.2 High Temperature Experiments 53
3 Metal/Silicate Partitioning of Tungsten 58
3.1 Experimental Results 58
3.1.1 Multi-anvil Press (MAP) 59

3.1.2 Laser-heated Diamond Anvil Cell (LHDAC) 64
3.1.3 Piston Cylinder (PC) 68
3.2 Partition Coefficients 74
3.3 Tungsten Valence in Silicate Melts 78
3.3.1 Estimating Tungsten Valence 78
3.3.2 Measurements of Tungsten Valence 80
3.4 Activities in Silicate and Metallic Melts 81
3.4.1 Carbon in Fe Metal Alloys 82
3.4.2 Modeling Approaches 83
3.5 Data Analysis 84
3.5.1 Activity Correction in Metals 84
3.5.2 Regressions 87
4 The W-WO_2 Buffer System 95
4.1 Data Analysis 95
4.1.1 Unit-cell Determinations 96
4.1.2 Peak Indexing 97
4.1.3 Phase Transitions in WO_2 113
4.2 Equations of State 118
4.2.1 Pressure Calibration 120
4.3 The W-WO_2 Oxygen Fugacity Buffer (WWO) 124
4.3.1 Polynomial Expression of fO_2 127
4.3.2 Relationship to Iron-wustite 128
4.3.3 Application to W Metal/silicate Partitioning 131
5 Core Formation Modeling 135
5.1 Modeling Approach 136
5.2 Models 139
5.2.1 Model M1 142
5.2.2 Model M2 144
5.2.3 Model M3 145
5.3 Implications of Models 147
6 Conclusions 150
Appendices 153
Appendix A: Additional LHDAC Sample Images 153
References 156

List of Tables

Table 1. Experimental conditions in metal/silicate partitioning experiments.....20

Table 2. Composition of starting material powder mixtures for MAP, LHDAC, and PC experiments. Quantities are weight percents of the indicated components or of total powder mixtures.....21

Table 3. Electron microprobe element suites, associated standards, and peak and background count times. 43

Table 4. Compositions of silicate phases as measured using electron microprobe.....44

Table 5. Compositions of metals as measured using electron microprobe.....47

Table 6. Experimental phases, oxygen fugacities, molar partition and exchange coefficients. 63

Table 7. Regression coefficients for parameterizations of W metal/silicate partitioning. 89

Table 8. Lattice parameters, volumes, and densities of W in x-ray diffraction experiments.....99

Table 9. Lattice parameters, volumes, and densities of WO_2 phases in x-ray diffraction experiments.....105

Table 10. Lattice parameters and unit-cell volumes of WC in x-ray diffraction experiments 113

Table 11. Fit parameters for P-V-T equations of state. 119

Table 12. Parameters of polynomial fits of tabulated fO_2 values for *$P2_1/c$*, *Pnma*, and *P2/m* WO_2 phases in high pressure W-WO_2 oxygen fugacity buffer.....128

Table 13. Fit parameter for the excess Gibbs energy of mixing in the W-WO_2 buffer-based expression of the Fe-W exchange coefficient. 132

Table 14. Effective metal/silicate partition coefficients and Fe-element exchange coefficients for equilibrium core formation based on bulk silicate Earth and core abundances for W, Ni, Co, and Mo 141

List of Figures

Figure 1. Siderophile element composition of the Earth's upper mantle, shown as CI and refractory element relative depletions 6

Figure 2. Tungsten metal/silicate partitioning data from literature, plotted as a function of pressure 9

Figure 3. Tungsten metal/silicate partitioning data from literature, plotted as functions of temperature, fO_2, and silicate composition 13

Figure 4. Schematics of COMPRES standardized multi-anvil press assemblies. 22

Figure 5. Cube assembly components, components of MAP cell, and position within 880-ton press at NASA Johnson Space Center. 23

Figure 6. Backscattered electron image of MAP sample GN13, showing extensive growth of ferropericlase with interstitial melt 25

Figure 7. Schematic of diamond anvil cell. 28

Figure 8. Transmitted light images of representative LHDAC samples 31

Figure 9. Two-dimensional temperature map derived from the thermal emission images shown at bottom 32

Figure 10. Backscattered electron images illustrating the process of sectioning LHDAC sample G36c using FIB 40

Figure 11. Analytical transects using microprobe on FIB-sectioned LHDAC sample G39, shown in backscattered electron image 50

Figure 12. Pressure and temperature distributions of x-ray diffraction experiments 51

Figure 13. Resistive external heater for DAC 56

Figure 14. Experimental P-T space of metal/silicate partitioning experiments 58

Figure 15. Back scattered electron images of MAP sample GN24 62

Figure 16. Reflected light image of MAP sample GN10 63

Figure 17. LHDAC sample G36c 67

Figure 18. Backscattered electron image of PC sample GPC2. 69

Figure 19. Evaluation of Henry's Law behavior in W metal/silicate experiments with weight percent level W doping in starting materials 71

Figure 20. Backscattered electron image of PC sample GPC7 72

Figure 21. Molar metal/silicate partition coefficients calculated from experiments to assess completion of metal–silicate reaction using both WO_2 and W metal in starting materials. 73

Figure 22. Plot of W metal/silicate molar partition coefficients from experiments in this study, with no corrections for T, fO2, or melt compositions applied. 75

Figure 23. Tungsten metal/silicate molar partition coefficients for this study, with temperature and fO2 corrections applied as discussed in the text. 77

Figure 24. Tungsten metal/silicate molar partition coefficients for this study fitted against log fO2, with no corrections for temperature, pressure, or silicate or metallic melt composition applied 79

Figure 25. Difference plots for experiments with carbon-bearing metals 86

Figure 26. Regression R1 plotted on the peridotite liquidus. 90

Figure 27. Regression R1 along isotherms and isobars 91

Figure 28. Regressions R2 and R1 plotted on the peridotite liquidus 93

Figure 29. Regression R3 plotted on the peridotite liquidus. 94

Figure 30. An example x-ray diffraction image for pattern G33_006 collected on CCD detector 96

Figure 31. X-ray diffraction spectrum showing G33_006 and a calculated pattern for the *Pnma* structure of WO_2 described by Sundberg et al. (1994) 104

Figure 32. X-ray diffraction spectrum showing patterns G33_006 and G33_022 ... 109

Figure 33. Structure models of WO_2: monoclinic, space group $P2_1/c$ (Bolzan et al., 1995), stable form at ambient conditions; and orthorhombic, space group *Pnma* (Sundberg et al., 1994), high pressure and temperature phase 110

Figure 34. X-ray diffraction spectra from highest temperature pattern at each pressure range 117

Figure 35. Phase diagram for WO_2 118

Figure 36. PVT EOS for WO_2 plotted along isotherms as a function of pressure 121

Figure 37. PVT EOS for W plotted along isotherms as a function of pressure. 123

Figure 38. Log of the absolute fO_2 of the WWO buffer plotted as a function of inverse temperature and pressure 126

Figure 39. Difference between WWO and IW buffers plotted versus inverse temperature and pressure 130

Figure 40. The predicted W metal/silicate partitioning in terms of the log of the Fe-W exchange coefficient calculated along the peridotite liquidus (Wade and Wood, 2005) 133

Figure 41. Isothermal and isobaric plots of the predicted W metal/silicate partitioning in terms of the log of the Fe-W exchange coefficient 134

Figure 42. Model M1 for constraining equilibrium core formation conditions 143

Figure 43. Model M2 for constraining equilibrium core formation conditions 145

Figure 44. Model M3 for constraining equilibrium core formation conditions 146

Figure A-1. Backscattered electron images showing obverse sides of LHDAC sample G34 153
Figure A-2. Temperature map showing radial temperature distribution of LHDAC sample G34 153
Figure A-3. Backscattered electron and secondary electron images of LHDAC sample G38a 154
Figure A-4. Backscattered electron images showing obverse sides of LHDAC sample G38b 155

List of Appendices

Appendix A: Additional LHDAC Sample Images.....153

1 Introduction

1.1 Planetary Core Formation

The Earth possesses a metallic core surrounded by a silicate mantle. This core–mantle configuration is accepted to be the result of the segregation between metal and silicate fractions early in planetary formation (Righter and Drake, 1996; Drake, 2000; Walter and Trønnes, 2004; Wood, 2008). Multiple models of core formation have been put forth over many decades (Wänke and Gold, 1981; Stevenson, 1981; Jones and Drake, 1986; Wänke and Dreibus, 1988; Rubie et al., 2003; Wood, 2008; and Rubie et al., 2011). In broadest terms, these models range from simple single-stage to more complex multi-stage scenarios. The foundation of all models is the segregation of metal from silicate, a process that formed the Earth's core, and the conditions necessary to explain the observed element abundances in the Earth's mantle.

How this metal-silicate segregation occurred remains a matter of debate and has led models that have include various aspects of: the mode of accretion, composition of the accreted materials, equilibrium vs. non-equilibrium segregation, and the pressure, temperature, and oxygen fugacity conditions at which segregation occurred. Simple models describe core formation as a single event from accreted materials due to internal processes. More complex models describe core formation that is coincident with accretion, with metal–silicate segregation occurring near the Earth's surface as the materials were accreted. Taking the latter scenario further, more recent models describe

episodes of large-scale melting of the silicate Earth, primarily due to large impacts with impactor sizes nearly half that of the proto Earth (Stevenson, 2008), leading to periods of so-called magma oceans. The "magma ocean" model has become widely accepted though variations of the model include different modes of metal-silicate segregation, i.e. regarding where segregation occurred and the extent of equilibration between metal and silicate phases (Walter et al., 2000; Wade and Wood, 2005; Righter, 2011; and Rubie et al., 2011). Common to many models is the process where small droplets of metal segregate within the molten Earth and gravitationally descend (Stevenson, 1990), and whether they equilibrate during descent (Rubie et al., 2003) or at the base of a magma ocean as ponded metals. All debated models indicate that large metal diapirs ultimately formed and further descended through solid or mostly solid silicate to form the metallic core.

Interplaying with the basic mode of core formation is the question of homogenous vs. heterogeneous accretion, i.e. did the materials accreting to form the Earth maintain an essentially fixed composition or did their composition change through the time of Earth's accretion. Righter (2011) argues that homogeneous accretion is a viable model of core formation in the Earth and can be reconciled with geochemical evidence. Wade and Wood (2005) also proposed homogeneous accretion, but also argued that the oxidation state of the Earth increased during accretion and invoked the perovskite disproportionation reaction (Frost et al., 2004) as the oxidation mechanism. Rubie et al. (2011) and Frost et al. (2008) favor heterogeneous accretion, arguing that the increasingly oxidized Earth during accretion cannot be explained exclusively by disproportionation of perovskite, which produces Fe^{3+} and Fe metal from Fe^{2+}.

The behavior of chemical elements during metal–silicate segregation provides insight into planetary differentiation processes. Distribution of elements between metal and silicate regions of planetary interiors result from: the characteristics of those elements; the physical and chemical conditions under which planetary differentiation occurred; and the composition of the original silicate and metal materials.

1.2 Partitioning of Moderately Siderophile Elements

The term siderophile literally means "iron loving", which refers to the affinity of the siderophile elements for Fe metal. The siderophile elements are those that preferentially bond with an Fe-rich metallic phase versus an oxide phase. They are further classified in three subgroups called the slightly, moderately, and highly siderophile elements based on extent of their tendency to bond in the metallic phase.

Application of the moderately siderophile elements to understanding core formation is fundamentally based on the partition coefficient, which is a measure of the balance between an element in coexisting equilibrium phases, in this case between metal and silicate. Determination of metal–silicate partition coefficients allows for calculations of element distributions that can be compared to accepted values of element abundances in the silicate (mantle) and metallic (core) portions of the Earth (Righter, 2003; Wade and Wood, 2005).In the simplest form, the partition coefficient is

$$D = C_M^{met} / C_{MOx}^{sil} \quad (1)$$

where C is the abundance of M as a mass fraction in the metal and silicate phases. Most metal-silicate partitioning literature gives D in terms of weight percents. The partition coefficient can also be calculated using the molar proportions of M in metal and silicate and in this form is termed the molar partition coefficient (Beattie et al., 1993). Cottrell

et al. (2009) defined the molar partition coefficient using the activities of M in metal and silicate.

Considering the generic metal-oxide equilibrium

$$M + \tfrac{x}{2}O_2 \rightleftharpoons MO_x \quad (2)$$

the Gibbs energy difference between *MOx* and *M* is

$$\Delta G_{MMO} = G(MO_x) - G(M) = \tfrac{x}{2} RT \ln f(O_2) \quad (3)$$

This reaction shows the explicit dependence of metal-silicate partitioning on fO_2, and therefore, it is sometimes preferable to cast the partition coefficient in terms of an exchange coefficient K_D. In systems containing Fe, metal-silicate partitioning of metal *M* can be modeled based on the exchange reaction

$$MO_y + yFe = M + yFeO \quad (4)$$

where *y* is the valence of *M*. The exchange coefficient, or exchange partition coefficient, is the quotient of the metal/silicate molar partition coefficients of M and Fe:

$$K_D = D(M) \Big/ D(Fe)^y = \left(X_M^{met} \Big/ X_{MO_y}^{sil}\right) \Big/ \left(X_{Fe}^{met} \Big/ X_{FeO}^{sil}\right)^y \quad (5)$$

where the abundances *X* are the mole fractions of the indicated components. Use of the exchange coefficient eliminates the need for an explicit fO_2 expression in modeling metal-silicate partitioning (Righter, 2003). Application of the exchange coefficient in describing metal-silicate partitioning includes the assumption that the valence of M in the silicate is known under the pressure, temperature and compositional conditions where it is being applied.

1.3 Constraints on Core Formation Conditions

In general, moderately siderophile elements are useful in constraining core formation conditions because they are sensitive to variations in temperature, pressure, oxygen fugacity, and silicate composition. As expected, the observed siderophile abundances in the Earth's mantle are depleted relative to chondritic abundances. However, predicted abundances of some siderophile elements, based on calculations using 1-bar partition coefficients, differ from their observed abundances (Figure 1). This has been described as the "excess siderophile problem". Explanations for this discrepancy have included metal-silicate partition coefficients that are different at higher pressures and temperatures as compared to the 1-bar coefficients, and equilibrium versus disequilibrium processes of metal–silicate segregation during core formation. It is generally accepted that this disparity is due, at least for some elements, to high pressure and temperature partitioning behavior that is not consistent with extrapolation of 1-bar, lower-temperature partition coefficients. (Ringwood, 1966; Capobianco et al., 1993; Righter, 2003; Rubie et al., 2003). The case of the highly siderophile elements (HSE) is the main exception to this explanation. The abundances of the HSE's are highly elevated in the mantle in contrast to their highly siderophile character, and show a remarkably uniform abundance pattern. Both of these aspects of mantle HSE abundances seem best explained by the addition of chondritic composition materials following core formation in what is termed the 'late veneer' (Bottke et al., 2010; and Walker, 2009).

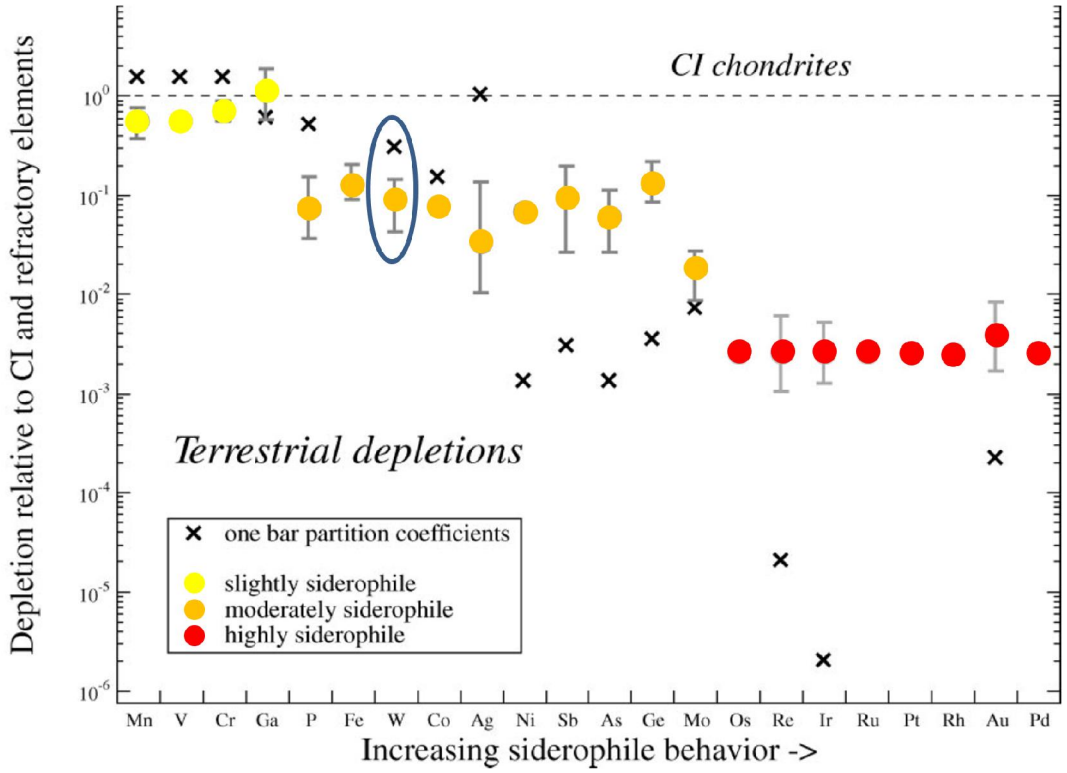

Figure 1. Siderophile element composition of the Earth's upper mantle, shown as CI and refractory element relative depletions. Observed values are shown as filled circles and calculated values using 1-bar partition coeffcients are shown by x's. The location of W is highlighted by a blue ellipse. Plot is from Righter (2003).

Li and Agee (1996) examined the excess siderophile problem through high pressure experimental investigations of Ni, Co, and S. They found that Ni becomes approximately five times less siderophile at 20 GPa, compared to Co, which is about half as siderophile at the same pressure. From this they determined that the near chondritic abundances of Ni and Co can be reconciled if the mantle abundances were set by metal–silicate segregation at a depth of approximately 750 km in a S-rich magma ocean where the pressure was 28 GPa with a temperature range of 2100 to 2400 ºC. Li and Agee (1996) alternatively suggested that their measured partition coefficients could be treated as bulk partition coefficients representative of equilibrium over a range of magma ocean depths, and the 28 GPa value was an average value for the entire mantle.

Righter et al. (1997) also examined partitioning of Ni and Co, along with Mo, W, and P. The thrust of the Righter et al. (1997) study was in presenting parameterizations for partitioning of these siderophile elements that included all available partitioning data, which benefited from the larger number of data points in their statistical analyses. The Righter et al. (1997) parameterizations were intended to account for the various P, T, fO_2, and compositional variation in the metal-silicate partitioning data set, and provided for extrapolation beyond the existing data. Righter et al. (1997) concluded that observed mantle abundances of Ni, Co, P, Mo, and W could be explained by metal–silicate equilibration in a hydrous, S-rich magma ocean at 27 GPa, 2200 K, and just below the iron wüstite (IW) buffer, which are similar conditions to those determined by Li and Agee (1996).

Tungsten is an important element in studies of Earth's formation and core-mantle segregation, because it is both refractory and moderately siderophile. Its refractory character means that it was likely little effected by volatilization in the high temperature conditions of the early Earth. Its siderophile character means that much of the Earth's W is in the core but the extent to which this occurred is dependent upon the P-T-fO_2 conditions of core formation. Several estimates of the abundance of W in the silicate Earth have been made: 29 ppb (McDonough and Sun, 1995), 12 ±3 ppb (Lyubetskaya and Korenaga, 2007), and 13 ±10 ppb (Arevalo and McDonough, 2008). McDonough (2003) and Arevalo and McDonough (2008) have estimated the bulk Earth abundance of W at approximately 170 ppb relative to chondritic proportions. Righter (2011) assumed the bulk Earth abundance of W as chondritic and used the compositions of CI and EH chondrites as probable lower and upper bounds on W abundance, with a range

of 93 to 130 ppb. Based on bulk Earth and silicate Earth abundances of W and a mass distribution of 68% mantle and 32% core, the W abundance in the core can be calculated by mass balance. Using the range of estimated bulk Earth and silicate Earth W abundances listed here, the Earth's core likely contains 260 to 500 ppb W.

Using core and mantle abundances of W, a partition coefficient can be calculated that represents equilibration between core and mantle. Comparison of these partition coefficients to those determined experimentally can provide constraint on equilibrium core formation conditions, assuming a single-stage core formation model. Taking the core and silicate Earth abundances of W as 500 ppb and 12 ppb, respectively, gives a partition coefficient *D* of approximately 40. Using the silicate Earth abundance for W of 29 ppb (McDonough and Sun, 1995) gives a *D* of approximately 16. Using a silicate Earth abundance of 12 ppb and core abundances calculated using CI and EH chondritic W abundances gives a range of *D* of 22 to 32. Published W partition coefficients in the pressure range of 1-bar to 20 GPa vary by two log units at lower pressures with the variation decreasing to one log unit above 10 GPa (Figure 2). This variation represents D values from approximately 25 to 125 above 10 GPa. Therefore, the siderophility of W may remain essentially constant with increasing pressure or must decrease at higher pressure to match the total range in D of 16 to 40 given above for modern core/mantle abundances.

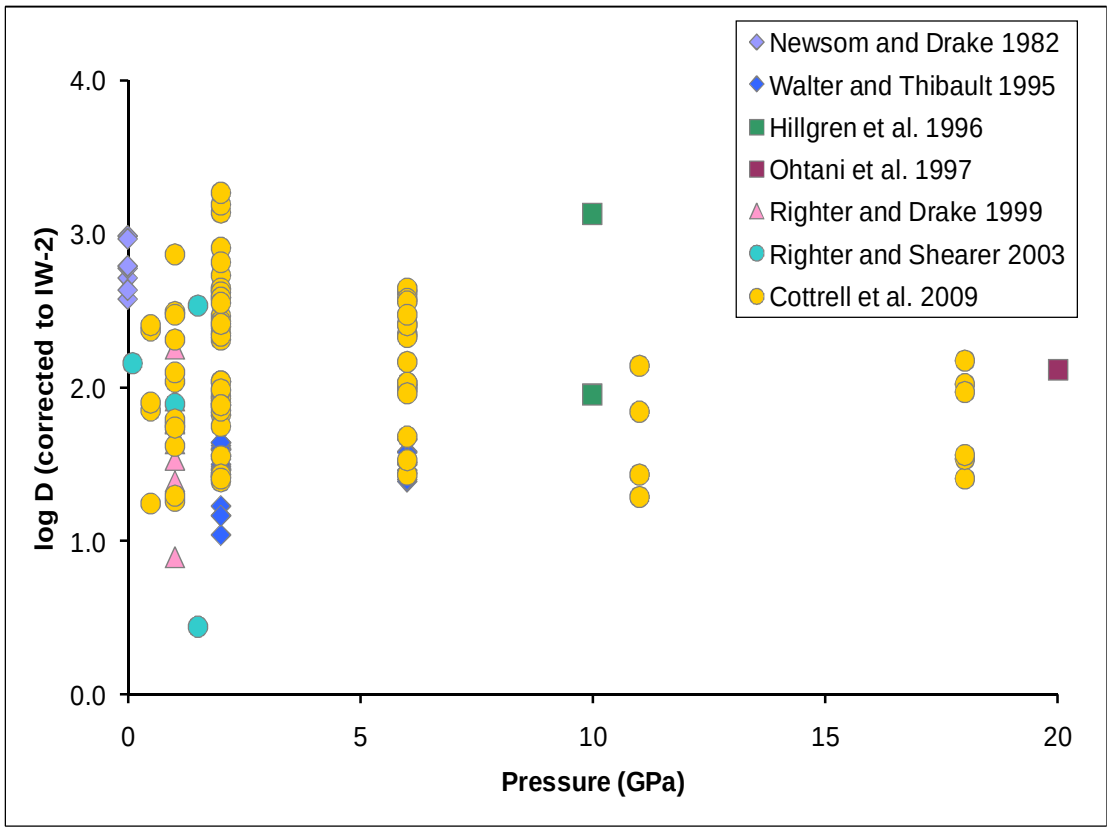

Figure 2. Tungsten metal/silicate partitioning data from literature, plotted as a function of pressure. Partition coefficients were corrected to IW-2 for more meaningful comparison, essentially removing the fO2 influence, though no correction for the influences of temperature and composition were made.

1.4 Timing of Core Formation

Element abundances and partition coefficients provide insight into core formation processes, but they do not constrain timing of core formation. The Hf/W geochronometer is a useful tool for this purpose. This geochronometer is based on the decay of ^{182}Hf to ^{182}W, where the half life of ^{182}Hf is 8.9 million years (Vockenhuber et al. 2004). A basic requirement in applying this geochronometer is that core/mantle segregation occurred within the lifetime of the Hf-W isotopic system, approximately 45 million years.

The principal application of Hf-W to constraining timing of core formation in the Earth is based, in simple terms, on the following model. During core/mantle

segregation, assuming in this case an idealized single-event core formation, Hf exclusively partitions into the silicate mantle due to its lithophile character, and W preferentially partitions into the metal core due to its siderophile character. This partitioning results in a significant depletion of W in the mantle and a corresponding increase in the Hf/W ratio of the mantle relative to the initial ratio. The increased Hf/W ratio results in the gradual production of excess radiogenic ^{182}W relative to chondritic ^{182}W. If core–mantle segregation occurred after Hf-W system extinction, then the $^{182}W/^{183}W$ of the mantle would equal that of chondrites (Lee and Halliday 1995). Analysis of carbonaceous chondrites indicate that the bulk silicate Earth is enriched by approximately 2 ε_W units relative to chondrites, where $\varepsilon_W = [(^{182}W/^{183}W)/(^{182}W/^{184}W) - 1] * 10^4$, suggesting that core–mantle segregation in the Earth occurred within the lifetime of the Hf/W isotopic system (Kleine et al. 2002, Schoenberg et al. 2002, and Yin et al. 2002). Limitations in applying the Hf/W geochronometer include the uncertainty the bulk solar system initial (BSSI) $^{182}Hf/^{180}Hf$ and the Hf/W ratio of the BSE, so that the amount of excess ^{182}W contributed by elevated Hf/W in the Earth can be constrained (Halliday 2003). The fractionation of Hf and W during core formation forms the basis of the applicability of this isotope system, and a refinement of Hf/W as BSE using improved understanding of W partitioning at high pressures may also lead to improvements in defining the timing of terrestrial core formation (Halliday, 2003; Righter and Shearer, 2003).

1.5 Previous Experimental Work

1.5.1 Moderately Siderophile Elements

For more than twenty years, the metal-silicate partitioning behavior of moderately siderophile elements has been explored experimentally. As these investigations progressed, more expansive coverage of temperature, compositional, pressure and fO_2 spaces were explored. Individual studies were often directed toward examining a particular portion of these spaces. (Hilgren et al., 1994; Walter and Thibault, 1995; Li and Agee, 1996; Righter et al., 1997; Ohtani et al., 1997; Jaeger and Drake, 2000; Righter and Shearer, 2003; Cottrell et al., 2009). As already discussed, it became apparent that high pressure exerted various degrees of influence on the partitioning behavior of moderately siderophile elements. Consequently, studies were conducted at increasingly higher pressures. Some elements, such as Ni and Co, have been investigated to higher pressure conditions, up to 80 GPa (Tschauner et al., 1997; Bouhifd and Jephcoat, 2003), whereas W and Mo have been studied to more modest pressure conditions of 20 GPa (Ohtani et al., 1997; Cottrell et al, 2009). The thrust of these investigations was to characterize high pressure and temperature behavior of the moderately siderophile elements so that their observed mantle abundances could be simultaneously reconciled in core formation models.

1.5.2 Tungsten

Tungsten partitioning has been extensively explored experimentally in temperature, compositional, and oxygen fugacity spaces, and to a much lesser extent in pressure space. Much of the previous work on W partitioning has been conducted at 1-

bar conditions or at relatively low pressures, i.e. <=10 GPa (Walter and Thibault, 1995; Hillgren et al., 1996; Righter and Drake, 1999; and O'Neill et al., 2008), and in two studies there are only a few experiments conducted between 10 and 20 GPa (Ohtani et al. 1997; Cottrell 2009). According to these limited data, the strongest influences on the partition coefficient of W are composition, oxygen fugacity, and temperature, with an unresolved influence of pressure. In general, W metal-silicate partitioning increases with increasing temperature, increases with decreasing fO_2, increases in more polymerized melts, and decreases with increasing pressure (Figure 3).

The published W partitioning data exhibit a fair amount of scatter, which is due in large part to the ranges of composition, temperature, fO_2, and pressure conditions in those experiments (Figure 3). To address the scatter in the data, parameterizations have been made to make more sense of the data by characterizing the combined temperature, fO_2, silicate composition, and pressure effects, and allowing for prediction of partitioning beyond the available data (Righter and Drake, 1999; Wade and Wood, 2005; and Cottrell et al., 2009). Predictions based on parameterization of these data suggest a possibly greater influence (Righter et al. 1997; Righter and Drake, 1999) or essentially no influence of pressure (Cottrell et al. 2009).

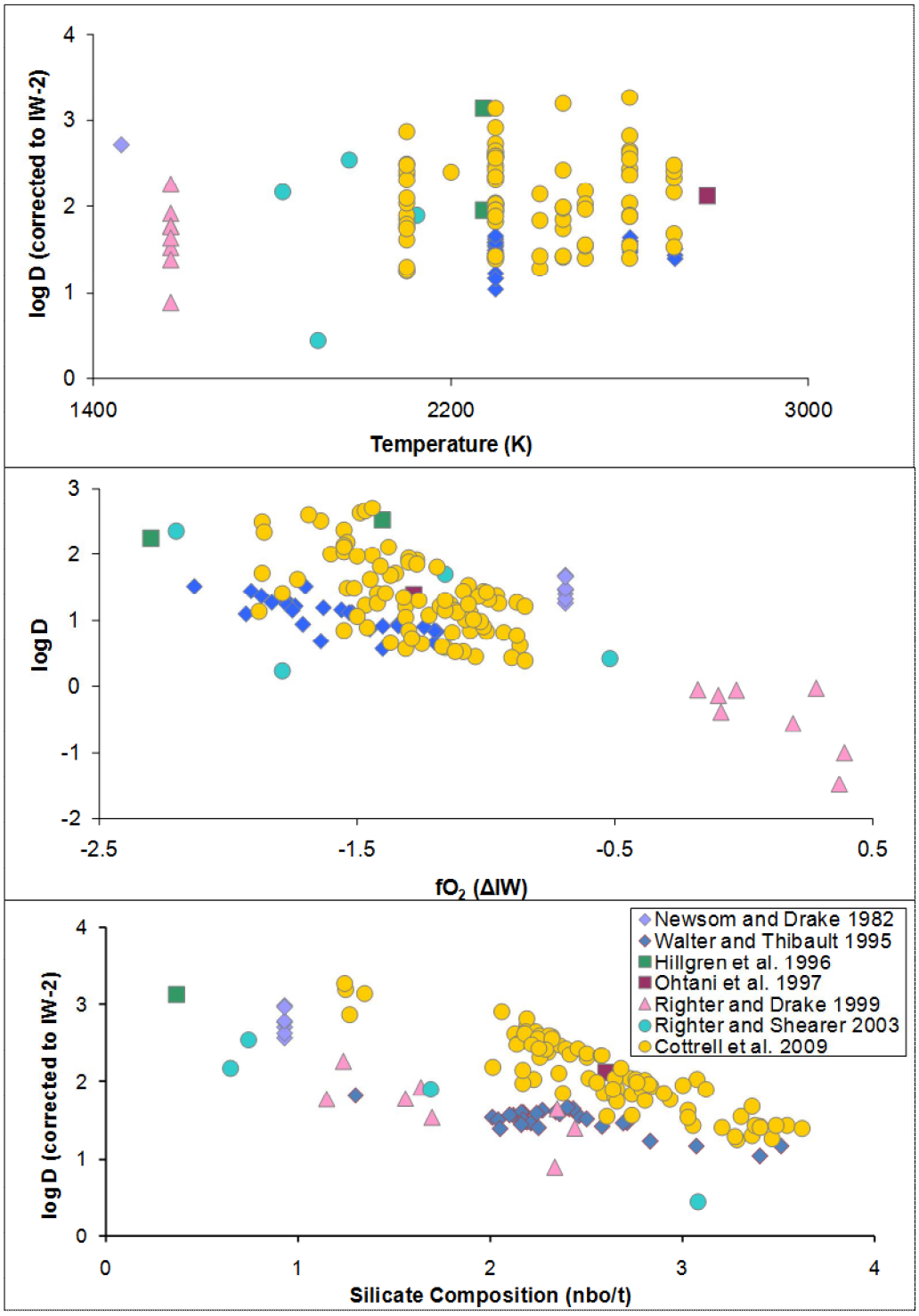

Figure 3. Tungsten metal/silicate partitioning data from literature, plotted as functions of temperature, fO2, and silicate composition. The ratio nbo/t is a proxy for silicate composition, where lower values indicate more polymerized melts and higher values indicate less polymerized melts. Partition coefficients are corrected to common fO2 of IW-2 for temperature and nbo/t plots.

Most proposed equilibration pressures for core formation fall outside of the experimental pressure range of W. Examples are 28 GPa (Li and Agee 1986), 27 GPa (Righter and Drake 1999), 40 GPa (Wade and Wood 2006), 20-50 GPa (Cottrell et al. 2009), and 10-60 GPa (Mann et al., 2009). Most W partitioning data are in the pressure range of 1-bar to 10 GPa with only a small number of measured values available at pressures between 10 and 20 GPa. Higher pressure experimental data were needed to measure this behavior and to address the lack of data a pressures greater than 20 GPa. The trajectory of W metal/silicate partitioning at high pressures in terms of both magnitude and slope are unconstrained due to poor high pressure data coverage and complex interdependencies of temperature, compositional effects and fO_2.

The effect of both silicate and metal melt compositions on metal–silicate partitioning of W and other moderately siderophile elements has been studied, and in some cases well established. The primary effect on metal/silicate partitioning of high valence elements like W in silicate melts is the degree of melt polymerization. This is related to the presence of network-modifying cations, such as Mg and Ca, that disrupt the structure imposed by interconnected silicate tetrahedra. Tungsten is sensitive to the degree of melt polymerization, and shows increased solubility in more depolymerized melts. Further, the affinity of W for silicate melts is stronger with increased Ca abundance relative to Mg (O'Neill and Eggins, 2002).

The composition of the metallic melt also affects W metal/silicate partitioning, particularly the presence of C and S. With increasing S content in the metal phase, W preferentially enters non-S-bearing phases, hence, the W metal/silicate partition coefficient decreases indicating a decrease in siderophility (Jana and Walker, 1997).

The effect of C is the opposite, and by more strongly binding W in the metal phase, calculated partition coefficients increase indicating an increase in siderophility (Cottrell et al., 2009). The effect of C on W metal–silicate partitioning has received greater attention in the literature due to its presence in experimental metal phases through the use of graphite sample capsules in multi-anvil press experiments, and in diamond anvil cell experiments. It is important to include the influence of S and C in characterizing W metal/silicate partitioning given their estimated abundances in the Earth's core of approximately 2 and 0.2 weight percent, respectively (McDonough, 2003).

1.6 Oxygen Fugacity Buffers

The fugacity of oxygen is a measure of the chemical potential of oxygen. As discussed previously, oxygen fugacity exerts a strong control on metal/silicate equilibria. Knowledge of the pressure and temperature dependencies on the relevant metal–oxide systems contributes to understanding of the behavior of elements in metal/silicate equilibria. The coexistence of a metal and its oxide at equilibrium constitutes an oxygen buffer.

1.6.1 Iron–wüstite

The equilibrium between metallic iron and iron (II) oxide exerts a strong influence on many Earth systems and is particularly relevant to the deep Earth due to the presence of a predominantly iron core and an iron-bearing mantle. The term iron-wüstite is derived from the mineral wüstite, which is a slightly non-stoichiometric form of iron oxide ($Fe_{1-x}O$), where $x \approx 0.05$. Wüstite is . At high pressures, iron (II) oxide coexisting

with metallic Fe becomes stoichiometric FeO, hence, the buffer is strictly speaking Fe-FeO, so the use of the iron-wüstite term is conventional.

The oxygen fugacity of experimental and natural systems are often measured or estimated relative to the iron- wüstite (IW) buffer. As an example, using the mole fraction abundances of Fe and FeO, the fO_2 can be estimated relative to the IW buffer by the equation: $\Delta IW=2\log(X_{FeO}/X_{Fe})$. This form of the equation is commonly used and assumes that either ideality of mixing in metal and oxide (activity cofficients equal to one), or that the ratio of the activity coefficients of FeO and Fe are equal to one and are constant with pressure and temperature. The IW (or Fe-FeO) buffer has been characterized to high pressure and temperature conditions by Campbell et al. (2009).

1.6.2 Tungsten–tungsten-dioxide

Estimates of relative fO_2 such as ΔIW are useful measures of the redox state of a system. However, the thermodynamics of these systems can be better understood and quantified with a more precise relationship between a given M-MOx system and IW. The W-WO_2 (WWO) buffer has been studied at ambient pressure conditions and at temperatures up to approximately 1800K (O'Neill and Pownceby, 1993). Oxygen fugacity buffers can have signficant pressure dependencies, so experimental extension of the 1-bar buffers is critical to be able to apply these buffers to the conditions of the deep Earth or to high pressure experiments (Campbell et al., 2009). As will be shown in later parts of this work, application of a high pressure-temperature fO_2 buffer for W provides an alternative, and arguably more robust means of characterizing metal/silicate partitioning, relative to the simplified linear parameterizations in common use, e.g. Wood (2008), Corgne et al. (2008), and Righter (2011). Additionally, published data on

the equation of state for WO_2 is limited to a computational study that estimated the high pressure crystal structure and room-temperature equation of state parameters (Dewhurst and Lowther, 2001).

1.7 Present Experimental Work

To address the paucity of high pressure data on the metal/silicate partitioning of W, I conducted high pressure melting experiments to extend the existing literature data set and to provide experimental constraints on the trend and magnitude of W siderophility at high pressures. As discussed in section 1.6, little is known experimentally about WO_2 at high pressures and temperatures, and consequently the behavior of the W-WO_2 oxygen fugacity buffer is currently unconstrained at high pressures. Therefore, I have conducted high pressure and high temperature experiments to characterize the WWO buffer and describe better the thermodynamics of W partitioning between metal and silicate under magma ocean conditions.

The high pressure melting experiments were made using both a multi-anvil press (MAP), and laser-heated diamond anvil cells (LHDAC). I also conducted low pressure (1 GPa) melting experiments using the piston-cylinder press (PC) at NASA Johnson Space Center to address some specific experimental questions that did not necessarily require the high pressure capabilities of MAP or LHDAC. The experimental work to characterize the WWO buffer was conducted using both DAC and MAP in conjunction with synchrotron x-ray diffraction.

1.8 Hypothesis

My null hypothesis was that the metal–silicate partitioning of W, as described by a partition coefficient, is essentially insensitive to changes in pressure. Prior to much of my experimentation, I had predicted that the effect of pressure on the metal/silicate partitioning of W would be to decrease the siderophility of W, shown by decreasing values of the partition coefficient. My alternate hypothesis was that the metal–silicate partitioning of W, as described by a partition coefficient, is sensitive to changes in pressure.

To reject the null hypothesis, an inclined trend in W metal/silicate partitioning with pressure that is statistically significant should be shown. Statistical significance means that the variation extends outside of analytical uncertainties on chemical compositional measurements of individual samples, or uncertainties on regressed fits to analytical data. To reject the alternate hypothesis, the results of my experiments in the form of measured partition coefficients and regressions or other expressions derived from those data should show no trend in W metal/silicate partitioning with pressure.

2 Experimental and Analytical Methods

The existing high pressure experimental data on metal/silicate partitioning of W provides only limited constraint on the siderophility of W at the high pressure conditions of core formation predicted by various models. Additionally, the near complete lack of high pressure and temperature data on tungsten oxides limits our understanding of the redox behavior of the tungsten-tungsten-oxide equilibrium at the high pressure-temperature conditions of the modern deep mantle, and of predicted high pressure-temperature conditions of core formation.

To address this lack of high pressure and temperature data on W, I conducted high pressure melting experiments on W in a peridotite silicate+metal starting composition. I also performed high pressure and temperature subsolidus experiments of coexisting W and WO_2 using x-ray diffraction to measure volume changes of both phases to characterize the W-WO_2 oxygen fugacity buffer at high pressures. The experimental and analytical techniques employed are described in detail in this chapter. I used two complementary techniques, LHDAC and MAP. Both techniques have advantages and disadvantages, but when combined allowed me to explore a wide range of pressures and temperatures. See Table 1 for both MAP and LHDAC experimental conditions.

For the metal/silicate partitioning experiments, sample starting materials consisted of natural peridotite powder mixed with Fe and W metals. Some experiments also had FeO added to lower the liquidus temperature and increase fO_2. Most MAP experiments also contained approximately 0.3 wt % Mo metal, with the

Table 1. Experimental conditions in metal/silicate partitioning experiments.

Multi-anvil Press

Run#	*P (GPa)*	*T (K)*[a]	*Hydraulic pressure (psi)*	*Press force (metric tons)*	*Sample capsule*[b]	*Assembly geometry*[c]
GN10	26.4	2482	6600	547	MgO poly	8/3
GN11	22.9	2481	5000	415	MgO poly	8/3
GN13	17.4	2511	5125	425	MgO poly	10/5
GN23	16.0	2517	4350	361	Graphite	10/5
GN24	16.0	2413	4350	361	MgO sc	10/5
GN25	12.0	2427	2975	247	Graphite	10/5
GN26	12.0	2367	2975	247	Graphite	10/5
GN30[a]	11.9	2408	3000	249	MgO sc	10/5
GN31	10.3	2373	2500	207	MgO sc	10/5
GN32	24.2	2763	5500	456	MgO sc	8/3

Diamond Anvil Cell

Run#	*P (GPa)*	*+/-*	*T (K)*	*+/-*
G34	49.8	1.3	3766	26
G36c	28.1	1.0	3837	69
G38a	40.3	1.8	4446	68
G38b	40.3	1.8	2962	56
G39a	27.0	1.0	3182	77

Piston Cylinder

Run#	*P (GPa)*	*T (K)*	*Hydraulic pressure (psi)*	*Sample capsule*
GPC1	1.0	1750	1450	MgO
GPC2	1.0	1750	1450	MgO
GPC3	1.1	1750	1570	MgO
GPC4	0.9	1750	1300	MgO
GPC5	1.0	1750	1450	MgO
GPC6	1.0	1800	1450	Graphite
GPC7	1.0	1800	1450	Graphite

[a]Temperature estimated from power-temperature curves due to loss of thermocouple during compression. [b]For MgO capsules: poly = polycrystalline, and sc = single crystal. [c]For the assembly geometry, shown as either 8/3 or 10/5, the first number gives the edge length in mm of the octahedron face, and the second number is the edge length of the truncation on the WC cube corner.

intention to collect metal/silicate partitioning data on Mo (Table 2). Measurement of Mo in the silicate would require LA-ICP/MS, due to its low abundances and these data has not yet been collected. The peridotite powder was provided by Dr. Roberta Rudnick, and was derived from mantle xenolith samples DMP56 and DMP60, which are spinel lherzolites. Both samples were analyzed for major elements and selected trace elements (Rudnick et al., 2004).

Table 2. Composition of starting material powder mixtures for MAP, LHDAC, and PC experiments. Quantities are weight percents of the indicated components or of total powder mixtures.

Mix	*Peridotite*	*FeO*	*WO_2*	*Total silicate*	*Fe*	*W*	*Mo*	*Total metals*	*Fe/W*[a]	*Silicate/metals*[a]
Multi-anvil Press										
JSC1[b]	69	-	-	69	29	1.8	0.33	31	16	2.2
JSC2[c]	67	-	-	67	28	5.3	0.31	33	5.2	2.0
JSC3[d]	62	7.4	-	69	26	4.9	0.29	31	5.2	2.2
Diamond Anvil Cell										
DAC	73	12	-	85	12	3.0	-	15	4.9	5.6
Piston Cylinder										
HL	63	6.0	-	69	31	0.31	-	31	100	2.2
HM	62	6.2	-	68	30	1.5	-	32	20	2.2
HH	63	6.3	-	70	25	5.0	-	30	5	2.3
RevM	65	4.9	-	70	28	2.4	-	30	38[e]	2.3
RevO	65	5.3	3.8	72	28	0.0	-	28	40[e]	2.6

[a]Ratios of Fe/W and silicate/metals are in terms of mass. [b]Used in experiments GN1-GN9. [c]Used in experiments GN10-GN14, GN20-GN21. [d]Used in experiments GN15-GN19, GN22-GN32. [e]Molar ratio.

2.1 Multi-anvil Press (MAP)

The MAP technique is an established technology and has been extensively utilized for high pressure metal/silicate partitioning studies (Li and Agee, 1986; Walter and Thibault, 1995; Righter and Drake, 1999; Cottrell et al., 2009). MAP experiments are desirable because of the larger sample volumes attainable, which allows easy sample recovery, preparation and compositional analysis. I conducted MAP experiments on the 880 ton Rockland Research press located in the High Pressure Petrology Laboratory at NASA Johnson Space Center, Houston, Texas. These experiments used standardized octahedral assemblies developed by and obtained from the Consortium for Materials Properties Research in Earth Sciences (COMPRES) Multi Anvil Assembly Development Project at Arizona State University (Leinenweber, 2005).

I used both 10/5 and 8/3 octahedral assembly sizes. This assembly nomenclature lists the truncation edge length (TEL) of the octahedron first, and the TEL of the anvil

cube truncation second. Experiments in the 10/5 assembly are applicable for experiments in the pressure range of 10 to 20 GPa. Experiments in the 8/3 assembly are applicable for experiments in the pressure range of 20 to 30 GPa. Schematics of 10/5 and 8/3 octahedral assemblies are shown in Figure 4.

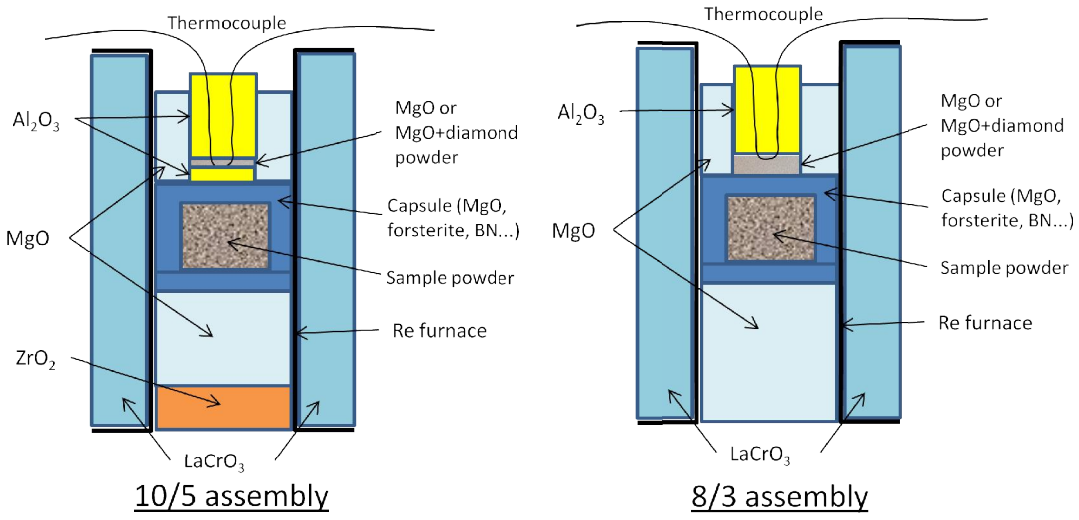

Figure 4. Schematics of COMPRES standardized multi-anvil press assemblies.

High pressures in MAP experiments are generated by application of uniaxial force from hydraulic pressure driving an upward-directed ram that is opposed by a fixed plate. Between the ram and fixed plate is the cell that contains six wedges, three above and three below, that redistribute the uniaxial force to three orthogonal force directions by pressing on the cube assembly. The cube assembly contains eight tungsten carbide cubes whose corners are truncated. These truncations press against opposing faces of the octahedral assembly thus ideally generating hydrostatic pressure conditions within the sample chamber (Figure 5).

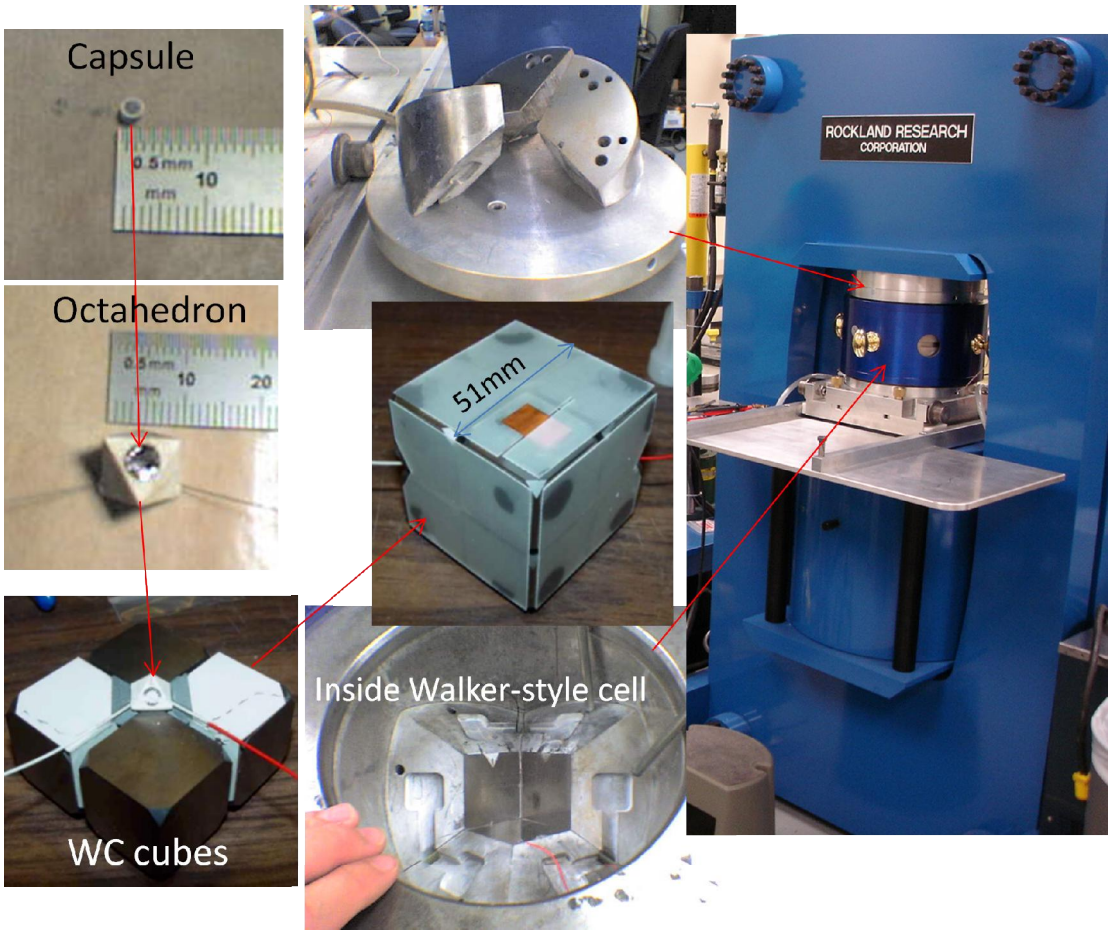

Figure 5. Cube assembly components, components of MAP cell, and position within 880-ton press at NASA Johnson Space Center.

2.1.1 Sample Capsule Compositions

Early MAP experiments, GN1-GN7, were conducted using boron nitride (BN) capsules. It was thought that this capsule material would react minimally with the silicate melt, but significant capsule dissolution occurred, which was suspected based on low microprobe totals from measurements of the quenched silicate. The presence of boron was confirmed by LA/ICP-MS data obtained on a piston-cylinder experiment of similar composition where eight to ten percent boron was detected in the silicate fraction. At this concentration, boron is a major element of the silicates in these experiments, and, therefore they are not representative of the Earth's mantle, in which

the boron abundance is approximately 0.3 ppm. Additionally, metal/silicate partitioning between Fe-rich metal and borosilicate glass at high pressures are poorly understood. For both of these reasons, compositional data obtained from samples GN1-GN7 were not used in the models of metal/silicate partitioning of W presented in this study.

Most of the remaining samples were conducted in polycrystalline or single-crystal MgO capsules. This capsule composition is commonly used in MAP experiments, and while it too reacts with the melt, the effect on the run product silicate composition is predictable and consists of increasing the Mg content to some degree depending on length of time at high temperature. Sample GN13 is a good example of this, where multiple large ferropericlase (Fp) grains are present due to melt interaction with the MgO sample capsule, enriching the melt in MgO (Figure 6). The single-crystal MgO capsules were found to be the superior choice because they limited the migration of melt at the high temperatures required to melt peridotite at high pressures. The polycrystalline MgO capsules were much more permeable than single crystal capsule and allowed migration of melt, thus, commonly resulting in experimental failure due to melt interaction with the Re furnace.

Three experiments, GN23, GN25 and GN26, were conducted using graphite capsules. The major benefits of these capsules are their stability at high temperatures and no interaction with the silicate melt. The major drawback is that they interact with the metallic melt, resulting in formation of Fe and W carbides. The presence of carbon in Fe and W alloys has a known effect on metal activities and, thus, on calculated partition coefficients where the activity coefficients are assumed to be ideal. This is discussed in greater detail in Chapter 3. Additionally, in these three experiments the

metallic liquid did not form spherical segregations but disseminated into the capsule walls. Thibault and Walter (1995) reported this behavior with Fe-bearing metallic melts in graphite capsules and attributed it to low surface tension between metallic liquid and solid C related to the graphite to diamond transition of the capsule.

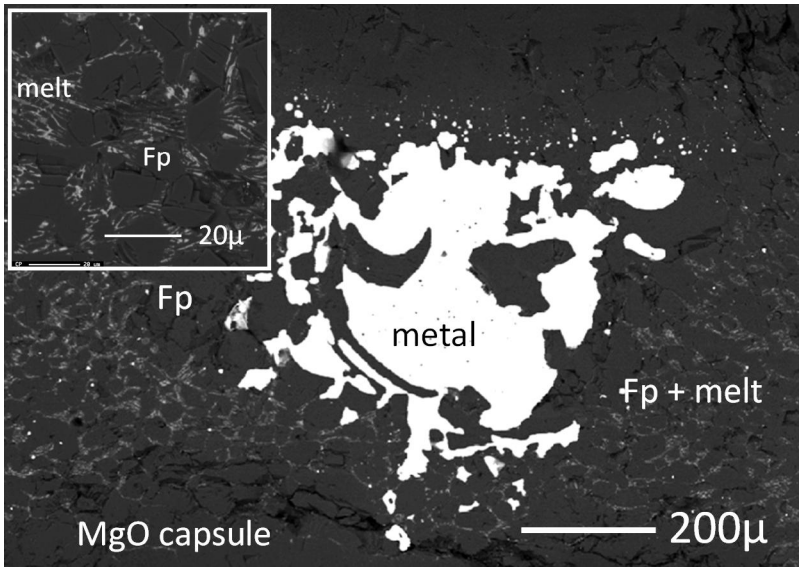

Figure 6. Backscattered electron image of MAP sample GN13, showing extensive growth of ferropericlase with interstitial melt. Ferropericlase was an equilibrium phase and its pervasive growth was due to saturation of the silicate melt by MgO from the capsule.

2.1.2 Sample Recovery and Preparation for Analysis

Sample recovery for MAP experiments was straightforward. The recovery procedure was essentially the same for all samples. The compressed octahedral assembly was removed from the cube assembly. The rough edges of the octahedron were broken away and the thermocouple wires were clipped. The octahedron was cut opened along the axis of the sample capsule using a rotating diamond-blade saw. For MgO capsules, the octahedron was cut directly through the approximate center of the capsule. For graphite capsules, the octahedron was cut just adjacent to the outer wall of the capsule, because it was not feasible to cut through the diamond capsule; the high

pressure conditions of the experiments transformed the graphite capsule because diamond was the stable carbon phase. The cut octahedron was embedded in epoxy. The epoxy-mounted sample was then polished to minimize sample surface topography.

For MgO capsules, wet polishing began with SiC paper of P120 grit size to quickly plane the epoxy-sample surface and to expose the sample chamber at the desired depth in the sample capsule, which was ideally the center of the capsule. The sample was polished further with progressively finer SiC papers down to P2000 grit size. The final polish used diamond abrasives in oil suspension or diamond-impregnated mylar polishing laps with steps at six, three and one μm grit particle sizes.

For graphite capsules (transformed to diamond), the initial polishing proceeded differently due to the high hardness of diamond relative to other materials in the sample. The sample surface was abraded with a fairly coarse SiC paper to remove epoxy, sample materials, and assembly component materials, leaving the diamond capsule in topographic relief. The exposed diamond was abraded using a diamond-impregnated polishing wheel until the capsule and sample surfaces were approximately coplanar. This process was repeated until the desired depth in the sample capsule was reached. Progressively finer SiC papers were used, P120, P360, and P600, corresponding to progressively finer diamond wheel grit sizes of 120, 45, and 6 μm. The final polishing consisted of two steps at three and one μm grit particle sizes using diamond abrasives in oil suspension.

2.2 Laser-heated Diamond Anvil Cell (LHDAC)

The LHDAC technique in terms of conducting laser-heated experiments is an established technology. Recovery of the run products and obtaining analytical data, however, is an emerging or cutting-edge technology. The major advantage of LHDAC over MAP is the ability to reach very high pressures and temperatures. The major drawback for experimental petrologic studies is sample recovery and preparation for compositional analysis. However, the focused ion beam (FIB) instrument provides a viable means to do this, as shown by the present study and several others (Auzende et al., 2008; Irfune et al., 2005; Miyahara et al., 2008; Ricolleau et al., 2008). More detail on using the FIB is given in a following section.

2.2.1 Sample Loading and Pressure Media

The DAC technique is based on applying a unidirectional stress along the axis of the diamond anvils which compresses the sample held between the anvils. The diamond anvils are gem quality and brilliant cut similar to a gem, except that the pointed end opposite the table is truncated to form a culet face, which is the surface in contact with the gasket and sample chamber (Figure 7). The sample chamber consists of a small

hole, typically 150 microns in diameter, drilled in a metal gasket consisting

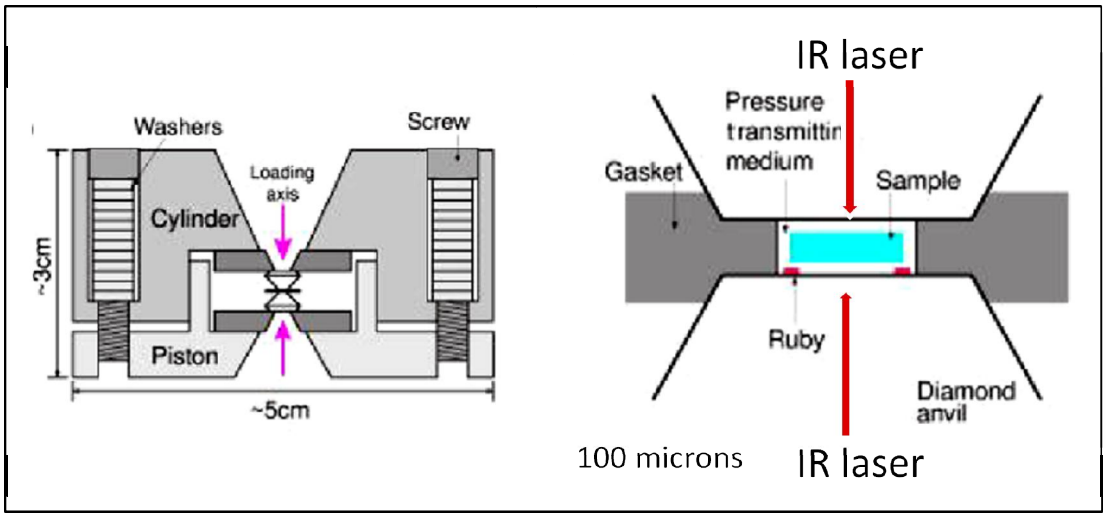

Figure 7. Schematic of diamond anvil cell.

of a thin disc or square that is approximately 250 microns thick. Gasket materials used in this study were steel, Inconel (a nickel-chromium alloy), and rhenium; the choice is primarily based on the maximum pressure of the experiment where the harder Re is preferable at high pressures. Before drilling the sample chamber, the gasket is pre-indented using the diamond cell. This allows for precise positioning of the sample chamber on the axis of the diamond anvils and aids in sample loading by centering the indentation in the gasket on the diamond anvil. Sample loading for solid media consists of placing layers of insulator next to the diamond anvils and a sample layer in between. Theses layers consist of foils of the materials made from powders compressed in a diamond anvil cell with culets of one mm diameter. The actual placement of the foils is done using a finely-pointed W needle where the foil is held to the needle by static charge, and the foils are stacked into the sample chamber by hand on atop another. Pressure in the sample chamber is a function of the applied force divided by the area of the diamond anvil culet faces. The pressure transmitting medium, typically referred to

simply as the pressure medium, distributes this stress to ideally produce a uniform stress field around the sample. A given pressure medium achieves this to some extent based on the properties of the medium in use. In simplest terms, the lower the shear strength of the pressure medium, the more hydrostatic is the pressure within the sample chamber. The pressure medium also serves as an insulator between the sample material and the diamond anvil culets during laser-heated experiments, where certain materials such as metals can react with the diamonds at sufficiently high temperatures. Beneficially, the high temperatures of these melting experiments served to relax the non-hydrostatic stresses in sample and pressure medium thus promoting hydrostatic conditions.

Several pressure media and related sample loading geometries were explored. These were: KBr, Argon, MgO, and natural silicate. After exploring these options, it was found that the best pressure medium was the same silicate material (peridotite) of the sample mixture without metals added. This configuration gave the most controllable experiments in terms of laser absorption, evenness of sample heating, and control over the reaction at high temperatures.

2.2.2 Laser Heating

In DAC experiments, the only means to melt the powdered starting materials is through laser-heating. The basis of this technique is the heating of metals by absorption of infrared laser light, and through this absorption the surrounding materials are also heated. The UMD Laboratory for Mineral Physics is equipped with a 50 W laser at 1064 nm for DAC laser-heating. This system allows for either single-sided or double-sided heating, depending on the characteristics of the materials in the experiment.

Double-sided heating is useful for thicker or opaque samples, and reduces the axial thermal gradient. The front and rear distribution of laser power is adjusted during an experiment by visually matching the visible light portion of the thermal emission at a laser power level where visible emission is first observed. A background image for each experiment is taken with the laser energized but at a power level just below where thermal emission is detectable.

Laser heating proceeds by progressively increasing the laser power while visually and spectroscopically monitoring the experiment. During laser heating, the temperature distribution of the laser-heated spot could be measured using the 2-d spectroscopic method described in further detail in 2.2.3. Laser power was increased by one to three percent steps every ten seconds, and thermal emission images were collected approximately every two seconds. Power was increased until melting of the silicate was achieved. Criteria for assessing silicate melting were based on observation of maximum temperatures and of inferred fluid motion based on changing thermal distributions. An increase in thermal emission intensities of approximately one order of magnitdue was associated with silicate melting. The metals show the greatest emission because they most strongly absorb the incident laser beam. Motion due to melting was seen in successive thermal emission images as changing positions and sizes of the brightest regions which correlated to molten metal blebs. These motions were related to mobilization of multiple smaller metal blebs in silicate liquid that coalesced to form single larger metal segregations, which were observed in sectioned samples. Successful laser-heating was also assessed based on the optical appearance of the laser-heated spot as viewed through the diamond anvils. Successful experiments showed a characteristic

morphology of a central dark region where the metal bleb resided surrounded by concentric rings of varying colors that consisted of silicate melt and subsolidus-transformed silicate crystalline materials (Figure 8).

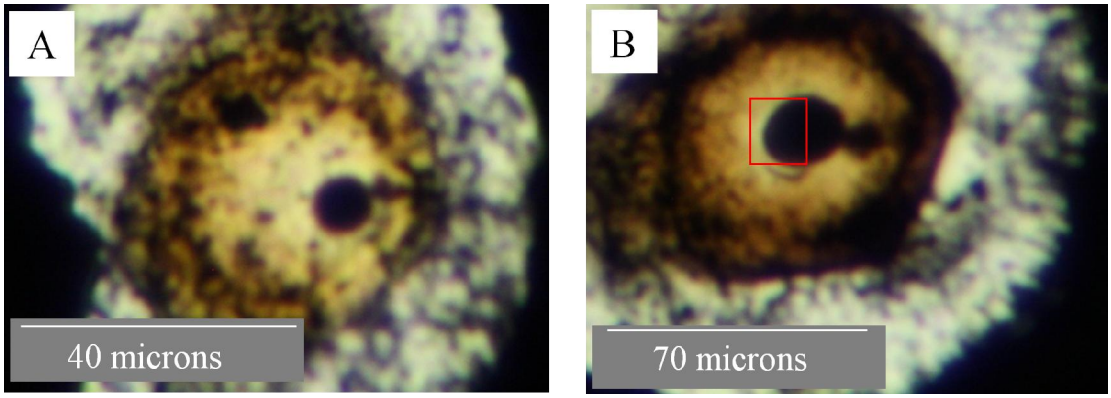

Figure 8. Transmitted light images of representative LHDAC samples: A) G28 P=28GPa, and B) *G29 P=36GPa. *Location of region investigated using FIB shown by red box (B).

The diameter of laser-heated spots is mostly a function of the diameter of the laser beam with a tradeoff between beam diameter and laser power required to melt the sample. The size of the region melted or transformed during laser heating is typically 20 to 50 microns in diameter. The total thickness of sample and insulating materials following compression and heating is typically less than 10 microns.

2.2.3 Temperature Measurement

Thermal gradients can be high in LHDAC experiments. Factors affecting the magnitude and distribution of these gradients include: thicknesses and thermal conductivities of the sample and insulator materials, diameter of the laser beam, absorption characteristics of the sample materials, and the maximum temperature.

I was able to quantify the radial gradient using the temperature mapping system in the UMD Laboratory for Mineral Physics. This system allows for the generation of a 2-dimensional temperature map of the laser-heated region of a sample (Figure 9).

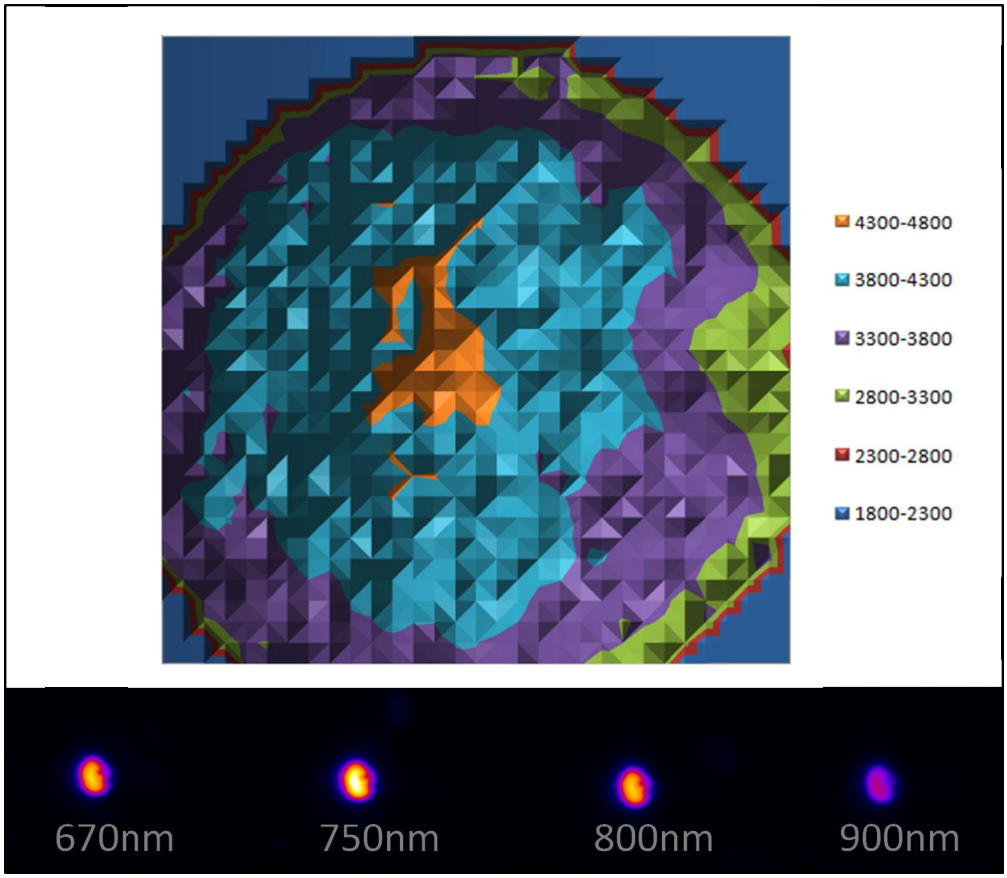

Figure 9. Two-dimensional temperature map derived from the thermal emission images shown at bottom. Colors on thermal emission image indicate intensity, white is highest intensity and blue is lowest intensity. Temperature map is 31x31 cells with a cell dimension of approximately 0.8 microns. Temperature ranges at right of temperature map are in Kelvins.

The temperature map is based on fitting measured thermal emissions to the Planck radiation function (Campbell, 2008). In the case of a completely opaque absorber with a transparent, non-absorbing insulator, axial gradients can be estimated based on the maximum temperature (T_{max}) at the sample mid-plane, and the minimum temperature at the diamond anvil faces (T_{anvil}). Campbell et al. (2009) argued that T_{anvil} can be approximated as (T_{max} - 300 K) / 2. In the experiments in this study, however, the axial

gradients were lower than the case just described. This was due to partial laser absorption by the Fe-bearing silicate material. The cross-sections of LHDAC samples from this study show melted silicate regions within approximately one micron of the diamond anvils. This indicates that the temperature within one micron of the anvils was at or above the liquidus temperature of the melt at the measured experimental pressures, and therefore the temperature of the diamond anvils was higher than would be estimated based on the approximation of T_{anvil} given above.

The experimental temperatures for LHDAC samples as reported in Table 1 were determined from the temperature maps, and are estimates of the temperature at the interface of metallic and silicate melts in those experiments. This is appropriate because the primary purpose of the experiments was to measure metal/silicate partitioning, and the partitioning of W, i.e. the equilibrium of W between metal and silicate, occurred at this interface. The location of the metal-silicate interface on the temperature maps was based on two premises: 1) the most intense thermal emission in the LHDAC experiments was from melted metallic regions, which were shown on the temperature maps as high temperature peaks in the centers of the maps; and 2) these high temperature peaks on the maps could be spatially correlated to the sectioned sample images through physical scaling of the temperature map pixels and sample images.

The traditional method of measuring temperature in LHDAC experiments used spectroscopy where hundreds of narrowband measurements were made simultaneously (Shen et al., 2001). These measurements might be made in the center of the laser-heated spot, a band across the spot, or across the entire spot. The first of these would be assumed to represent the highest temperatures, the second would represent a

temperature distribution profile ideally across the hottest part of the spot, and the third would represent an average temperature across the sampled part of the spot. The major drawback to this method is the underlying assumption of a radially-symmetric temperature distribution, which is not always achieved in practice. Chromatic aberration is also an issue because focus is wavelength dependent and therefore all wavelengths will not be simultaneously in focus at the optical aperture (Campbell, 2008).

The 2-d system used in this study addresses these limitations by independently focusing four narrowband images of the laser-heated spot with 10 nm bandwidths centered at 670 nm, 750 nm, 800 nm, and 900 nm. All four images are simultaneously focused to separate regions of a CCD detector. The collected digital thermal images are processed to remove background (both the collected background image and a flat field subtraction) and to apply a calibration correction. System calibration images were periodically collected by lab personnel generally following maintenance and were applicable for all experiments within a given maintenance interval. The four regions of the image representing the four wavelength bands are aligned and fitted to the Planck radiation function $I = C\varepsilon\lambda^{-5}/\left(\exp(hc/\kappa\lambda T)-1\right)$ which relates intensity of emission (I) to emissivity (ε), wavelength (λ), and temperature (T); C includes physical constants and experimental geometric factors, and κ is the Boltzmann constant. The gray body approximation, where emissivity is assumed to be independent of wavelength, is used in temperature calculations. For simplification of fitting, the Wien approximation of the Planck function is used (Campbell, 2008). At temperatures less than approximately 4000 K, and in the range of wavelengths of interest here, the Wien approximation,

expressed as $I = C\varepsilon\lambda^{-5} / \exp(hc/\kappa\lambda T)$, gives temperatures that deviate from the Planck blackbody spectrum by less than four percent. The Wien approximation can be simplified to a linear equation in T^{-1} that is amenable to linear least-squares fitting (Heinz and Jeanloz, 1987).

2.2.4 Pressure Measurement

For all laser-heated experiments, small quantities of ruby were added for pressure calibration. This is an established procedure based on the calibrated pressure-dependent shift in a doublet of fluorescence peaks that result from green laser light impinging on a ruby grain (Mao et al, 1986). Pressures were measured at multiple locations within the sample chamber prior to and following laser-heating. The uncertainty on the pressure was taken as the standard error of the mean of the post-heating pressure measurements.

2.2.5 Sample Recovery and Preparation for Analysis

The run product of a LHDAC experiment consists of a laser-heated region within untransformed materials contained within the sample chamber. It is trivial to remove the gasket from the DAC. Removing the sample from the gasket for further processing, i.e. mounting and polishing, is more challenging. Because of the basic LHDAC sample geometry, I attempted two recovery techniques for traditional epoxy mounting and polishing: 1) the sample remained in the gasket, and 2) the sample was removed from the gasket. Recovery option 1 has the merit of simplicity and provides complete preservation of all material in the sample chamber and preservation of experimental sample orientation. The main drawback in this option is the presence of the gasket material in the sample mount, which can be an issue depending on the anticipated

sample analysis technique and as a complicating factor in sample polishing. Recovery option 2 can be more complicated depending on the sample loading geometry. It also most often does not preserve all the materials in the sample chamber, which makes it more difficult to determine experimental sample orientation. The major advantage is that the gasket material does not become part of the sample mount, which simplifies polishing and can be beneficial for some analytical techniques. I found that recovering the sample intact in the gasket was the best method. Attempts at removal of sample materials from their gaskets resulted in a low success rate with the major problem being that samples tended to break apart during removal complicating identification of the laser-heated region.

Two sample mounting geometries are appropriate to prepare LHDAC samples for microprobe analysis: 1) sample flake mounted parallel to the mounting substrate (horizontal mounting), and 2) sample flake mounted perpendicular to the substrate (vertical mounting). The first geometry is perhaps the most straightforward and would be the logical choice for macroscopic samples such as a rocks or mineral grains. However, because LHDAC samples are typically less than 10 microns thick, parallelism to the substrate becomes a critical matter. This is important because even a slight inclination of the sample flake relative to the substrate can result in sample loss when polishing. The major advantage to this geometry is the ability to measure radial composition. The second geometry overcomes this limitation by polishing through the sample perpendicular to the thin dimension. It is thus possible to more precisely polish to the region of interest within sample without concern for parallelism of the sample to the substrate. I mounted two LHDAC samples using the perpendicular mounting

method based on the previous experiences of others in the Laboratory for Mineral Physics with the horizontal method. Attempts to analyze these samples by EMPA, where the activation volume on a sample of DAC scale was of major concern, showed that x-ray interaction between metal and silicate, and between transformed and untransformed materials was an intractable problem.

2.3 Piston Cylinder Press (PC)

The PC technique has a longer lineage than MAP and differs from MAP both in design and upper pressure and temperature limits. The major advantages of PC are larger sample volumes and faster experimental run times. The cross-sectional area of experimental run products in the PC are commonly five to ten times that of those in MAP experiments. This is particularly beneficial when analyzing for low-abundance, e.g. trace level, elements that require use of LA/ICP-MS where larger sample feature sizes are preferable or required. Total experiment times are significantly shorter than MAP, as little as one hour. The shorter run times are mostly due to the rapid compression and decompression, taking only minutes versus many hours for MAP.

2.4 Focused Ion Beam (FIB)

As discussed in previous sections, I determined that the FIB technique is the most effective means of sectioning and preparation of LHDAC samples for compositional analysis. This method allows for precise sectioning of a sample, providing a slice through the sample parallel to the heating axis. The main advantage is that only a thin portion of the sample, on the order of one micron or less, is extracted and mounted in

such a way that the profile of the sample can be analyzed. This was crucial for metal/silicate partitioning measurements because interaction of the analytical beam with the insulating peridotite silicate material would have made assessment of quench silicate melt compositions highly uncertain. Samples were sectioned at NASA Johnson Space Center using an FEI Quanta 3D FEG, which combines FIB and SEM capabilities.

The basic operation of FIB involves vaporizing sample material using a high energy gallium ion beam, a process known as milling. Regions of arbitrary dimensions can be milled by rastering the ion beam. The rate of milling can be controlled by adjusting beam current, but is also affected by material properties. High milling rates commonly result in re-deposition in the vicinity of the milled area.

The following briefly describes the procedure used to produce FIB sections from my LHDAC samples, and the images shown in Figure 10 illustrate the process of sectioning LHDAC sample G36c. (1) The laser-heated spot (region of interest) was located, either by measurements from imagery obtained prior to loading in the FIB machine or by identification of surface features. This proved problematic for DAC samples and is discussed further below. (2) A thin layer of platinum was deposited along the region of interest, which was used as a high Z-contrast marker for reference during milling. (3) Material was excavated on both sides of the region of interest, leaving an approximately four micron thick section. Careful attention was paid during excavation to mill to the center of the laser-heated spot. This was done to ensure that features such as the metal blebs had the same dimensions on both sides of the section to maximize the analyzable area. (4) The section was cut nearly completely free on both

ends of the section leaving on a small region connected to the bulk sample. The section was thinned to approximately two microns. (5) A tungsten needle was welded using platinum to the upper corner of the sample opposite the remaining connection to the bulk sample, and this connection was then cut. (6) The section was lifted away from the bulk sample and welded to a copper TEM grid, and thinned (equivalent of polishing) to approximately one micron by rastering the ion beam parallel to the section surface.

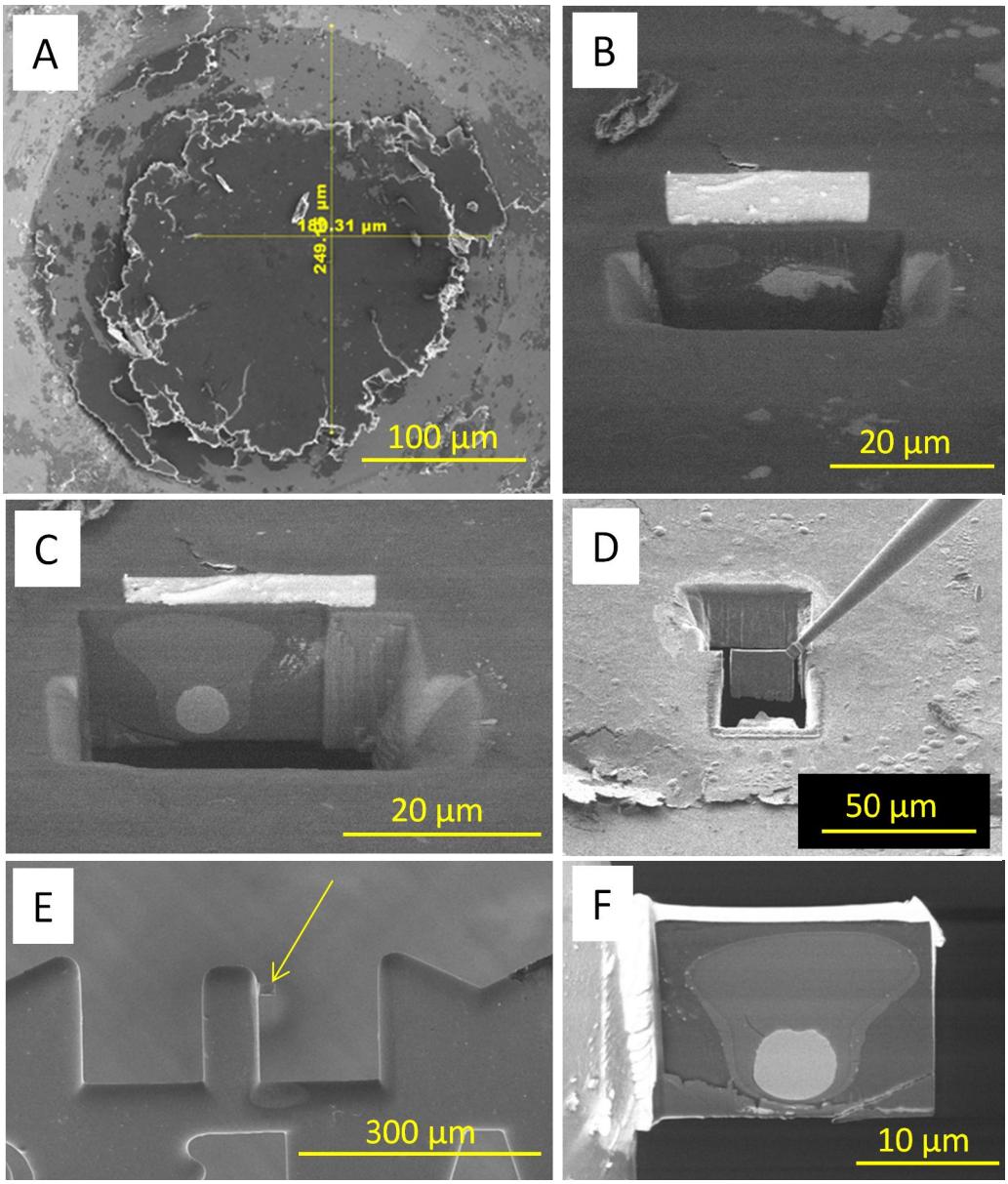

Figure 10. Backscattered electron images illustrating the process of sectioning LHDAC sample G36c using FIB. The sequence proceeds left to right and top to bottom beginning with the upper left (A): (A) locating region of interest; (B) excavating on one side of laser-heated spot; (C) completed excavation on one side of spot; (D) following excavation on other side, section welded to W needle is lifted away from bulk sample; (E) section welded to copper TEM grid; and (F) high-resolution view of completed, polished section.

2.4.1 Locating the Region of Interest

The most challenging aspect of using FIB to section the LHDAC samples was locating the region of interest within each sample. Two sources contributed to make this challenging. First, the laser-heated regions were readily visible in transmitted

optical imagery, which was the only means of imaging the samples following laser heating. But, within the FIB, secondary electron, backscattered electron, and ion imaging were the only means of viewing the sample, which showed only surface features. Second, measurements taken from optical imagery did not always correspond well to those made with the FIB using electron or ion imaging, with measurement differences up to several microns. The source of this error was not definitively determined, but may have resulted from distortions of electron and ion beam images due to aspect ratio scaling errors. After much trial and error, it was found that the most reliable and efficient means of locating the regions of interest was by using surface features on the samples such as fractures, topographic bulges around laser-heated regions, and edges of the bulk sample or the sample chamber hole. This was aided by taking reflected light images of the samples focused on the sample surfaces, combined with transmitted light images that best showed the laser-heated areas, and relating to surface features visible within the FIB by electron imaging. Six LHDAC samples, G31, G34, G36, G38a, G38b and G39, were sectioned by FIB and are described in detail in Chapter 3.

2.5 Electron Microprobe

All samples were analyzed for chemical composition by electron microprobe using wavelength dispersive spectroscopy (WDS). The majority of samples were analyzed using a JEOL JXA-8900 located in the Nanoscale Imaging Spectroscopy, and Properties Laboratory at the University of Maryland. Samples GN23-GN26 were analyzed using a Cameca SX-100 microprobe located at NASA Johnson Space Center.

The beam conditions common to analysis of all samples were 15 kV accelerating voltage and 20 nA beam current. Peak and background counting times are given in Table 3. Electron beam diameter was chosen depending on the requirements of individual samples, primarily dictated by the sample feature sizes, e.g. average dimensions of crystals in quenched silicate melt and of exsolution domains in quenched metallic liquids. The efficacy of using a broad, defocused versus a narrow, focused beam to characterize the average composition of silicate quench textures and exsolved metals was evaluated for sample GN24. Chabot and Drake (1997) compared EMPA broad beam analysis of a multi-phase quenched metallic liquid with composition determined by image processing of a backscattered electron image of the sample. The percentages of the two phases were calculated from the image, and the compositions of the individual phases were known from narrow beam measurements of those phases. A strong linear correlation was found between the compositions of the metallic liquid using these two techniques.

In sample GN24, a transect consisting of 50 measurements was made across a portion of the quenched silicate melt with approximately 7 microns spacing between measurements, with a beam diameter of 1 micron. The composition of the silicate melt, as mole percent oxides, based on the average of these measurements was: 7.0 ± 0.48 FeO, 54 ± 1.6 MgO, 35 SiO_2 ± 0.49, 1.3 Al_2O_3 ± 0.30, and 2.5 CaO ± 0.54. Six measurements were made with a beam diameter of 50 microns. The composition of the silicate melt based on the average of these measurements was: 7.1 ± 0.31 FeO, 54 ± 0.57 MgO, 35 ± 0.45 SiO_2, 1.3 ± 0.09 Al_2O_3, and 2.4 ± 0.22 CaO. Similarly, a transect of 35 measurements was made across the largest metal region in the sample with a 1

micron beam diameter, and approximately 5 microns spacing between measurements. The composition of the quenched metallic liquid based on the average of these measurements, as mole percent, was: 93 ± 0.31 Fe, 5.6 ± 0.22 W, 0.56 ± 0.03 Ni, and 0.80 ± 0.07 Mo. Measurements were made using a 50 micron beam on seven metal segregations, including the largest one where the 1-micron beam transect was made, and the metal composition based on the average of these measurements was: 93 ± 0.46 Fe, 5.3 ± 0.12 W, 0.56 ± 0.05 Ni, and 0.75 ± 0.07 Mo.

Table 3. Electron microprobe element suites, associated standards, and peak and background count times.

Element	*Phase*	*Standard*	*Peak count time (sec.)*	*Background count time (sec.)*
Fe	Oxide	Forsterite	20	5
Si	Oxide	Forsterite	10	5
Ni	Oxide	Forsterite	60	5
Mg, Ca	Oxide	Diopside	10	5
Al	Oxide	Orthoclase	10	5
K	Oxide	Orthoclase	30	5
Cr	Oxide	Chromite	30	5
Mn	Oxide	Rhodonite	20	5
Ti	Oxide	Ilmenite	10	5
Na	Oxide	Albite	30	10
W	Oxide	Scheelite (JEOL) W metal (Cameca)	120 (30 for high abundance samples)	30
Fe	Metal	Fe	20	5
W	Metal	W	30	5
Ni	Metal	Ni	60	5
Cr	Metal	Cr	30	5
S	Metal	Pyrrhotite	50	10
O	Metal	Magnetite	60	5
Mg	Metal	Diopside	10	5
Si	Metal	Forsterite	10	5

Element abundances in nearly all samples were calculated using the CITZAF correction algorithm (Armstrong, 1995). For LHDAC samples G34 and G36, abundances were calculated using the Phi-Rho-Z (PRZ) algorithm assuming a thin-film sample geometry, for comparison to ZAF, and the two methods gave comparable results. Analytical results for silicate and metallic phases are shown in Tables 4 and 5.

Table 4. Compositions of silicate phases as measured using electron microprobe. Abundances are in weight percents of oxides.

Run	*Phase*[a]	*WO_2*	*FeO*	*Al_2O_3*	*K_2O*	*Na_2O*	*MnO*	*SiO_2*	*CaO*	*MgO*	*Cr_2O_3*	*NiO*	*TiO_2*	*Total*	*N*[b]
GN10	Aki	0.19	11.52	54.16	0.01	0.11	0.09	4.34	0.22	22.46	7.57	0.04	0.12	100.83	1
	sigma	*0.03*	*0.08*	*0.19*	*0.01*	*0.01*	*0.02*	*0.06*	*0.02*	*0.13*	*0.05*	*0.02*	*0.02*		
	Pv[c]	0.10	10.48	0.19	0.00	0.09	0.12	42.52	0.19	48.53	0.03	0.21	0.02	102.49	36
	sigma	*0.01*	*0.01*	*0.00*	*0.00*	*0.00*	*0.00*	*0.03*	*0.00*	*0.03*	*0.00*	*0.00*	*0.00*		
	Maj	0.10	6.24	4.82	0.00	0.12	0.11	55.58	0.71	33.60	0.27	0.07	0.13	101.75	11
	sigma	*0.01*	*0.02*	*0.02*	*0.00*	*0.00*	*0.01*	*0.05*	*0.01*	*0.05*	*0.01*	*0.01*	*0.01*		
	Melt	0.13	3.52	6.39	0.02	1.17	0.09	50.36	18.77	15.56	0.47	0.03	0.42	96.91	7
	sigma	*0.01*	*0.02*	*0.02*	*0.00*	*0.01*	*0.01*	*0.06*	*0.05*	*0.04*	*0.01*	*0.01*	*0.01*		
	Pv	0.17	7.27	2.62	0.03	0.07	0.08	53.96	0.63	37.08	0.12	0.01	0.13	102.15	1
	sigma	*0.03*	*0.07*	*0.04*	*0.01*	*0.01*	*0.02*	*0.18*	*0.03*	*0.16*	*0.02*	*0.02*	*0.02*		
GN11	Aki	0.19	10.99	55.98	0.00	0.36	0.13	0.51	0.08	26.84	7.08	0.02	0.22	102.41	1
	sigma	*0.03*	*0.08*	*0.19*	*0.00*	*0.02*	*0.02*	*0.02*	*0.01*	*0.14*	*0.05*	*0.02*	*0.02*		
	FP	0.12	15.42	1.13	0.01	0.13	0.11	2.45	0.48	81.63	0.21	0.01	0.04	101.74	6
	sigma	*0.01*	*0.04*	*0.01*	*0.00*	*0.01*	*0.01*	*0.02*	*0.01*	*0.10*	*0.01*	*0.01*	*0.01*		
	Ring	0.09	10.24	0.13	0.00	0.06	0.08	40.84	0.09	48.57	0.05	0.18	0.04	100.37	10
	sigma	*0.01*	*0.02*	*0.01*	*0.00*	*0.00*	*0.01*	*0.05*	*0.00*	*0.06*	*0.01*	*0.01*	*0.01*		
	Maj	0.13	4.66	5.63	0.01	0.31	0.10	54.64	1.75	33.06	0.23	0.02	0.10	100.63	16
	sigma	*0.01*	*0.01*	*0.02*	*0.00*	*0.00*	*0.00*	*0.04*	*0.01*	*0.04*	*0.01*	*0.00*	*0.01*		
	melt	0.12	3.78	3.96	0.01	0.69	0.12	51.53	14.73	21.15	0.33	0.01	0.44	96.89	18
	sigma	*0.01*	*0.01*	*0.01*	*0.00*	*0.00*	*0.00*	*0.04*	*0.03*	*0.03*	*0.01*	*0.00*	*0.01*		
	Pv	0.05	6.03	2.94	0.00	0.31	0.14	50.55	2.75	36.99	0.26	0.00	0.18	100.21	1
	sigma	*0.03*	*0.06*	*0.05*	*0.01*	*0.02*	*0.02*	*0.17*	*0.05*	*0.16*	*0.02*	*0.00*	*0.02*		
GN13	Melt	0.08	4.54	3.95	0.06	0.37	0.03	38.76	0.93	47.04	0.00	0.01	0.05	95.81	3
	sigma	*0.02*	*0.03*	*0.03*	*0.01*	*0.01*	*0.01*	*0.09*	*0.02*	*0.10*	*0.00*	*0.01*	*0.01*		
	Fp	0.05	7.66	1.22	0.00	0.04	0.04	0.25	0.04	90.68	0.08	0.01	0.01	100.09	27
	sigma	*0.01*	*0.01*	*0.01*	*0.00*	*0.00*	*0.00*	*0.00*	*0.00*	*0.05*	*0.00*	*0.00*	*0.00*		
GN23	Melt	0.19	12.17	3.64	0.01	0.19	0.13	43.06	2.40	37.77	0.32	0.02	0.06	99.97	39

Run	Phase[a]	WO_2	FeO	Al_2O_3	K_2O	Na_2O	MnO	SiO_2	CaO	MgO	Cr_2O_3	NiO	TiO_2	Total	N[b]
	sigma	*0.03*	*0.10*	*0.02*	*0.01*	*0.01*	*0.02*	*0.10*	*0.03*	*0.10*	*0.02*	*0.01*	*0.01*		
GN24	Melt	0.17	9.86	2.58	0.00	0.16	0.10	40.69	2.59	42.69	0.16	0.02	0.08	99.10	38
	sigma	*0.04*	*0.15*	*0.05*	*0.01*	*0.02*	*0.03*	*0.38*	*0.05*	*0.46*	*0.03*	*0.01*	*0.02*		
	Fp	0.08	15.32	1.13	0.01	0.05	0.06	0.22	0.03	81.94	0.27	0.02	0.02	99.13	11
	sigma	*0.05*	*0.20*	*0.03*	*0.01*	*0.01*	*0.02*	*0.02*	*0.01*	*0.90*	*0.02*	*0.02*	*0.01*		
GN25	Melt	0.65	14.70	5.72	0.01	0.35	0.12	40.15	2.28	35.66	0.25	0.02	0.04	99.94	22
	sigma	*0.04*	*0.16*	*0.04*	*0.01*	*0.01*	*0.02*	*0.12*	*0.03*	*0.12*	*0.02*	*0.02*	*0.01*		
GN26	Melt	0.54	15.15	4.50	0.01	0.65	0.12	40.46	2.66	35.50	0.30	0.02	0.04	99.95	24
	sigma	*0.04*	*0.16*	*0.03*	*0.01*	*0.01*	*0.02*	*0.12*	*0.04*	*0.12*	*0.02*	*0.01*	*0.01*		
GN30	Melt	0.07	7.32	0.51	0.00	0.04	0.05	40.58	0.33	50.26	0.13	0.01	0.01	99.31	19
	sigma	*0.01*	*0.02*	*0.01*	*0.00*	*0.00*	*0.00*	*0.04*	*0.00*	*0.04*	*0.01*	*0.00*	*0.00*		
	Fp	0.04	16.56	1.25	0.00	0.01	0.08	0.08	0.02	81.49	0.41	0.01	0.01	99.98	5
	sigma	*0.01*	*0.04*	*0.02*	*0.00*	*0.01*	*0.01*	*0.01*	*0.01*	*0.11*	*0.02*	*0.01*	*0.01*		
GN31	Melt	0.13	9.44	0.57	0.00	0.03	0.08	40.29	0.34	48.57	0.13	0.01	0.01	99.59	31
	sigma	*0.01*	*0.01*	*0.00*	*0.00*	*0.00*	*0.00*	*0.03*	*0.00*	*0.03*	*0.01*	*0.00*	*0.00*		
	Fp	0.09	16.60	1.16	0.00	0.02	0.07	0.10	0.01	81.45	0.35	0.01	0.01	99.88	12
	sigma	*0.01*	*0.03*	*0.01*	*0.00*	*0.00*	*0.01*	*0.00*	*0.00*	*0.07*	*0.01*	*0.01*	*0.01*		
GN32	Melt	0.28	8.23	2.62	0.00	0.10	0.07	48.26	3.61	37.74	0.12	0.01	0.09	101.13	46
	sigma	*0.01*	*0.01*	*0.01*	*0.00*	*0.00*	*0.00*	*0.03*	*0.01*	*0.02*	*0.00*	*0.00*	*0.00*		
	Fp	0.05	13.11	0.94	0.00	0.04	0.05	0.18	0.02	87.71	0.15	0.02	0.01	102.30	31
	sigma	*0.00*	*0.01*	*0.01*	*0.00*	*0.00*	*0.00*	*0.00*	*0.00*	*0.04*	*0.00*	*0.00*	*0.00*		
G34	Melt	0.32	32.97	1.24	0.01	0.10	0.27	31.78	1.10	32.42	0.13	0.28	0.10	100.72	20
	sigma	*0.01*	*0.03*	*0.01*	*0.00*	*0.00*	*0.00*	*0.03*	*0.01*	*0.04*	*0.00*	*0.01*	*0.01*		
G34	Fp	0.00	25.50	0.69	0.00	0.12	0.15	0.00	0.15	73.03	0.08	0.29	0.03	100.04	2
	sigma	*0.00*	*0.13*	*0.04*	*0.00*	*0.02*	*0.02*	*0.00*	*0.03*	*0.31*	*0.02*	*0.03*	*0.02*		

Run	*Phase*[a]	*WO_2*	*FeO*	*Al_2O_3*	*K_2O*	*Na_2O*	*MnO*	*SiO_2*	*CaO*	*MgO*	*Cr_2O_3*	*NiO*	*TiO_2*	*Total*	*N*[b]
G36c	Melt	0.69	34.46	1.87	0.00	0.20	0.10	34.25	1.75	24.50	0.10	0.11	0.04	98.05	9
	sigma	*0.01*	*0.05*	*0.01*	*0.00*	*0.01*	*0.01*	*0.05*	*0.01*	*0.05*	*0.01*	*0.01*	*0.01*		
	Fp	0.28	48.36	0.35	0.00	0.22	0.04	0.00	0.81	49.60	0.11	0.22	0.02	100.00	2
	sigma	*0.04*	*0.15*	*0.04*	*0.00*	*0.02*	*0.02*	*0.00*	*0.03*	*0.24*	*0.02*	*0.03*	*0.02*		
G38a	Melt	5.50	12.84	8.33	0.02	1.00	0.10	38.39	5.94	27.10	0.48	0.07	0.24	100.00	11
	sigma	*2.43*	*1.45*	*0.20*	*0.00*	*0.01*	*0.01*	*1.30*	*0.43*	*0.42*	*0.01*	*0.00*	*0.04*		
G38b	Melt	1.01	34.01	0.67	0.01	0.05	0.12	32.03	0.20	31.61	0.04	0.17	0.00	99.93	3
	sigma	*0.05*	*1.00*	*0.11*	*0.00*	*0.00*	*0.01*	*0.57*	*0.06*	*0.27*	*0.01*	*0.01*	*0.00*		
G39a	Melt	0.11	26.64	2.14	0.02	0.89	0.26	36.88	3.71	27.73	0.20	0.26	0.12	98.96	15
	sigma	*0.02*	*0.20*	*0.02*	*0.00*	*0.01*	*0.01*	*0.07*	*0.03*	*0.17*	*0.01*	*0.01*	*0.01*		
GPC2	Melt	2.05	18.74	5.92	0.02	0.50	0.14	32.75	5.41	35.74	0.19	0.01	0.18	101.65	59
	sigma	*0.01*	*0.02*	*0.01*	*0.00*	*0.00*	*0.00*	*0.03*	*0.01*	*0.03*	*0.00*	*0.00*	*0.00*		
GPC3	Melt	0.64	21.80	6.69	0.02	0.64	0.14	31.06	6.85	31.83	0.16	0.01	0.22	100.06	80
	sigma	*0.01*	*0.02*	*0.01*	*0.00*	*0.00*	*0.00*	*0.02*	*0.01*	*0.02*	*0.00*	*0.00*	*0.00*		
GPC4	Melt	4.99	16.19	6.90	0.01	0.48	0.14	30.06	5.28	35.72	0.25	0.01	0.19	100.22	55
	sigma	*0.01*	*0.02*	*0.01*	*0.00*	*0.00*	*0.00*	*0.03*	*0.01*	*0.03*	*0.00*	*0.00*	*0.00*		
GPC6	Melt	0.16	16.39	0.54	0.01	0.04	0.11	39.62	0.48	43.73	0.20	0.00	0.01	101.28	11
	sigma	*0.03*	*0.03*	*0.01*	*0.00*	*0.01*	*0.01*	*0.05*	*0.01*	*0.06*	*0.01*	*0.00*	*0.01*		
GPC7	Melt	0.28	15.66	0.78	0.01	0.03	0.09	38.82	0.73	43.70	0.17	0.01	0.03	100.31	13
	sigma	*0.03*	*0.03*	*0.01*	*0.00*	*0.00*	*0.01*	*0.04*	*0.01*	*0.05*	*0.01*	*0.00*	*0.01*		

[a]Aki = akimotoite; Fp = ferropericlase; Maj = majorite; Mw = magnesiowüstite; Ring = ringwoodite; Pv = Mg silicate perovskite. [b]Number of microprobe measurements made on the indicated phase. [c]Mg silicate perovskite identified by Raman spectroscopy, and stoichiometry determined from microprobe data suggests replacement of olivine by perovskite and magnesiowüstite intergrowths.

Table 5. Compositions of metals as measured using electron microprobe. Abundances are in weight percents.

Run#		*Fe*	*Cr*	*W*	*Mo*	*Ni*	*C*	*S*	*O*	*Si*	*Total*	*N*
GN10	metal	83.37	0.01	14.40	0.93	0.33					99.04	17
	sigma	*0.04*	*0.00*	*0.04*	*0.01*	*0.01*						
GN11	metal	81.78	0.06	16.19	0.88	0.47					99.39	38
	sigma	*0.03*	*0.00*	*0.03*	*0.01*	*0.00*						
GN13	metal	80.19	0.12	16.68	0.97	0.48					98.44	24
	sigma	*0.03*	*0.00*	*0.03*	*0.01*	*0.01*						
GN23[a]	metal	79.25		13.87	0.83	0.26	5.56	0.23			100.00	0
	sigma											
GN24	metal	82.65	0.04	15.82	1.17	0.53					100.21	42
	sigma	*0.33*	*0.01*	*0.28*	*0.09*	*0.04*						
GN25[a]	metal	79.19		13.71	0.85	0.27	5.73	0.24			100.00	0
	sigma											
GN26[a]	metal	78.97		13.91	0.86	0.27	5.75	0.24			100.00	0
	sigma											
GN30	metal	78.68	0.02	18.16	0.90	0.50					98.25	20
	sigma	*0.04*	*0.00*	*0.03*	*0.01*	*0.01*						
GN31	metal	79.86	0.02	16.54	1.02	0.41					97.84	30
	sigma	*0.03*	*0.00*	*0.02*	*0.01*	*0.00*						
GN32	metal	79.27	0.02	17.68	0.98	0.51		0.07	0.51		99.04	22
	sigma	*0.04*	*0.00*	*0.03*	*0.01*	*0.01*		*0.00*	*0.01*			

Run#		*Fe*	*Cr*	*W*	*Mo*	*Ni*	*C*	*S*	*O*	*Si*	*Total*	*N*
G34	metal	77.04	0.10	0.04		0.98	14.34	1.06	6.62		100.18	8
	sigma	*0.08*	*0.01*	*0.04*		*0.01*	*0.11*	*0.01*	*0.09*			
G36c	metal	84.31	0.04	1.95		1.11	8.54	0.84	3.10	0.10	100.00	11
	sigma	*0.10*	*0.00*	*0.03*		*0.01*	*0.07*	*0.00*	*0.03*	*0.01*		
G38a	metal	28.37	0.29	59.35		0.35	1.72	0.07	7.63	1.83	99.62	11
	sigma	*0.03*	*0.01*	*0.08*		*0.01*	*0.00*	*0.00*	*0.02*	*0.01*		
G38b	metal	66.60	0.01	19.80		2.11	8.99	2.19	0.31		100.00	7
	sigma	*4.51*	*0.01*	*1.54*		*0.10*	*5.70*	*0.14*	*3.07*			
GPC2	metal	96.75	0.01	3.04		0.51		0.05	0.43		100.78	25
	sigma	*0.04*	*0.00*	*0.02*		*0.00*		*0.00*	*0.01*			
GPC3	metal	98.12	0.00	0.54		0.55		0.05	0.62		99.88	18
	sigma	*0.05*	*0.00*	*0.02*		*0.01*		*0.00*	*0.01*			
GPC4	metal	86.98	0.01	11.68	1.04	0.50		0.07	0.56		100.82	21
	sigma	*0.04*	*0.00*	*0.03*	*0.01*	*0.01*		*0.00*	*0.01*			
GPC6	metal	85.52	0.04	6.14		0.50	6.66	0.03	1.06		100.00	10
	sigma	*0.06*	*0.00*	*0.04*		*0.01*	*0.01*	*0.00*	*0.01*			
GPC7	metal	89.57	0.01	4.28		0.33	5.37	0.03	0.38		100.00	11
	sigma	*0.05*	*0.00*	*0.04*		*0.01*	*0.00*	*0.00*	*0.01*			

[a]Metal compositions for GN23, GN25, and GN26 were estimated by mass balance using starting powder mixture composition and compositional measurements of quenched silicate melt. Carbon saturation of metals was assumed in these calculations because experiments were conducted in graphite capsules.

2.5.1 Analytical Element Suite

Non-metallic phases in samples were analyzed for the following elements: Fe, Si, Mg, Ca, Al, Ni, Cr, Ti, Mn, Na, K, and W. All of these except for W were present in the tabulated natural peridotite starting materials at approximately weight percent abundances (Rudnick et al, 2004). Tungsten abundance was not determined in the starting materials, but it is assumed to be present at the parts per billion level common to peridotites. All metals were analyzed for Fe, W, Ni, Cr, Si, and Mg. Most MAP samples contained Mo in the starting materials and those samples were analyzed for Mo. The inclusion of Mg and Si was to detect signal from silicate materials, and in the case of Si to determine possible Si dissolution in the metal phase. Additionally, some samples were analyzed for O and S, because these had been detected in metals of LHDAC samples, and were subsequently included in the metals suite.

2.5.2 Standardization

Standards for the majority of the elements in the analytical suite were common between the work done on JEOL and Cameca machines, and these are shown in Table 3. However, note the different W standard for silicate analyses; scheelite on the JEOL and W metal on the Cameca. It appears that this was an important difference, particularly where W abundances in the silicate were low and closer to detection limits. The analytical uncertainties on measurements of W under those conditions were consistently lower for samples analyzed on the JEOL versus the Cameca machine.

2.5.3 LHDAC Samples

Initially I expected that the microprobe would be unsuitable for analyzing LHDAC samples, and that these would require use of an analytical TEM. However, I have found through analysis of five FIB-sectioned samples that the microprobe is well suited to analysis of these samples. Analytical uncertainties were on par with those in MAP and PC samples, and spatial resolution was approximately one micron. This level of spatial resolution was evident in transects where distinct changes in composition could be seen across phase boundaries within distances of approximately one micron. Two examples are shown in Figure 11 for sample G39 where the transects cross phase boundaries between silicate melt and the surrounding crystalline materials that are clearly distinguished by Z-contrast and texture.

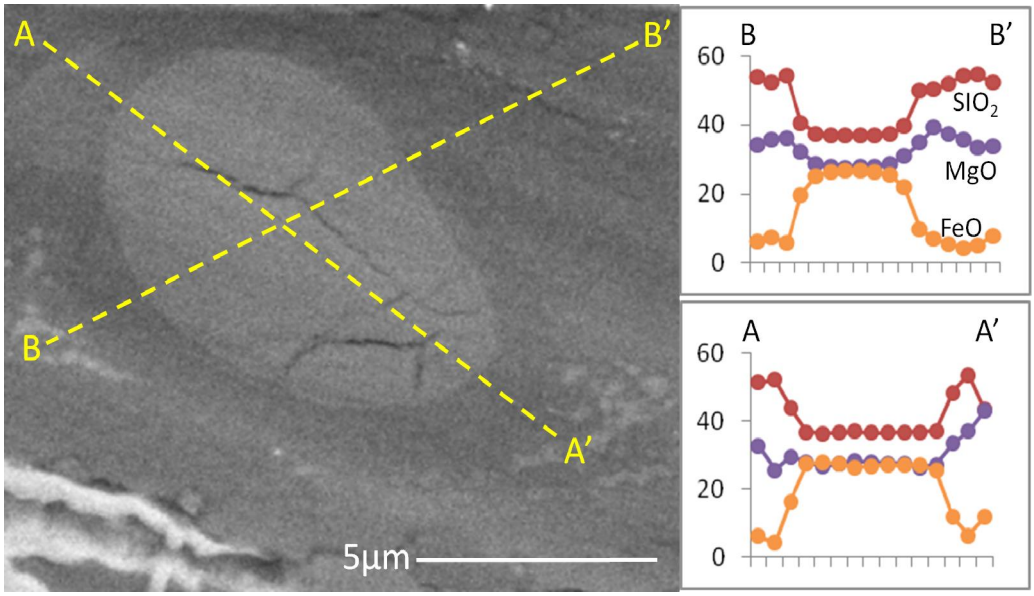

Figure 11. Analytical transects using microprobe on FIB-sectioned LHDAC sample G39, shown in backscattered electron image. Horizontal scales on composition plots are distances along transects, with measurements spaced approximately every 0.8 microns.

2.6 Synchrotron X-ray Diffraction

In order to calculate thermal equations of state (EOS) and oxygen fugacity buffers for the W-WO_2 system, x-ray diffraction data were collected on coexisting W and WO_2 (see Figure 12 for P-T space distribution of data).

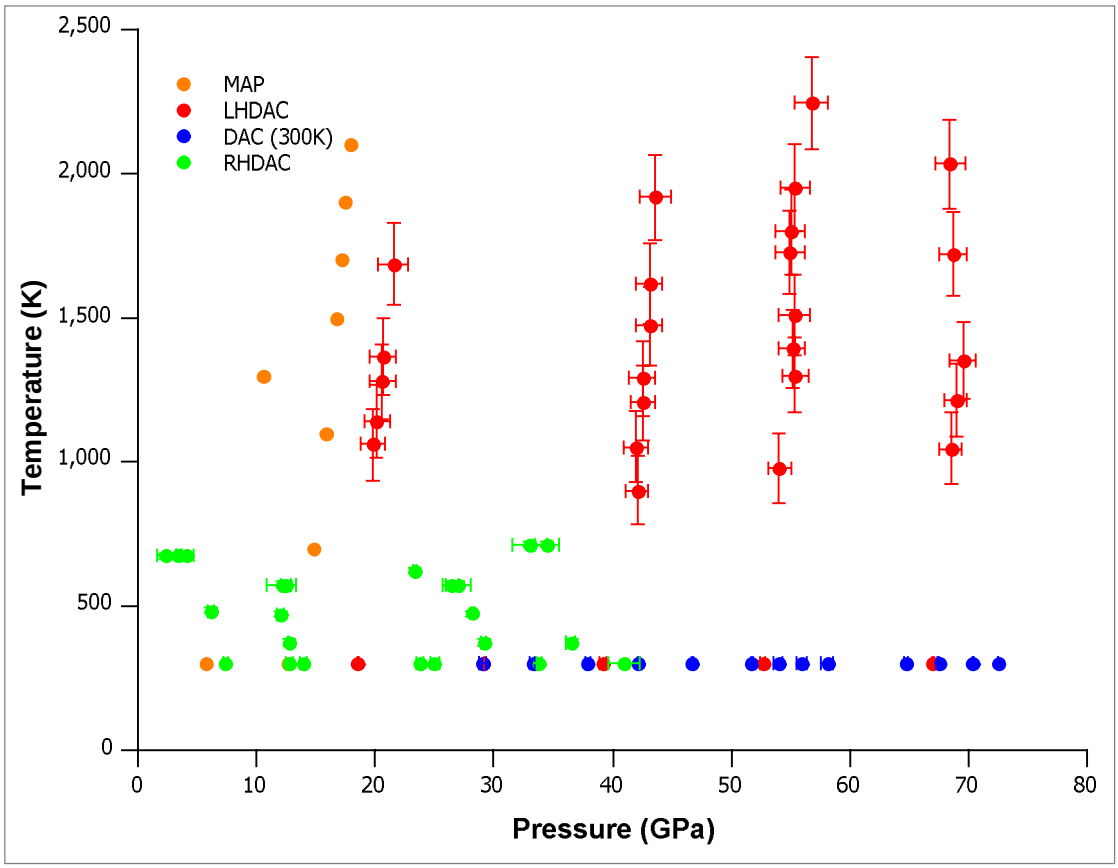

Figure 12. Pressure and temperature distributions of x-ray diffraction experiments. MAP – multi-anvil press, LHDAC- laser-heated diamond anvil cell, RHDAC – resistively-heated diamond anvil cell, and DAC 300K – room-temperature compression in diamond anvil cell.

These data were at collected high pressures and temperatures using diamond anvil cells and a multi anvil press at beamline X17C of the National Sychrotron Light Source (NSLS), Brookhaven National Lab, and at beamline 13-ID-D of the Advanced Photon Source (APS), Argonne National Lab. Because of the small sample volumes in DAC and MAP experiments, the high photon flux and high energy of synchrotron x-radiation

are required. Making measurements of both metal and oxide in the same experiment is important because the oxygen fugacity buffer is defined in terms of the equilibrium between metal and oxide. It is also advantageous that both phases are present under the same experimental conditions in EOS calculations because the volume difference (ΔV) between the phases are referenced to exactly the same P-T conditions. This results in lower measurement uncertainties and hence lower propagated uncertainties in the EOS calculations.

2.6.1 Room Temperature Compression

Room temperature compression provides the foundation for the thermal EOS. Coexisting W and WO_2 were compressed in DACs using an argon pressure medium over a pressure range of approximately 25 to 73 GPa. X-ray diffraction data were collected at discrete pressures on beamline X17C at NSLS using angle-dispersive diffraction with diffraction patterns collected on an area CCD x-ray detector. These x-ray diffraction data were used to determine unit cell volumes of the individual phases. Helmholtz free energy and finite strain terms were calculated from these data and were fit using a least squares minimization. From these fits, parameters for third order Birch-Murnaghan EOS were calculated (Birch, 1952). Experimental pressures were determined using Pt as a pressure calibrant (Fei et al., 2007). As discussed in later sections, the room temperature EOS for WO_2 is complicated by phase transitions including coexisting crystal structures.

2.6.2 High Temperature Experiments

With only room-temperature data, the EOS for these systems are not sufficient for extrapolation to high temperature conditions. High temperature experiments were made using laser-heated DAC, MAP, and externally-heated DAC.

2.6.2.1 LHDAC

Laser-heated DAC experiments were conducted in February 2010 at APS on coexisting W and WO_2 where x-ray diffraction data were collected at temperatures up to 2300 K and at pressures up to approximately 70 GPa. The sample was insulated between layers of NaCl, which also served as the pressure calibrant (Decker 1971; Fei 2007) . The laser-heating system at APS allows for simultaneous heating and x-ray diffraction. This is achieved through the use of x-ray transparent optics that direct twin lasers onto opposite sides of the sample for double-side heating allowing the laser and x-ray beams to be coaxial (Shen et al., 2001). Four heating cycles were made with starting pressures at ambient temperature of approximately 18, 39, 53, and 67 GPa. A heating cycle was not made in the pressure range around 30 GPa to avoid the pressure range of the B1 to B2 phase transition in NaCl, which complicates pressure determination due to coexistence of the two structures (Heinz and Jeanloz 1984). Laser power was gradually increased and diffraction patterns were collected up to the peak temperature for a given pressure step. The laser power was then decreased gradually and diffraction patterns were collected approximately every 100 degrees. The pressure in the diamond cell was increased at room temperature between each heating cycle. The diffraction data from the cooling portion of each heating cycle were used in EOS calculations. This is because non-hydrostatic stresses tend to be developed following

cold compression, which can adversely affect measured lattice spacings and consequently lead to errors in calculated unit cell volumes, ultimately propagating to EOS calculations. At high temperatures the non-hydrostatic stresses are relaxed, improving the quality of the diffraction data. The diffraction data were measured using an angle-dispersive configuration and diffraction spectra were collected using a CCD x-ray area detector.

2.6.2.2 MAP

Diffraction data can be collected in the MAP using a special octahedral assembly. Modifications to the standard octahedral assembly are required to allow passage of the x-ray beam and diffracted x-radiation resulting from interaction of the beam with the sample. This is particularly important due to the presence of the Re heater, which strongly diffracts x-rays. Additionally, the LaCrO3 sleeve in the standard configuration would attenuate the x-ray diffraction signal and contribute to the diffraction spectrum, thus complicating identification of the experimental phases. In the beamline octahedral assembly, the LaCrO3 sleeve and the Re furnace contain slots on opposing sides that allow passage of the x-ray beam, which ideally interacts with the sample and sample capsule only. Boron nitride capsules were used because their low mean atomic number results in minimal attenuation of the x-ray beam. The entire cube assembly is aligned in a specific configuration to allow the x-ray beam to pass between the gaps of the WC cubes and through the aperture in the octahedral assembly. Diffracted x-rays were detected using a cooled Ge energy-dispersive detector placed a fixed 2-theta angle relative to the incoming x-ray beam. By calibrating the detector at this angle and

distance to the sample, the resulting energy spectrum can be converted to a intensity versus *d*-spacing spectrum.

MAP experiments were conducted in November 2010 using the large volume press at beamline 13-ID-D at APS. The sample capsule contained a mixture of W and WO_2. Pressure calibration was by MgO where experimental pressures were calculated using a thermal EOS for MgO (Speziale, 2001). Diffraction data were collected at temperatures up to 2100 K and 18 GPa. Two heating cycles were made at press forces of 800 and 400 tons. Similar to LHDAC experiments, data were collected on the heating and cooling portions of each cycle but the cooling data was used in EOS calculations. It was noted during the second cycle that the W diffraction peaks were weakening in relative intensity to those of WO_2. The decision was made to heat to 2100 K and decompress the experiment at constant temperature; data were collected at press forces of 350, 300 and 270 tons. At 270 tons press force, temperatures were slowly decreased and data were collected at approximately 200 degree intervals. It is uncertain why W diffraction intensities decreased so significantly, but the WO_2 remained a stable phase as shown by successful indexing of the diffraction data to the published orthorhombic structure (Sundberg et al. 1994).

2.6.2.3 Externally-Heated DAC

An external heating system was developed in the UMD Laboratory for Mineral Physics that allowed for sample chamber temperatures up to approximately 450ºC. The final external heater production design at UMD was the result of several months of research and development. Various heater block/cell holder and heater geometries were explored. An undergraduate worker was employed to assist with fabrication and testing.

Also investigated were various gasket geometries. The first design was a torus-like ring that surrounded the gasket and was located between the diamond anvils. This had the advantage of only requiring the gasket and diamonds to be heated and minimized the heating of the metal cell. This was a desirable feature to minimize the thermal expansion of the metal parts of the cell, which can result in lowering of the pressure in the sample chamber during heating. The complication with this geometry was sample loading. The ring heater needed to be emplaced around the gasket and on top of the lower diamond before assembling the cell. Attempts were made to load the DAC using this heater geometry, but the cell loading success rate was low. Therefore another heater geometry was explored. This second, and ultimately the production design, involved heating the entire DAC (Figure 13). In this geometry, the DAC is flanked by two thin heaters one on each side and parallel to the plate surfaces of the DAC. This

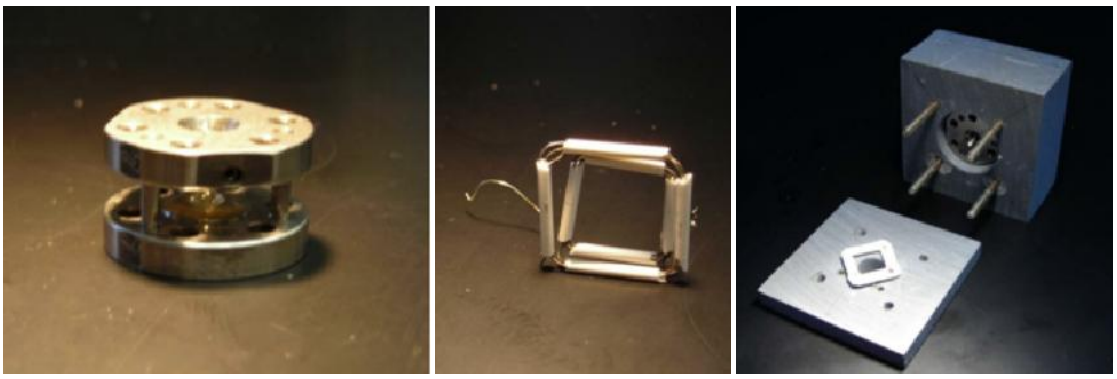

Figure 13. Resistive external heater for DAC. The images from left to right show: a three-post Inconel DAC; the resistive heater with alumina tubing for electrical insulation; and the DAC and heater installed inside of pyrophyllite block.

geometry has the major advantage of making cell loading easier. Cell loading is done in the typical fashion and does not require the added complication of mounting the heater around the diamond anvils and gasket. The main disadvantage is that since the entire cell heated, the resulting thermal expansion of the cell results in a decrease in

sample chamber pressure during heating. X-ray diffraction data were collected at beamline X17C at NSLS. Diffraction patterns were collected at discrete temperatures and at four different starting pressures.

3 Metal/Silicate Partitioning of Tungsten

3.1 Experimental Results

The experimental P–T space of my metal/silicate partitioning experiments is shown in Figure 14. The regions covered by MAP and DAC experiments are indicated; note that only analyzed samples are included on this plot. The liquidus and solidus of peridotite are shown for reference. Compositions of silicate and metallic phases are reported in Tables 4 and 5.

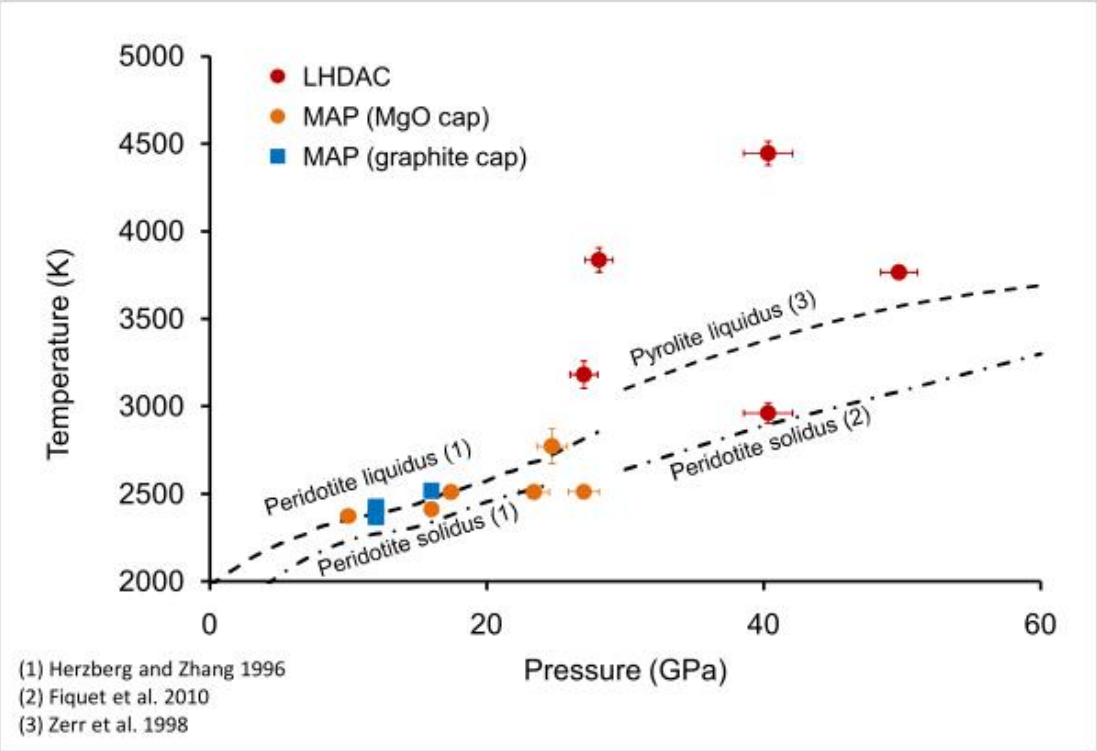

Figure 14. Experimental P-T space of metal/silicate partitioning experiments. The location of the piston cylinder experiments are not shown.

The experimental goal was to minimize the range of experimental temperature, silicate composition and oxygen fugacity to isolate the P effect, but experimental

realities did not allow this across the entire experimental P–T space. The range of pressure covered was 10 to 50 GPa, and the temperature range of the peridotite liquidus over this pressure range is approximately 1000°. However, this was realized for two of the DAC experiments (G36 and G34), which were similar in temperature, composition, and fO_2, and most of the MAP experiments were within a temperature range of 150°. In general, MgO capsule runs were enriched in MgO and depleted in FeO relative to starting compositions, except for the low melt fractions experiments (GN10 and GN11) which where enriched in CaO and SiO_2 and highly depleted in MgO; graphite capsule runs had quenched silicate melt compositions that were very similar to starting materials except for depletion in FeO; and DAC runs were slightly depleted in SiO_2, enriched in FeO and depleted in MgO relative to starting silicate compositions.

3.1.1 Multi-anvil Press (MAP)

I conducted 32 MAP experiments. The first 12 experiments were developmental runs to establish experimental methods for the P-T conditions of interest, which reached the limits of the MAP capability. Fifteen of the 32 experiments failed, most often due to loss of melt containment, but in a few cases due to other factors including experimental error that resulted in no heating. Electron microprobe analyses were obtained on 13 samples that contained silicate melt, three of which were experiments done using BN capsules, and for reasons described in Section 2.1.1 the analytical data are not reported here. Some samples were not analyzed due to lack of silicate melt. The pressure range for all experiments was from approximately 10 to 27 GPa. Peak temperatures attained in the analyzed experiments ranged from approximately 2,100 to 2,700 K.

Experimental conditions and sample assembly geometries are shown in Table 1. The positions of these experiments in P–T space is shown in Figure 14.

For experiments GN24 to GN32, iron (II) oxide was added to the starting powder mixture (Table 1) to both promote lowering of the liquidus temperature and, thus, aid in melting the sample charge, and to control fO_2 to a value of approximately IW-2. An fO_2 of approximately IW-2 is consistent with the modern mantle, and is thought to be appropriate to the conditions of Earth's core formation (Cottrell et al., 2009), or at least the later stages of core formation (Wood, 2008; Rubie et al., 2011). Metals consisted of Fe and W at a ratio of approximately five to one by weight. The silicate (including added FeO) to metal ratio was approximately two to one. Less than one weight percent Mo metal was also added to all MAP with the forethought of possibly collecting Mo partitioning data (Table 2). Abundances of Mo in the metal phase were measured in all samples, but not in the silicate phases because they were below the detection limit of the microprobe.

As discussed in Chapter 2, the most suitable sample capsule was found to be single crystal MgO. An example of an experiment in this capsule type was GN24, which is shown in Figure 15. Experimental conditions were 16 GPa and approximately 2400 K. The phases present were quenched silicate melt (showing crystalline quench texture characteristic of peridotite) and metallic liquid with ferropericlase (Fp) crystals concentrated around the metal blobs. The metals are an alloy of Fe and W exhibiting exsolution with regions of higher and lower W concentrations, the brighter material has a composition of approximately 70 weight percent Fe and 30 weight percent W, and the darker regions approximately 85 weight percent Fe and 15 weight percent W. The

average composition of the metal phase was calculated using a weighted average based on 85% of the low-W phase and 15% of the high-W phase. This distribution of the exsolved metal phases was determined by image analysis of a BSE image of the sample, where the phases were discriminated based on Z-contrast, and the volumetric distribution was assumed to be represented by the 2-dimensional distribution exposed at the polished surface of the sample. This same type of analysis was used in determination of compositions of quenched metallic liquids in other MAP samples that exhibited metallic phase exsolution. The Fp grains contain approximately 15 weight percent FeO and one weight percent Al_2O_3. This abundance of Al_2O_3 was measured in Fp in other samples too. All of the starting materials likely melted in this sample, based on the ubiquitous quench texture in the silicate fraction of the run phases.

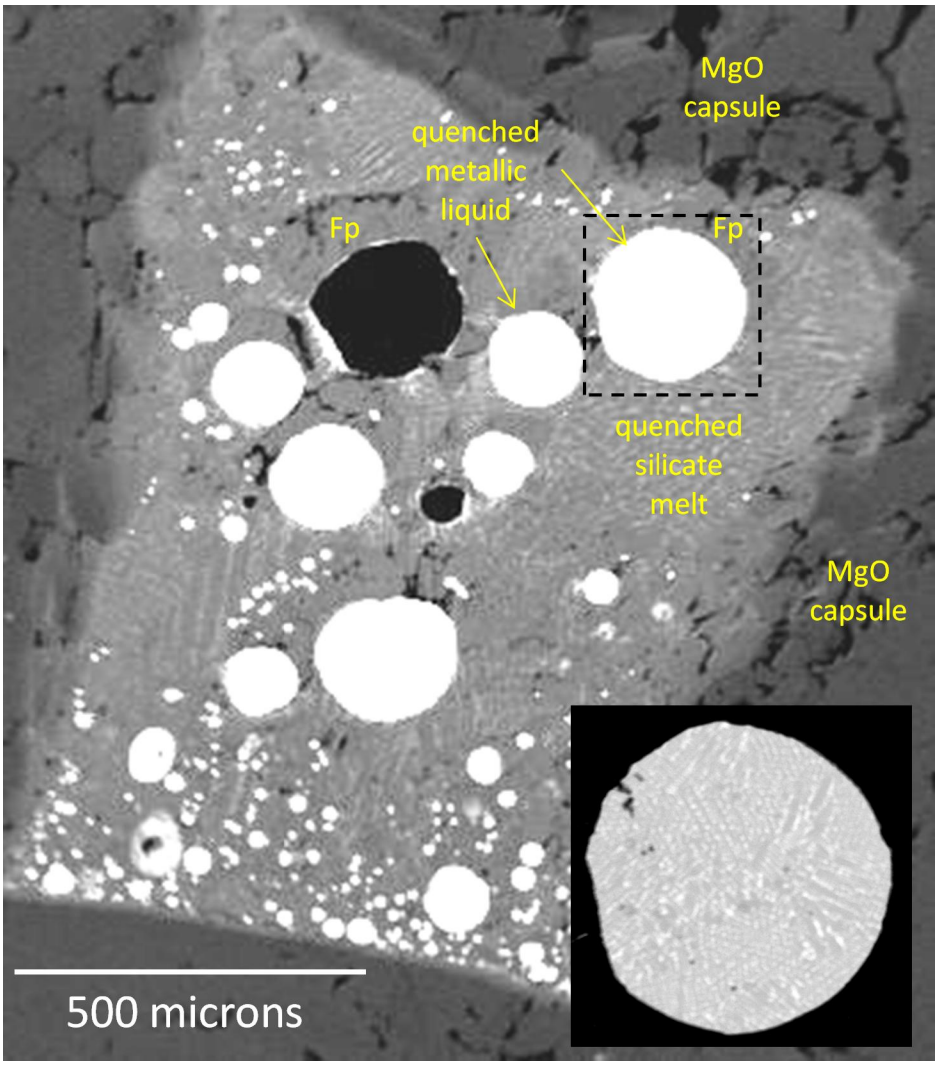

Figure 15. Back scattered electron images of MAP sample GN24. Image to lower right shows exsolution in quenched metallic liquid where the brighter regions contain approximately 30 wt% W, and the grey regions contain approximately 15 wt% W.

In contrast to sample GN24, samples GN10 and GN11 exhibited very low silicate melt fractions. Sample GN10 is shown in Figure 16 and the small regions of melt are highlighted. These regions were first identified as melt based on stoichiometry determined form microprobe results and later confirmed as melt by Raman spectroscopy using a Raman microscope at NASA JSC. The other crystalline phases

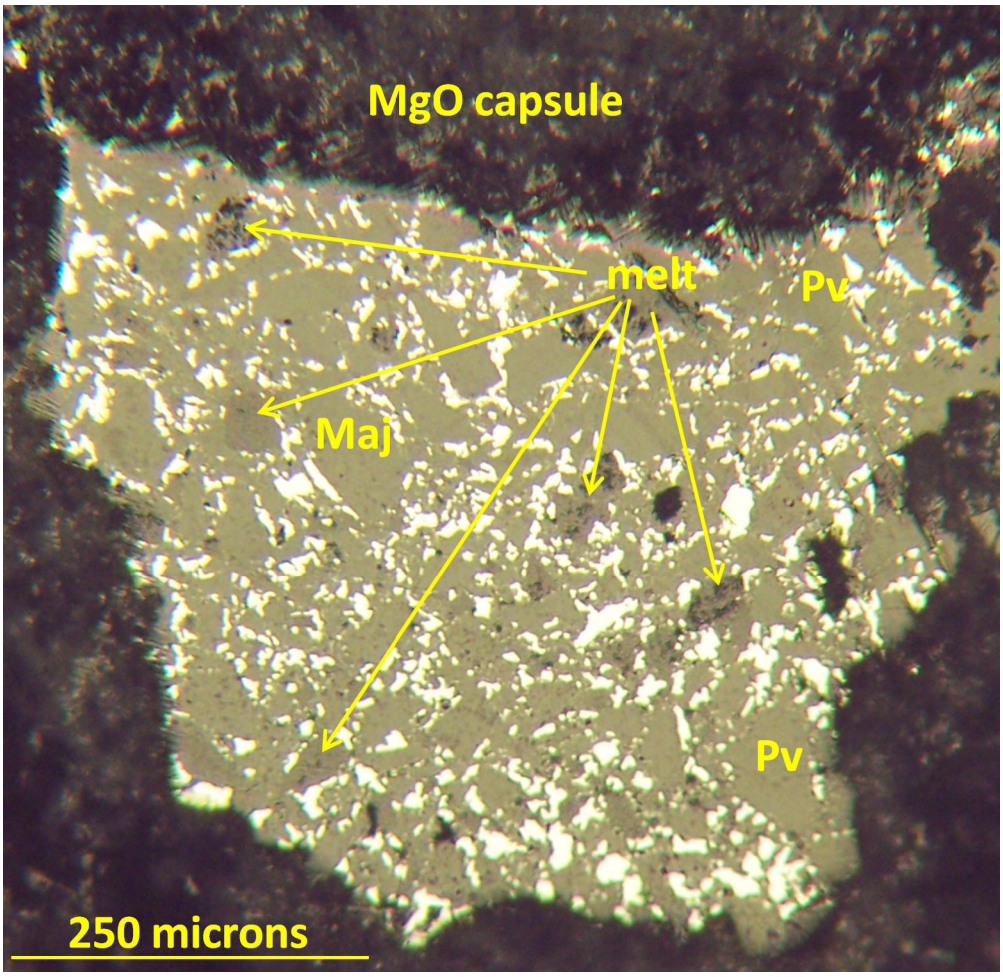

Figure 16. Reflected light image of MAP sample GN10. The melted silicate regions are indicated either by yellow label or pointed to by yellow arrows. Other silicate phases are shown by labels: Pv – perovskite, and Maj – majorite. The highest reflectance regions are Fe-W metallic alloy.

in this sample, as well as the phases in GN11, were also identified by Raman spectroscopy. The phase assemblages in these samples are listed in Table 6. The low melt fraction in these samples contributed to their silicate melt compositions being enriched in CaO relative to all other MAP samples.

Table 6. Experimental phases, oxygen fugacities (expressed relative to the IW buffer), molar partition and exchange coefficients.

Run#	*Phase*	*ΔIW*	*sigma*	*log D* (W)*	*sigma*	*log Kd (W)*	*sigma*
GN10	Melt	-3.03	0.00	2.16	0.04	-0.87	0.04
	Pv[a]	-2.25	0.00	2.34	0.02	0.09	0.02
	Maj	-2.63	0.00	2.31	0.04	-0.32	0.04
	Pv	-2.52	0.01	2.10	0.08	-0.42	0.08
	Aki	-1.82	0.01	1.90	0.08	0.08	0.08

GN11	Melt	-2.94	0.00	2.29	0.04	-0.65	0.04
	Ring	-2.24	0.00	2.43	0.05	0.19	0.05
	Fp	-2.13	0.00	2.40	0.04	0.26	0.04
	Maj	-2.87	0.00	2.26	0.03	-0.61	0.03
	Pv	-2.66	0.01	2.66	0.26	-0.01	0.26
	Aki	-1.88	0.01	1.97	0.08	0.09	0.08
GN13	Melt	-2.55	0.00	2.29	0.03	-0.26	0.03
	Fp	-2.63	0.00	2.82	0.05	0.19	0.05
GN23	Melt	-1.82	0.02	1.91	0.05	0.09	0.05
GN24	Melt	-2.24	0.01	2.11	0.16	-0.13	0.16
	Fp	-1.99	0.01	2.53	0.30	0.54	0.30
GN25	Melt	-1.62	0.03	1.37	0.06	-0.25	0.07
GN26	Melt	-1.60	0.03	1.46	0.06	-0.14	0.07
GN30	Melt	-2.52	0.00	2.63	0.04	0.11	0.04
	Fp	-1.91	0.00	2.92	0.16	1.00	0.16
GN31	Melt	-2.31	0.00	2.30	0.02	-0.01	0.02
	Fp	-1.92	0.00	2.51	0.05	0.59	0.05
GN32	Melt	-2.38	0.00	2.01	0.01	-0.37	0.01
	FP	-2.11	0.04	2.85	0.06	0.74	0.07
G34	Melt	-0.52	0.00	-0.53	0.17	-1.04	0.17
	Fp[a]	-0.89	0.00	–	–	–	–
G36c	Melt	-0.68	0.00	0.36	0.01	-0.31	0.01
	Fp	-0.78	0.01	0.80	0.06	0.02	0.06
G38a	Melt	-1.00	0.10	1.14	0.19	0.14	0.21
G38b	Melt[b]	-0.64	0.30	1.30	0.15	0.66	0.34
G39a	Melt[c]	–	–	–	–	–	–
GPC2	Melt	-1.66	0.06	0.24	0.05	-1.42	0.07
GPC3	Melt	-1.50	0.04	0.00	0.04	-1.50	0.06
GPC4	Melt	-1.70	0.06	0.46	0.06	-1.24	0.09
GPC6	Melt	-1.56	0.01	1.64	0.08	0.08	0.08
GPC7	Melt	-1.67	0.00	1.25	0.05	-0.42	0.05

[a]Partition coefficients for Fp in G34 could not be calculated due to no detection of W. [b]Partition coefficients and fO_2 estimate for G38b likely do not reflect metal-silicate equilibrium, see text for discussion. [c]Partition coefficients and fO_2 were not calculated due to lack of metallic phase in sectioned part of the laser-heated spot.

3.1.2 Laser-heated Diamond Anvil Cell (LHDAC)

I conducted a total of 40 LHDAC experiments. Approximately 75% of these were developmental runs in which various pressure media, starting compositions, and sample loading geometries were explored. Six of the ten production runs have been sectioned and five of those have been analyzed for chemical composition. Tight scheduling and high demand for access to the FIB facility at NASA Johnson Space Center were the main limiting factors on the number of analyzable LHDAC samples. Three of the five

analyzed samples (G34, G36c, and G38a) yielded data that allowed calculation of W partition coefficients, while the remaining two samples (G38b and G39a) provided useful information about W solubility in silicate melts, the analytical precision of applying EMPA to LHDAC samples, and about the geometry of the laser-heated regions in the DAC experiments.

Figure 17 shows a backscattered electron image of an example LHDAC sample. Experimental conditions were 28 GPa and about 3800 K. The section was cut parallel to the laser-heating axis (shown by red arrows) and so shows both the on-axis and radial structure of the laser-heated spot. The phases present are quenched silicate melt, quenched metallic liquid, and ferropericlase. The ferropericlase forms a rim around the quenched silicate melt, and contains approximately 35 weight percent FeO. The metal alloy is saturated with respect to C and also contains approximately three weight percent oxygen. Analytical transects across this sample in approximately E-W and N-S orientations relative to the image in Figure 17, showed uniform composition. Transects across the metal region in similar orientations showed uniform composition in the metal.

The experimental temperature of LHDAC sample G34 was also approximately 3800 K, though the pressure was approximately 40 GPa. The silicate melt composition of G34 was very similar to that of G36 and showed uniformity across analytical transects. The metal composition of G34 differed both in its W abundance, which was approximately 400 ppm compared to approximately two weight percent in G36. The measured oxygen content of G34 was approximately six weight percent, which is twice that of G36. The oxygen solubility indicated in these two samples is in good agreement

with the predictions of Rubie et al. (2004). Also the inferred carbon content of G34 was higher than G36. The different texture of the metals in G34 compared to G36 suggests the presence of carbides in G34 that likely contributed to the greater carbon content (Figure A-1). Figure A-2 shows the temperature map for G34 that illustrates the physical correlation between the metallic melt and the highest temperature region of the laser-heated spot.

Experiment G38 included two laser-heated regions, identified as LHDAC samples G38a and G38b (Figures A-3 and A-4). While G38a and G38b were at the same experimental pressure, they differed in temperature by approximately 1500 K (Table 1). Sample G38a, with an experimental temperature of approximately 4400 K, differs from all other LHDAC samples both in its high temperature, and overall high W abundance (Tables 4 and 5). This high W abundance was likely the result of heterogeneity in the starting materials. The O content of G38a was the highest of the LHDAC samples at approximately 8 wt%, but the estimated C content was lower than other LHDAC samples at approximately 2 wt%. Sample G38b, at a temperature of approximately 3000 K, exhibited low silicate melt fraction and consequently did not have a metallic sphere like the other LHDAC samples. Quenched silicate liquid in G38b was identified based on texture and similarity to G34 and G36c. The composition of metallic regions in G38b were very similar to starting materials and, based on the FIB section, the silicate melt and metallic regions do not appear to have been in physical contact. Therefore, the silicate and metallic melts were likely not in equilibrium. The W metal/silicate partition coefficient for G38b did not fit the trend of other LHDAC and MAP samples, supporting the interpretation of disequilibrium.

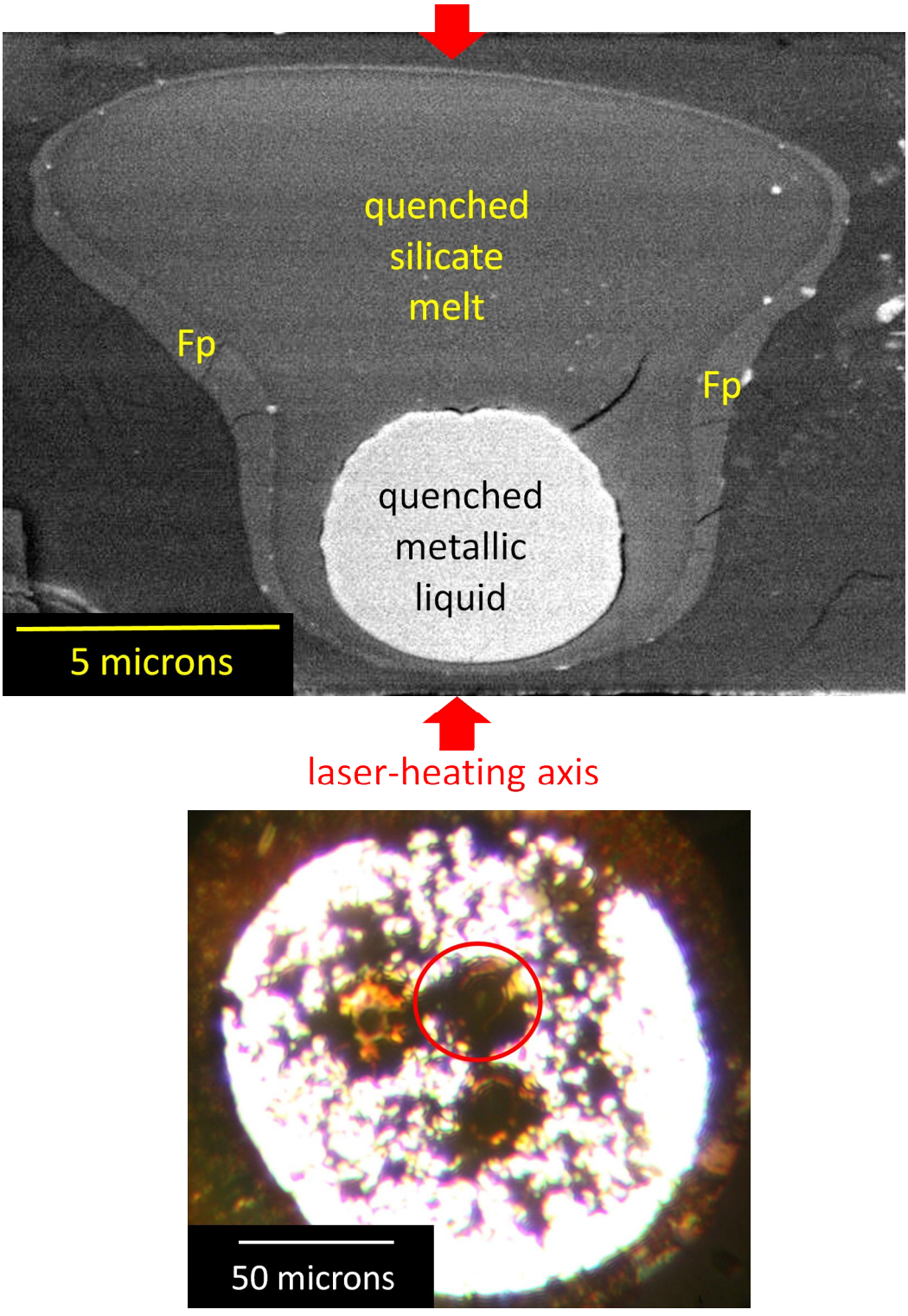

Figure 17. LHDAC sample G36c. Upper view is a backscattered electron image of FIB section. Lower view is an optical image taken while sample was under pressure in the DAC. Red circle indicates location of laser-heated spot where FIB section was taken. Fp – ferropericlase.

3.1.3 Piston Cylinder (PC)

I conducted five PC experiments. These were directed at examining two specific problems: 1) assessing Henry's Law behavior of tungsten at the weight percent levels typical of my experiments, and 2) assessing equilibrium through reversal experiments.

The Henry's Law set of experiments consisted of three runs with identical silicate starting compositions and silicate to total metal weight fractions of approximately 70/30. The only variable was the Fe to W ratio with starting W concentrations of 5.1, 1.5 and 0.31 weight percent. These experiments were conducted using MgO capsules. Peak temperatures were 1750 ℃ and pressures ranged from 0.9 to 1.1 GPa. The heating cycles up to peak temperatures were 40 minutes, and the experiments were held at peak temperatures for 30 minutes.

The reversal experiments had similar silicate compositions and silicate to metal ratios. They differed only in including W metal versus WO_2 in the starting materials, where the W abundances in the starting materials were set to provide equivalent molar proportions of W in both experiments. The experiments were conducted in graphite capsules. Peak temperatures were 1800 °C and pressures were 1 GPa.

3.1.3.1 Samples GPC2-GPC4

These samples comprised the experiment set to assess Henry's Law behavior of W. Samples GPC3, GPC2, and GPC4 contained 0.31, 1.5, and 5.1 weight percent W in their starting materials, respectively. All runs exhibited essentially identical phase assemblages consisting of quench metallic liquid, quench silicate liquid, ferropericlase, and euhedral olivine grains. The metal phase is present in the run products as spherical blebs ranging in size from a few tens of microns to over 500 microns. Figure 18 shows

sample GPC2 as an example of the textures and phases present in these experiments.

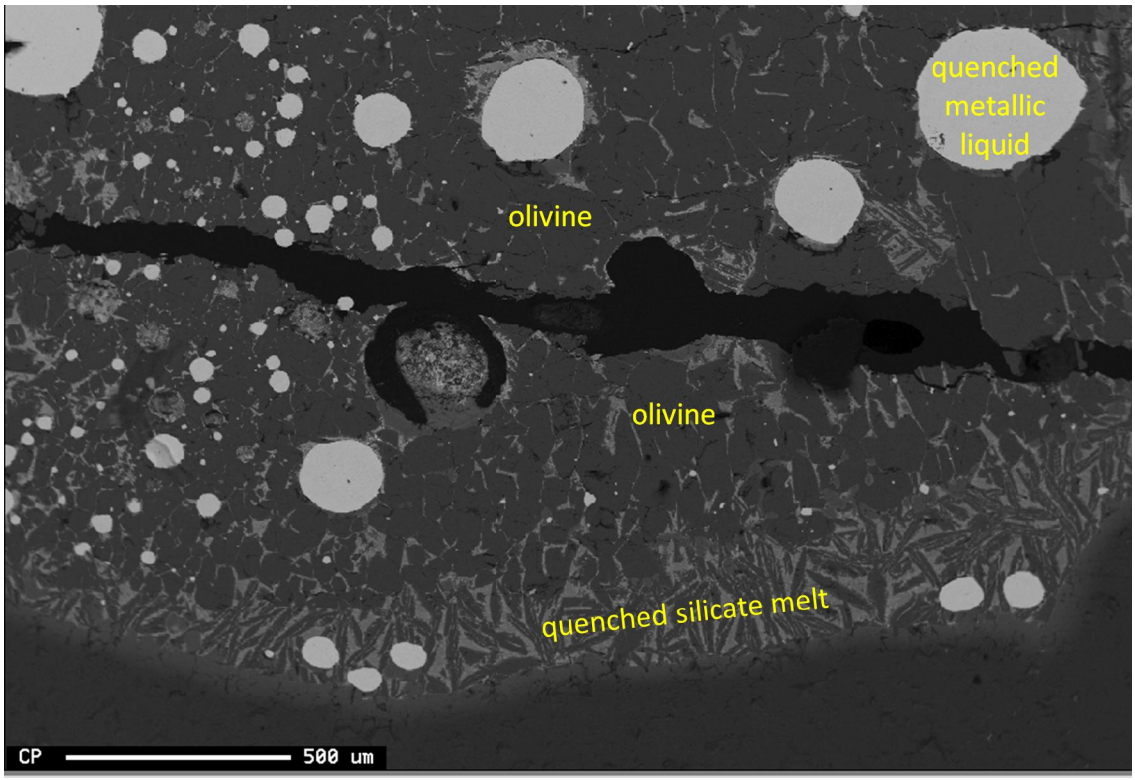

Figure 18. Backscattered electron image of PC sample GPC2.

Their compositions are homogeneous, within the individual experiments, and differ only between experiments in their Fe and W abundances. Metals showed exsolution of low-W and high-W phases, and inclusion of oxide grains, which appear as dark specks on BSE images. The oxide grains are quench products and have been observed by others in metal/silicate experiments (O'Neill et al., 1998; Chabot and Agee, 2003; Mann et al., 2009). The quenched silicate liquid consists of feathery olivine grains with finer-grained interstitial crystalline assemblages. This is a quench texture and the average composition of the entire assemblage of feathery olivine and interstial crystalline materials were taken to represent the composition of the silicate melt. The ferropericlase grains were present near capsule walls and mostly along metal blebs, and

were typically an equilibrium phase coexisting with the silicate melt. The euhedral olivines were likewise an equilibrium phase and range in size from tens of microns up to approximately 200 microns. Saturation in MgO due to capsule composition and the added FeO in the starting mixture promoted the abundant growth of the euhedral olivines which comprised a significant portion of the sample chamber volumes (>80%), and likewise promoted growth of Fp.

Due to the large grain sizes and large sample volume, a broad beam approach was taken to characterize the compositions of the silicate melts. A 30 micron beam diameter was used on the microprobe, with large numbers of analytical points collected along transects, gave sufficient data density to measure the average silicate melt compositions. Averaged silicate melt compositions across these three samples are similar with the primary difference being the tungsten oxide abundances and relative differences in other oxide abundances.

All samples have similar silicate compositions except for FeO and MgO abundances, which vary by approximately five weight percent across the experiments. The Fe and W abundances vary linearly with the abundances of W in the starting materials. The range of fO_2 in the experiments is 0.2 log units relative to the IW buffer with values of -1.50 to -1.70. The range in molar metal/silicate partition coefficients is approximately 0.45 log units, where the partition coefficients increase positively with higher W abundance in the starting materials (Table 6). To remove the effect of fO_2 on the results, the partition coefficients were corrected to a common fO_2 which reduced the range in molar partition coefficient to 0.16 log units. With this fO_2 correction, the molar partition coefficients vary within the 2-sigma uncertainties, where the uncertainties are

the standard error of the mean (Figure 19). This indicates that experiments with doping levels of W up to 5 wt% in the starting materials obey Henry's Law. All experiments in this study use no more than this level of W. Walter and Thibault (1995) observed Henry's Law behavior in metal/silicate partitioning experiments with W levels of 10 wt% of the bulk starting composition.

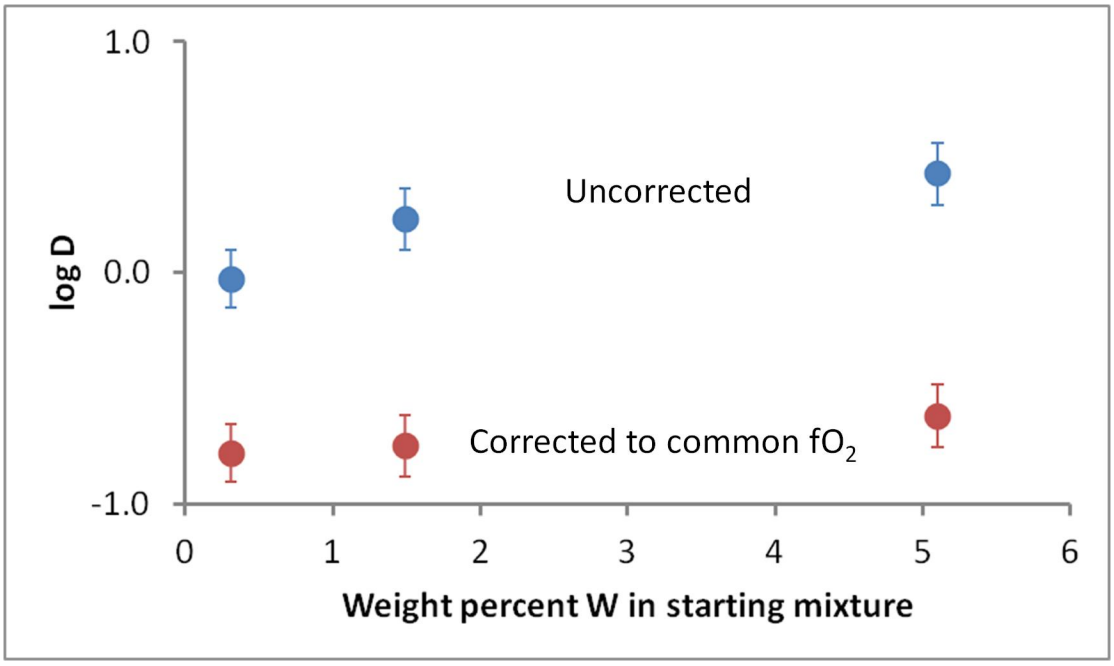

Figure 19. Evaluation of Henry's Law behavior in W metal/silicate experiments with weight percent level W doping in starting materials. Blue symbols are uncorrected molar metal/silicate partition coefficients, and red symbols are molar metal/silicate partition coefficients corrected to common fO_2. Error bars are 2-sigma, where sigma was calculated from the standard errors of the means of measurements made on silicate and metallic melts.

3.1.3.2 Samples GPC6-GPC7

These two samples were the basis for the reversal experiments to assess equilibrium in the experimental design. Phase assemblages consisted of quench silicate liquid, quench metallic liquid, and olivine. Unlike the MgO capsule experiments, the euhedral olivines in these two experiments represented a much lesser portion of the sample volumes (<20%). The quenched silicate was essentially the same texture as in

GPC2-GPC4 (Figure 20). The average composition of the silicate melt (Table 4) was similar to the starting peridotite composition (Table 2) due to the lack of reaction between silicate and the graphite capsules. Metal compositions were uniform for multiple metal blebs within individual samples, with standard error of the mean on Fe measurements of approximately 0.3 wt%. The compositions between the two samples were similar, though Fe abundances differed approximately 4 wt% and W abundances differed by approximately 2 wt% (Table 5). Metals showed exsolution similar to most other experiments in this study. Both samples also contained oxide grains in the metals, with GPC6 having a greater portion of these grains, which was detected in chemical analyses by slightly higher oxygen than in GPC7. The metals were saturated in carbon by reaction with the graphite capsules and this was shown by low probe totals, with the difference from 100% taken as the C abundances.

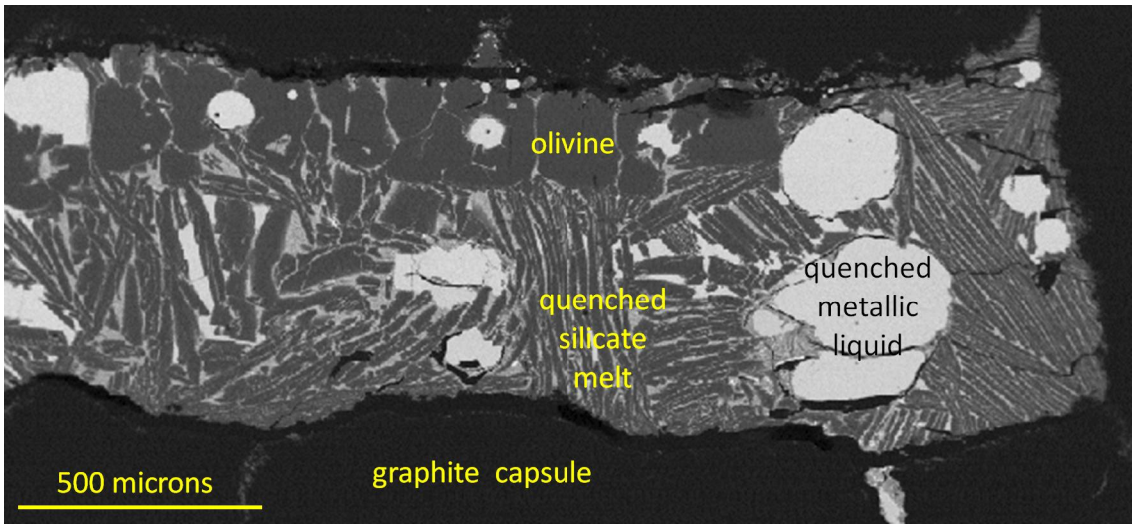

Figure 20. Backscattered electron image of PC sample GPC7. This sample was one of two experiments to assess equilibrium in the metal/silicate partitioning experiments through reversal of the reaction, i.e. starting materials alternately contained W metal and WO_2.

The fO_2 in these experiments were similar with -1.56 and -1.67 for GPC6 and GPC7, respectively. Tungsten molar metal/silicate partition coefficients differed by

approximately 0.3 log units between the two experiments (Figure 21). The partition coefficient for sample GPC6 (WO_2 in starting materials) was larger than for GPC7 (W in starting materials). If the difference in the W partition coefficients was due to an incomplete reduction of WO_2 to W , i.e. non-equilibrium, then it would be expected that GPC6 would have a lower metal/silicate partition coefficient, particularly since the fO_2 was slightly higher, which would tend to reduce the partition coefficient. Partition coefficients for Ni and Cr were also calculated and they showed a similar trend to W (Figure 21), with the GPC6 coefficients greater than the GPC7 coefficients. The source of the Ni and Cr in the starting materials was the peridotite, no Ni or Cr were added as metals. The similar trend in W, Ni, and Cr partitioning suggests a systematic difference in these experiments, but it is not evident what that difference was, given the same pressure and temperature conditions for both experiments.

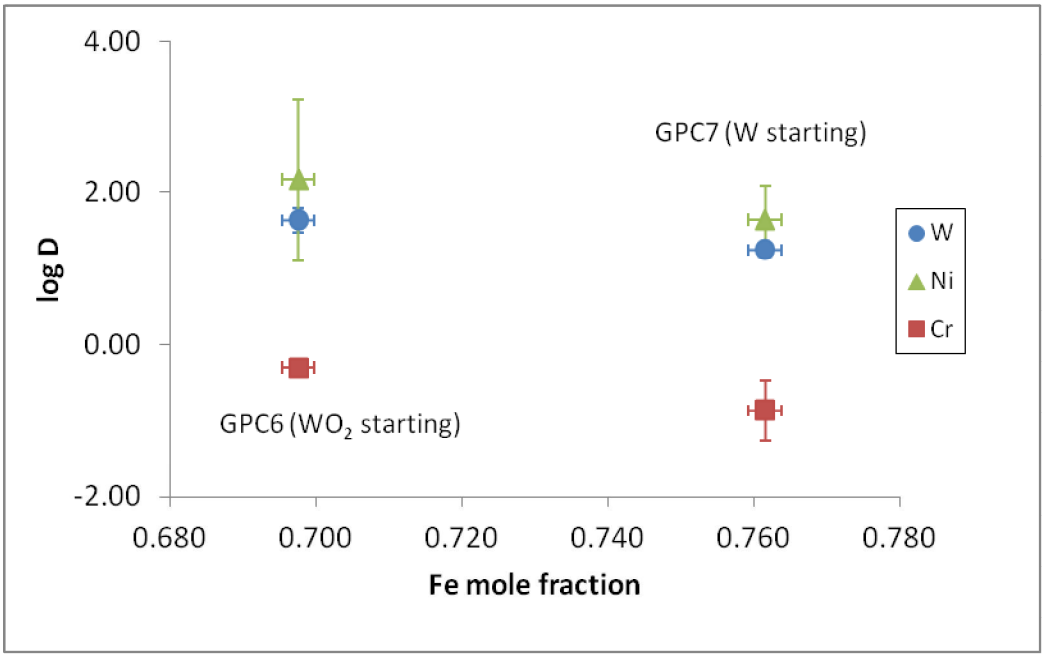

Figure 21. Molar metal/silicate partition coefficients calculated from experiments to assess completion of metal–silicate reaction using both WO_2 and W metal in starting materials.

3.2 Partition Coefficients

Tungsten metal/silicate molar partition coefficients were calculated for each experiment. The log values of the molar partition coefficients are plotted versus pressure in Figure 22. At first glance, this plot suggests a distinct negative trend in log D with increasing pressure, but the trend is not entirely due to pressure. Temperature, silicate and metal compositions, and fO_2 effects also contribute (Figure 22). Note the two highest pressure MAP experiments, which have distinctly different silicate compositions and the lowest fO_2, show larger log D values, suggesting more siderophile character. In the other MAP experiments, differences can be seen between the graphite and MgO capsule runs. In the case of the two LHDAC experiments, given the similarities in temperature, silicate and metal metal compositions, and fO_2 between the these experiments, the difference in log D shown is significantly influenced by pressure.

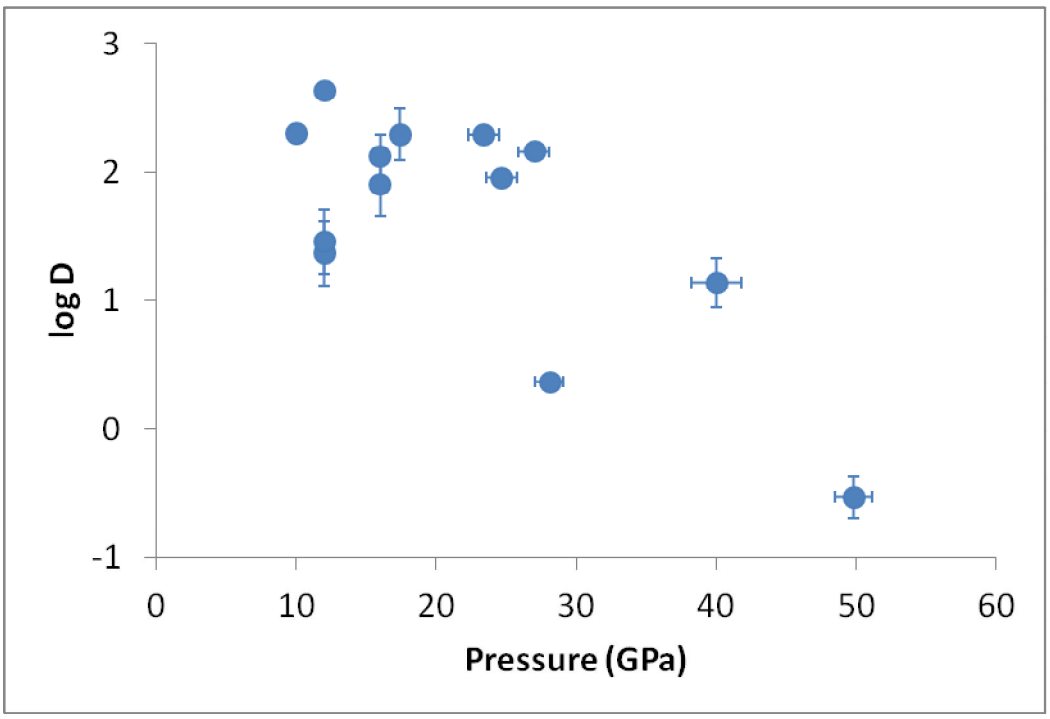

Figure 22. Plot of W metal/silicate molar partition coefficients from experiments in this study, with no corrections for T, fO_2, or melt compositions applied.

As a first approximation, I applied some simple corrections to the partition coefficients to examine the pressure effect. A more rigorous evaluation of the combined effects of pressure, temperature, composition, and fO_2 is presented in Section 3.5 below. The partition coefficients were corrected to the fO_2 of the lowest temperature experiment using the equation $logD^{met/sil}_{corr.} = logD^{met/sil}_{\Delta IW} + \frac{y}{2}\Delta IW_{exp.} - \Delta IW_{ref.}$ where ΔIW_{ref} is the fO_2 to which partition coefficients are to be corrected and *y* is valence of the W in the silicate. A temperature correction was applied using the equation $logD^{m/s}_{Tcorr.} = logD^{m/s}_{Texp.} - \left(-4920 * \Delta\frac{1}{T}\right)$where $\Delta 1/T$ is the difference in inverse temperature between the lowest temperature experiment and the experiment being corrected. The correction factor was determined by a linear fit of isobaric data (experiments 1, 3, 8, 20 and 28) from Righter et al. (2010) as $logD^{met/sil}_{W} =$

$-4920\left(\frac{1}{T}\right) + 3.84$. The remaining influences on the partition coefficients are then pressure and composition. In Figure 23, the fO_2 and temperature corrected partition coefficients are plotted as a function of pressure with the symbols sizes representing the SiO_2, MgO, and CaO mole fractions, whose abundances are thought to influence W solubility in silicate melts. Qualitatively, these plots don't suggest a strong influence of composition, which is not in agreement with most previous findings (Walter and Thibault, 1995; O'Neill and Eggins, 2002; O'Neill et al., 2008; Cottrell et al., 2009). This could indicate that the temperature relationship determined from the 1 GPa data of Righter et al. (2010) are not applicable across the wide pressure range of the present data set. The individual contributions of pressure, silicate composition and metal composition cannot be readily separated and will be examined in later sections using regression approaches.

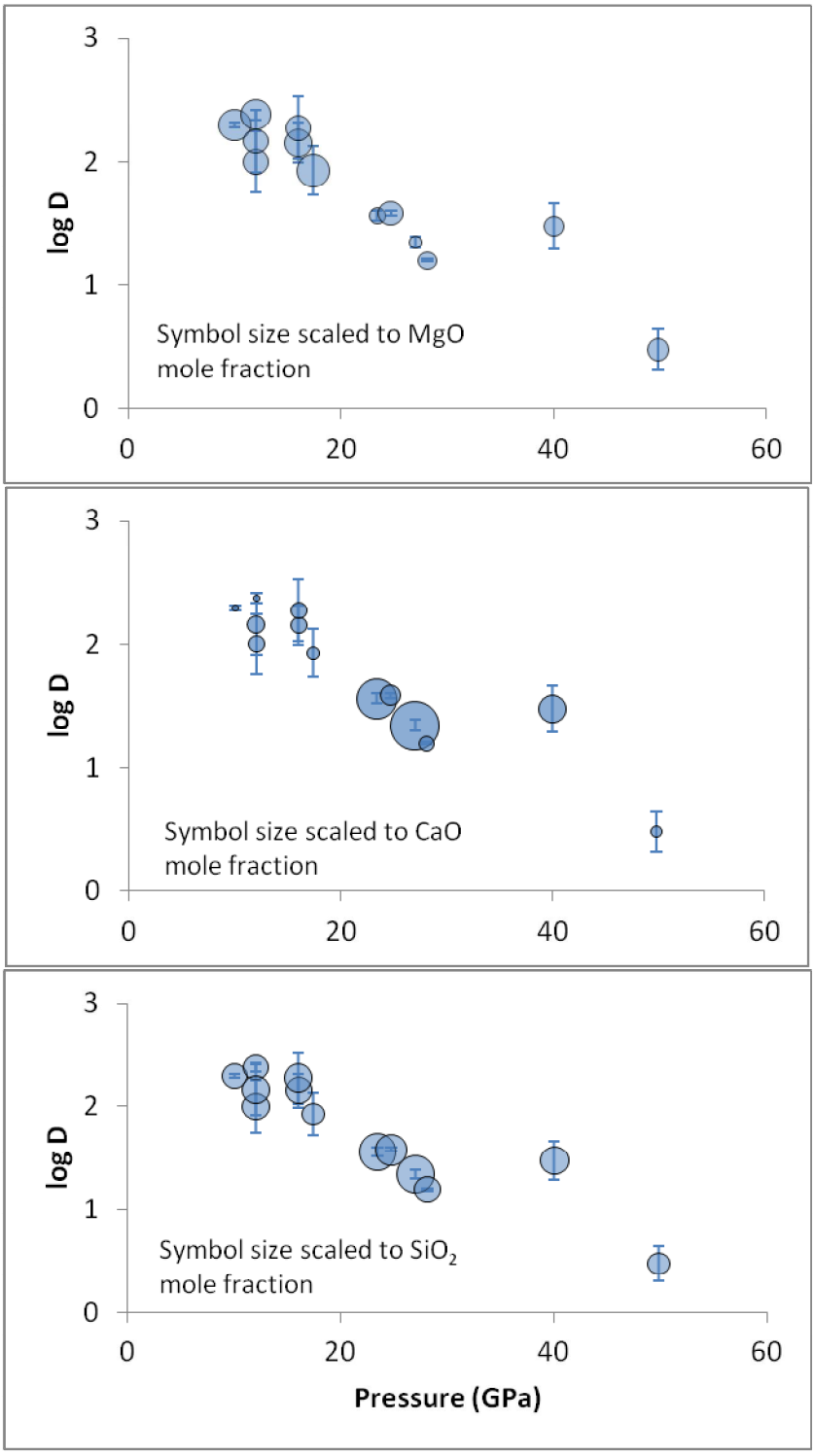

Figure 23. Tungsten metal/silicate molar partition coefficients for this study, with temperature and fO_2 corrections applied as discussed in the text. Error bars are 1-sigma uncertainties propagated from microprobe counting statistics on individual measurements.

3.3 Tungsten Valence in Silicate Melts

Tungsten exhibits a 6+ valence in silicate melts at geologically relevant redox conditions (O'Neill et al., 2008). Determination of W valence at high pressures and temperatures is crucial for studies of W metal/silicate partitioning because it is integral to the underlying metal-oxide equilibrium as shown in equation (2). Debate continues on this matter, but some consensus exists that at geologically relevant redox conditions, W is in a mixed valence state in silicate melts at pressures lower than 6 GPa, and predominantly, if not exclusively, 4+ at higher pressures (Cottrell et al. 2009; Righter 2011; Siebert et al. 2011).

3.3.1 Estimating Tungsten Valence

Given the metal-oxide equilibrium $W + x/4\,O_2 \rightleftharpoons WO_{x/2}$, the equilibrium constant $K = a\left(WO_{x/2}\right)/a(W)f(O_2)^{x/4} = X\gamma\left(WO_{x/2}\right)/X\gamma(W)f(O_2)^{x/4}$. Rearranging in terms of the log of the molar partition coefficient and the log of oxygen fugacity gives $logD_W^{met/sil} = -\frac{x}{4}logf(O_2) + C$, where *C* contains the activity coefficients and the equilibrium constant. Fitting *log D* versus *log* fO_2 at fixed temperature, pressure, and composition, the slope is equal to *x/4* where *x* = valence of W in the silicate.

Using the database of tungsten metal/silicate data determined in this study, with data at pressures ranging from 10 to 50 GPa, log D was fitted versus log fO_2, estimated as ΔIW (Figure 24). No corrections for the effects of pressure, temperature or melt compositions were made to the partition coefficients or fO_2 estimates. Therefore, it is assumed that these combined effects are similar for both the partition coefficients and

the estimated fO_2 values, and that the net effect on the uncertainty of the determined valence is minor. The slope of this fit is 0.98, so by using the relationship described above, x = 4 * 0.98 = 3.92. With the assumptions made and within the uncertainty of the fit, a valence of 4+ is indicated.

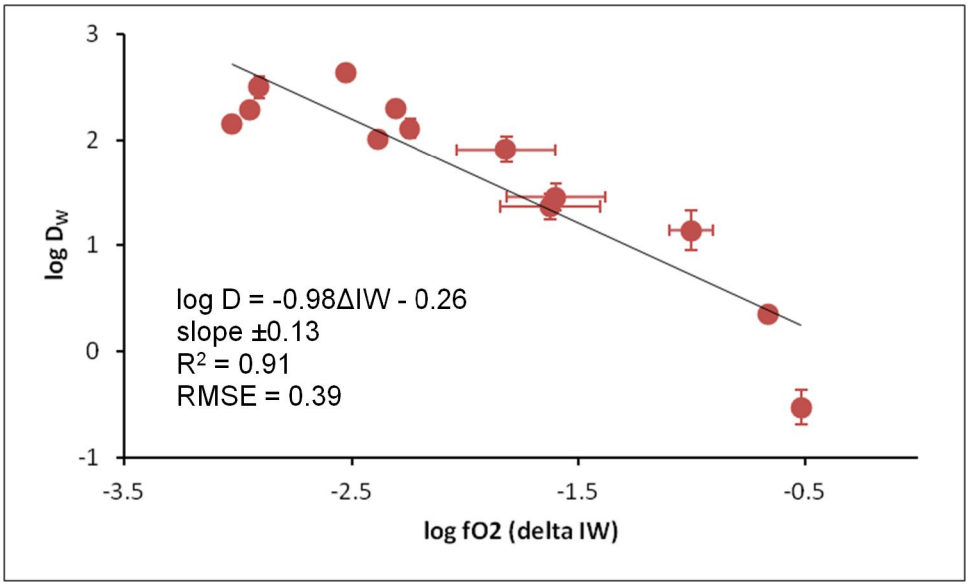

Figure 24. Tungsten metal/silicate molar partition coefficients for this study fitted against log fO_2, with no corrections for temperature, pressure, or silicate or metallic melt composition applied.

To better constrain the valence of W in silicate melts, I used the metal/silicate partitioning data of Cottrell et al. (2009) which consists of isobaric and isothermal sets. Taking each of the isobaric-isothermal data sets from Cottrell et al. (2009), the partition coefficients were corrected to a common silicate composition of nbo/t = 2.8, leaving fO_2 as the only variable. I fitted log D against log fO_2 (as ΔIW) to determine W valence at pressures of 0.5, 1, 2, 6, 11 and 18 GPa. The results of these fits indicate that the valence of tungsten is mostly 6+ at 0.5 GPa, has a mixed valence of 4+ and 6+ at 1 and 2 GPa, becoming predominantly 4+ at 6 GPa and higher. These estimates of tungsten valence are consistent with those of Cottrell et al. (2009), which were based on regression coefficients of fits to the same data.

3.3.2 Measurements of Tungsten Valence

Ertel et al. (1996) conducted W solubility studies using an anorthite-diopside eutectic silicate composition, and determined tungsten to have a 4+ valence across the range of fO_2 investigated, which was approximately IW to IW-5. O'Neill et al. (2008) conducted studies with a wider range of silicate compositions in the CMAS system, including the same An-Di compositions used by Ertel et al. (1996). In contrast to Ertel et al. (1996), O'Neill et al. (2008) determined a predominantly 6+ valence for tungsten with possibly some 4+ in the lowest fO_2 range of their experiments at approximately IW-3. Danielson et al. (2008) conducted XANES studies on samples in CMAS and natural basaltic compositions with tungsten doping. The results of Danielson et al. (2008) indicate that tungsten valence is 6+ above the IW buffer becoming mixed valence below IW, and that W valence may be predominantly 4+ at fO_2 less than IW-2 for Fe-free compositions and less than IW-3 for Fe-bearing compositions. Considering the results of these three studies, it appears that the valence of W in silicate melts at 1-bar pressure is likely 6+ at fO_2 near the IW buffer, and progressively tends toward a 4+ valence at lower fO_2 conditions of IW-2 and lower. Because these results were obtained at 1-bar pressure, they lack constraint on W valence at the high pressure and temperature conditions relevant to core formation in a deep magma ocean. Also, these studies employed mostly Fe-free compositions, with the exception of some experiments in Danielson et al. (2008), and consisted of equilibrium between silicate melt and W metal, in contrast to the Fe-rich metal of the Earth's core.

3.4 Activities in Silicate and Metallic Melts

A very common approach in studies of metal/silicate partitioning is the assumption of ideality of relevant components in solutions, i.e. that activity coefficients are unity, or ratios of activity coefficients are either unity or constant with pressure or temperature. Under conditions where a solute is sufficiently dilute and within Henry's Law, or the solvent is sufficiently abundant and within Raoult's Law, then these assumptions are valid at least in terms of first order effects. However, if the solute concentration falls outside Henry's Law limits then solute-solvent interactions likely will violate assumptions of ideality. Additionally, strong solute-solute interactions can also invalidate an assumption of ideality of a component in solution, even if that solute is dilute.

Examples related to metal/silicate partitioning include calculation of molar partition coefficients, exchange coefficients, and estimates of fO_2 relative to the IW buffer (ΔIW). An underlying assumption in calculating partition coefficients and exchange coefficients is ideality of mixing or constant activity coefficients, or their constant ratios with pressure and temperature. The definition of ΔIW includes the ratio of the activities of FeO and Fe. Assumptions of ideality, if not valid, will result in calculated values that are not strictly correct and may include significant error, thus not accurately representing the actual conditions of the system being described.

A silicate melt contains a mixture of oxide components that are not, strictly speaking, ideally mixed. Therefore, the activity coefficients of the oxide components are not unity. Activity coefficients for some oxides have been determined, but for many trace elements have not. O'Neill and Eggins (2002) determined activity coefficients for

FeO, NiO, CoO, and MoO_x in the CMAS system. They found a range of activity coefficient values for FeO with an average value of $\gamma_{FeO} = 1.5$. Knowledge of the activity coefficient for a trace element can be important in metal/silicate partitioning, especially in cases where the activity is correlated to the abundance of a particular major element component. For example, the activity coefficient of MoO_x was found to be strongly correlated with CaO abundance, due to formation of complexes such as $CaMoO_x$ in silicate melts (O'Neill and Eggins, 2002). Given its similar chemical characteristics to Mo, W activity may show similar sensitivity for CaO in silicate melts. O'Neill et al. (2008) showed that the activity coefficients of Mo and W oxides are strongly correlated, and suggested that W solubility in silicate melts is enhanced by higher CaO abundance in a manner similar to that of Mo. They also stated that the CaO abundance should exhibit a stronger influence on Mo and W solubilities in silicate melts, as compared to MgO abundance, based on the lower Gibbs free energy of formation for Ca versus Mg molybdates and tungstates; i.e. the Ca complexes are thermodynamically more stable.

3.4.1 Carbon in Fe Metal Alloys

Solute-solute interactions in solutions can reduce the activities of the solutes. Reduced activity of a solute means that it has a lower tendency to leave the solution and is therefore more strongly bound in the solution. The presence of carbon in Fe metal alloys in particular is known reduce the activity of Fe and the alloying components. In the case of the ternary Fe-W-C system, the interaction of carbon and tungsten increases the siderophility of W. Because of the extent of activity reduction, calculated metal/silicate partition coefficients with assumed unity activity coefficients will

overpredict the siderophility, i.e. the molar concentration ceases to be a strictly valid proxy for activity. It has been shown that correction for carbon activity results in lower calculated partition coefficients and increased estimates of fO_2 in the ΔIW form (Wade and Wood, 2005; Cottrell et al., 2009, 2010).

3.4.2 Modeling Approaches

One approach to addressing the effect of carbon on activities in Fe-metal alloys is to apply an activity model to the experimental data. This approach was presented by Wade and Wood (2005) and has been used by others (Corgne et al. 2008, Cottrell et al. 2009, and Siebert et al. 2011). It is based on use of interaction parameters in a multicomponent solution model that was developed for use in the steelmaking industry (The Japan Society for the Promotion of Science and The Nineteenth Committee on Steelmaking, 1988). The activity coefficients can be calculated that account for the interactions of the solution components. The major drawback is that the data on which the model was developed were collected at temperatures that were much lower than those applicable to the deep Earth. This requires extrapolation of the interaction parameters to the higher temperatures of high pressure metal/silicate experiments. Additionally, the pressure dependence on the model is unknown because all data were at ambient pressure. Righter (2011) also questioned the applicability of the approach to geologic systems because the data were collected only on metallic liquids (melts for steelmaking) that did not coexist with silicate liquids.

Another approach is to account for the effects of carbon by including a term in a multi-parameter regression of partition coefficients (see Regression section below). This approach was presented by Righter et al. (1997), and has the merit of not

extrapolating lower temperature data, i.e. interaction parameters. It has the potential to better characterize the high temperature and pressure effects of carbon because it based directly on the data at experimental temperatures and pressures. It is perhaps not as thermodynamically robust as the other approach, but does relate to the physical process by using the mole fraction of carbon in a parametric form similiar to a simple binary solution activity model, e.g. $a\ ln(1 - X_C)$, where a can be considered as a Margules parameter. Comparing the two approaches for the cases of Ni and Co, Righter (2011) showed similar solutions for matching the partition coefficients required by core/mantle abundances. This suggests the two approaches are equivalent in predicting metal/silicate partitioning, at least for elements with single valences such as Ni and Co.

3.5 Data Analysis

3.5.1 Activity Correction in Metals

As one line of analysis of my data, I corrected the calculated partition coefficients using the multi-component model of Ma (2001), as described below. For ternary systems the activity coefficients of the solvent γ_1 and solutes γ_i can be calculated from equations 25 and 26 of Ma:

$$\ln \gamma_1 = \varepsilon_2^2\left[X_2 + \ln(1-X_2)\right] + \varepsilon_3^3\left[X_3 + \ln(1-X_3)\right] + \varepsilon_2^3 X_2 X_3\left[1 - \left(\frac{1}{(1-X_2)}\right) - \left(\frac{1}{(1-X_3)}\right)\right]$$
$$-\left(\frac{\varepsilon_2^3}{2}\right) X_2^2 X_3^2\left[\left(\frac{3}{(1-X_2)}\right) + \left(\frac{3}{(1-X_3)}\right) + \left(\frac{X_2}{(1-X_2)^2}\right) + \left(\frac{X_3}{(1-X_3)^2}\right) - 3\right]$$

$$\ln\gamma_i = \ln\gamma_1 + \ln\gamma_i^0 - \varepsilon_i^i \ln(1-X_i) - \varepsilon_i^k X_k\left[1+\left(\frac{\ln(1-X_k)}{X_k}\right)-\left(\frac{1}{(1-X_i)}\right)\right]$$
$$+\varepsilon_i^k X_k^2 X_i\left[\left(\frac{1}{(1-X_i)}\right)+\left(\frac{1}{(1-X_k)}\right)+\left(\frac{X_i}{2(1-X_i)^2}\right)-1\right]$$

Applying this correction to the ternary Fe-W-C system, setting W as phase 2 and C as phase 3, the interaction parameters ε and ideal activity coefficent γ_i^0 were taken from published tabulated values; $\varepsilon_W^C = \varepsilon_C^W$ =-3.05, ε_C^C = 12.81, ε_W^W = not available and therefore assumed = 0, γ_C^0 = -0.62 (Siebert et al. 2011). These values were established at a reference temperature of T_0 = 1873 K. Extrapolation of ε and γ to temperatures above the reference temperature, i.e. temperatures of partitioning experiments, are given by: $\ln\gamma_i^0(T) = T_0/T \ln\gamma_i^0(T_0)$ and $\varepsilon_i^k(T) = T_0/T\ \varepsilon_i^k(T_0)$.

$$\ln\gamma_{Fe} = \varepsilon_C^C\left[X_C + \ln(1-X_C)\right] + \varepsilon_W^C X_W X_C\left[1-\left(\frac{1}{(1-X_W)}\right)-\left(\frac{1}{(1-X_C)}\right)\right]$$
$$-\left(\frac{\varepsilon_W^C}{2}\right)X_W^2 X_C^2\left[\left(\frac{3}{(1-X_W)}\right)+\left(\frac{3}{(1-X_C)}\right)+\left(\frac{X_W}{(1-X_W)^2}\right)+\left(\frac{X_C}{(1-X_C)^2}\right)-3\right]$$

$$\ln\gamma_W = \ln\gamma_{Fe} - \varepsilon_W^C X_C\left[1+\left(\frac{\ln(1-X_C)}{X_C}\right)-\left(\frac{1}{(1-X_W)}\right)\right]$$
$$+\varepsilon_W^C X_C^2 X_W\left[\left(\frac{1}{(1-X_W)}\right)+\left(\frac{1}{(1-X_C)}\right)+\left(\frac{X_W}{2(1-X_W)^2}\right)-1\right]$$

$$\ln\gamma_C = \ln\gamma_{Fe} + \ln\gamma_C^0 - \varepsilon_C^C \ln(1-X_C) - \varepsilon_C^W X_W\left[1+\left(\frac{\ln(1-X_W)}{X_W}\right)-\left(\frac{1}{(1-X_C)}\right)\right]$$
$$+\varepsilon_C^W X_W^2 X_C\left[\left(\frac{1}{(1-X_C)}\right)+\left(\frac{1}{(1-X_W)}\right)+\left(\frac{X_C}{2(1-X_C)^2}\right)-1\right]$$

Applying this correction to the present experimental data and to literature data with carbon-bearing metals, the net result in calculated partition coefficients and in fO_2 estimates relative to the IW buffer is roughly 0.2 log units, when compared to those

same parameters calculated using mole fractions and assuming unity activity coefficients. The actual variation is approximately proportional to the mole fraction of carbon in a given experiment and is shown in Figure 25, which shows the difference in calculated metal/silicate molar partition coefficients and the ΔIW values. The relationship is stronger for the ΔIW than for the log D values, but a relationship clearly exists even in the log D case. Note that for all activity-corrected calculations, an activity coefficient value of 1.5 was used for FeO, and the activity coefficient for WO_x was assumed to be one.

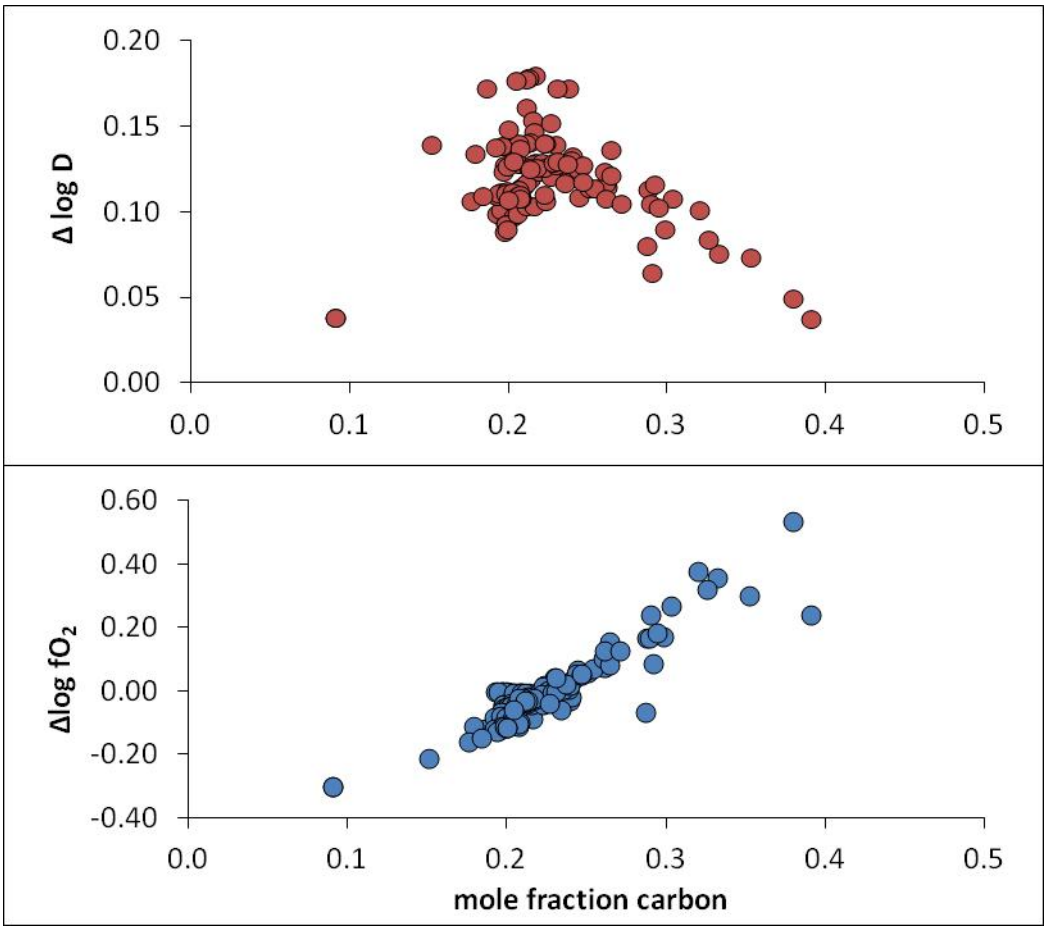

Figure 25. Difference plots for experiments with carbon-bearing metals. The values ΔlogD and ΔlogfO_2 are the differences between uncorrected partition coefficients and those calculated using activity-corrected metals. Carbon contents in metallic phases were estimated based on deficit of microprobe totals from 100 percent. The outlier in the ΔlogD plot is LHDAC sample G38a, where the high temperature, approximately 4400 K, resulted in only a small activity correction.

3.5.2 Regressions

As discussed previously regarding both literature data and the results of the present study, the combined effects of pressure, temperature, silicate and metal compositions, and fO_2 are often difficult to experimentally isolate. One approach to this problem is to parameterize partitioning data sets to characterize these combined effects using an expression of the general form $\log D^{met/sil} = a + b(fO_2) + c(1/T) + d(P/T) + e(X)$, where X represents a measure of silicate melt composition. A similar regression form can be used in modeling metal/silicate partitioning using the Fe-W exchange coefficient rather than the partition coefficient with an explicit fO_2 term (Wade and Wood 2005; Wood 2008; Cottrell et al. 2009; Siebert et al. 2011; and Righter 2011).

Considering the discussion in Section 3.3 concerning the valence of W at low pressures, regressions of W metal/silicate partitioning data at pressures less than approximately 5 GPa may be subject to confounding effects of a probable mixed valence state of W in the silicate (Cottrell et al., 2009). Additionally, Sanloup et al. (2011) have described a density change in Fe-rich metallic melts at approximately 5 GPa that may contribute to changes in measured metal/silicate partition coefficients. Based on these arguments, I do not include data below 5 GPa in regressions of metal/silicate partitioning data or in fitting of the excess Gibbs energy of mixing in the WWO-IW buffer parameterization approach presented in Chapter 4.

The solubility of W in silicate melts has a compositional dependence and, thus, a measure of silicate composition is needed in regressions of W metal/silicate partitioning data. One measure of silicate melt composition is the ratio of nonbridging oxygens to tetrahedrally-coordinated cations, termed nbo/t, which characterizes the degree of melt

polymerization, or in simplest terms, the extent of interconnection of the silicate tetrahedra (Mysen, 1983). This ratio can be calculated as $\frac{nbo}{t} = \left(2\left(X_{Fe} + X_{Mg} + X_{Ca}\right) - 2X_{Al}\right)/(X_{Si} + 2X_{Al})$ where the X terms are the mole fractions of the indicated cations. The nbo/t proxy for silicate composition has been used extensively in literature and still enjoys widespread use. However, it has been demonstrated that the solubility of high valence elements such as W are affected to different extents by the network-modifying cations Ca and Mg, which are not distinguished by the nbo/t formulation. The work of O'Neill and Eggins (2002), O'Neill et al. (2008), and Righter (2011) show that the effect on W metal/silicate partitioning is more sensitive to the abundance of Ca than to that of Mg. Additionally, Si and Al are increasingly in octahedral coordination at high pressures and not in tetrahedral coordination (Williams and Jeanloz, 1998). Therefore, the concept of nbo/t loses much of its meaning at high pressure. To address these issues, Righter (2011) used the mole fractions of the major oxides in the silicate melt to characterize silicate composition in metal/silicate partitioning regressions. Following Righter, I adopt the parameterization scheme that is based on the mole fractions of oxide components in the silicate melt versus using nbo/t .

One further issue is the presence of C and S in metallic melts and their effects on W solubility. Carbon is known to readily form both Fe and W carbides that result in a stronger affinity of W for the metal phase, and consequently results in higher calculated partition coefficients when ideality of mixing is assumed with activity coefficients equal to one (Siebert et al. 2011). Sulfur exhibits the opposite behavior and acts to exclude W from the metal phase, and therefore results in a less siderophile behavior of W in the presence of S-bearing metals (Jana and Walker 1997; Ohtani et al. 1997).

Many experiments are carbon-saturated due to either graphite capsules or contamination by carbon from diamond anvils, and some experiments were intentionally sulfur-bearing. The two approaches presented in the literature are described in Section 3.4.2. I have explored both approaches in my regressions and a comparison of the results is given below.

Taking the molar partition coefficients for my data combined with partition coefficients calculated from literature data (Walter and Thibault, 1995; Hillgren et al., 1996; Ohtani et al., 1997; Righter and Shearer, 2003; Cottrell et al., 2009), I parameterized the metal/silicate partitioning of W. This is regression R1 and the fitted parameters and their uncertainties are listed in Table 7. The silicate compositional

Table 7. Regression coefficients for parameterizations of W metal/silicate partitioning.

	Regression	R1		R2		R3	
	Partition coefficient form	log D molar		log D molar (with metal activity correction)		log $K_D^{Fe\text{-}W}$	
	Fit uncertainty (r.m.s)	0.20		0.35		0.20	
Parameters	*a*	-0.79	±0.39	-0.20	±0.69	-0.93	±0.44
	b (ΔIW)	-0.82	±0.11	-1.02	±0.18	-	
	c (1/T)	-1926	±854	-3140	±1570	-2174	±907
	d (P/T)	-118	±15	-142	±27	-122	±16
	e (SiO_2)	7.84	±0.68	5.70	±1.14	7.39	±0.69
	f (Al_2O_3)	4.81	±1.36	6.46	±2.31	5.06	±1.11
	g (CaO)	-8.82	±1.3	-3.54	±2.15	-9.00	±1.35
	h (C)	-1.01	±0.43	-		-0.44	±0.32
	i (S)	-6.39	±0.83	-4.83	±1.46	-5.79	±0.71

parameters are the mole fractions of SiO_2, Al_2O_3, and CaO. A fit that included the mole fraction of MgO resulted in an uncertainty on the MgO parameter that was greater than the parameter value, indicating that the fit was insensitive to the MgO abundance,

therefore MgO was not included in R1. The metal compositional parameters are the mole fractions of C and S. Using R1, W metal/silicate molar partition coefficients were calculated along the peridotite liquidus to a maximum pressure of 100 GPa (Figure 26). The liquidus used in Figure 26 is a 2nd order fit to the data of Herzberg and Zhang (1996). The silicate composition was set as peridotitic with mole fractions SiO_2 = 0.38, Al_2O_3 = 0.02, and CaO = 0.03. The metal compositional values were mole fractions of C = 0.008 and S = 0.03 based on the estimated Earth core composition of McDonough (2003). Figure 26 shows a decreasing trend in the siderophility of W with increasing pressure along the peridotite liquidus.

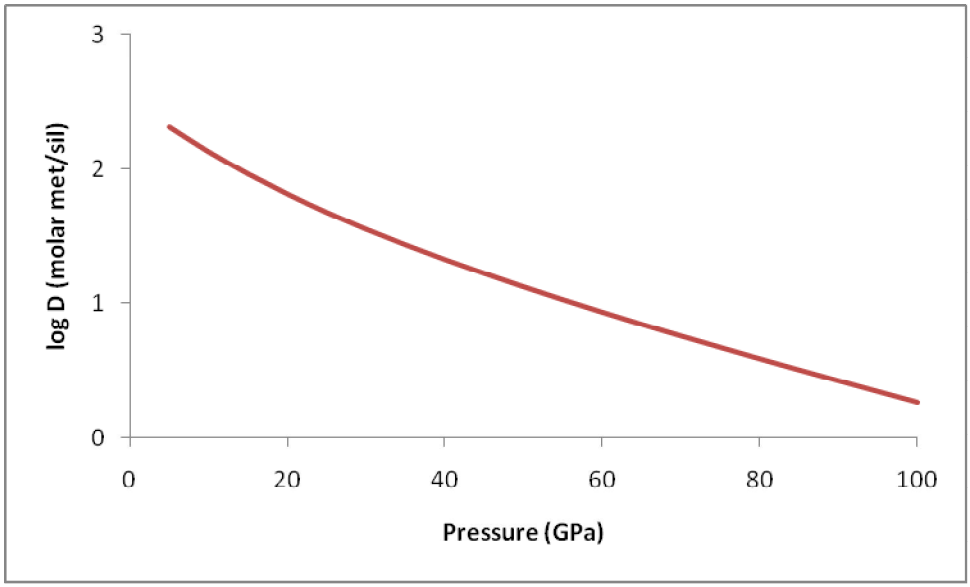

Figure 26. Regression R1 plotted on the peridotite liquidus. The liquidus was based on experimental data of Herzberg and Zhang (1996) and Zerr et al. (1998).

With the same parameter values, log D values were calculated along isotherms and isobars (Figure 27). The plots in Figure 27 indicate a negative pressure effect and positive temperature effect on W metal/silicate partitioning, which is agreement with other studies (Cottrell et al., 2009; Righter, 2011). In fact the pressure effect given by Cottrell et al. (2009) along a 2500 K isotherm is approximately the same as that shown

in Figure 27. Across a temperature range of 2000 K, the pressure effect decreases with increasing temperature from approximately three log units to two log units. The temperature effect increases with increasing pressure from less than one log unit to just over two log units.

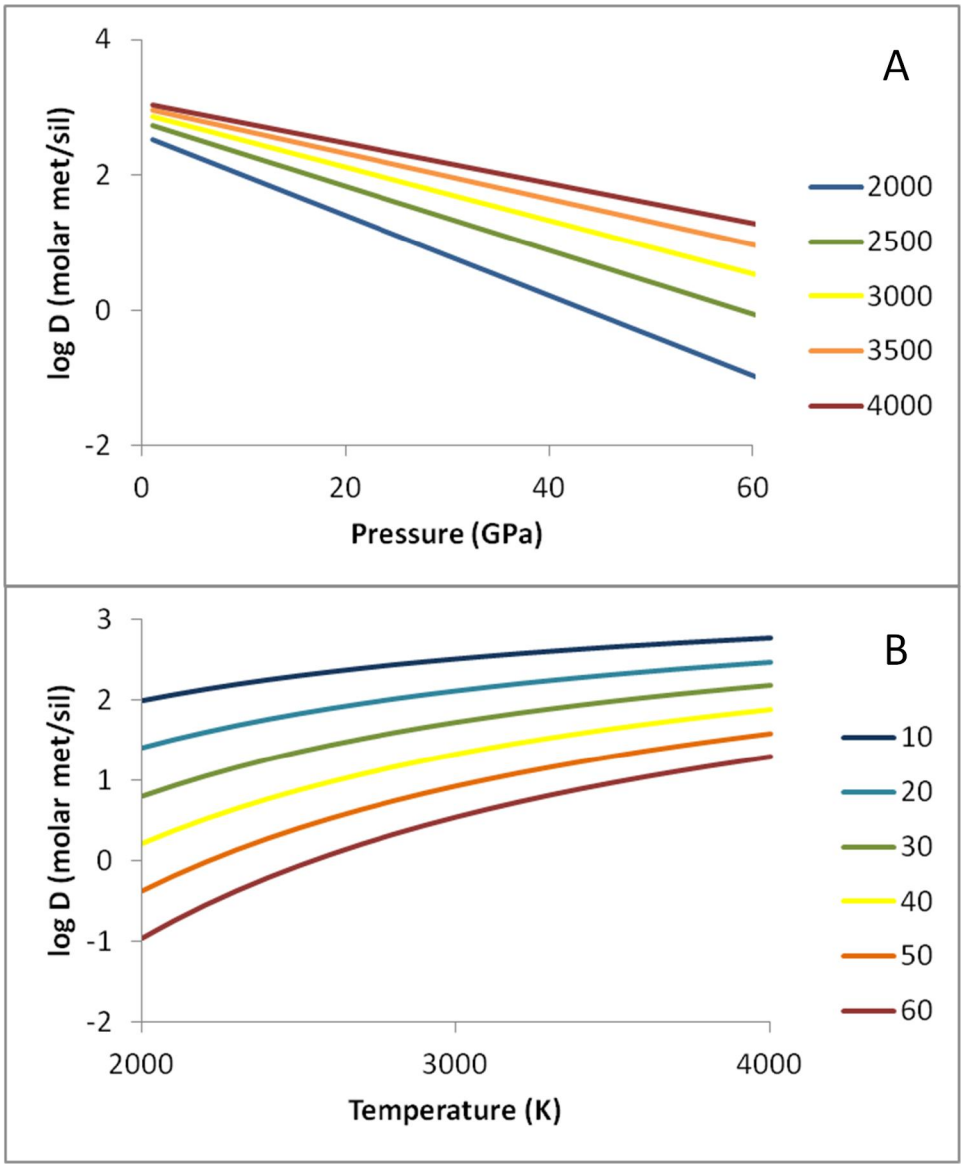

Figure 27. Regression R1 along isotherms and isobars. Isotherms in plot (A) are in Kelvins, and isobars in plot (B) are in GPa.

To compare the two approaches for dealing with C in the metallic melts, I regressed the data for the same experiments after applying the multicomponent activity

model described in Section 3.5.1 to the carbon-bearing experiments. The parameters of this regression, R2, are shown in Table 7. Both R1 and R2 are plotted together along the peridotite liquidus with the same parameter values given above for the Figure 26 plot (Figure 28a). Note that the curves are quite similar with an offset in log D of approximately 0.2 log units up to approximately 50 GPa, and the offset increases to approximately 0.45 log units by 100 GPa. This difference between the predicted log D values using R1 and R2 is slightly larger than the average difference between uncorrected and corrected log D values of the experiments (Figure 25). Setting the mole fraction C parameter to a value of 0.23 which is representative of the experimental abundance in C-saturated metallic melts, the curves are essentially the same (Figure 28b). This indicates that the activity correction procedure and the use of the C regression parameter similarly characterize the effect of C on W metal/silicate partitioning. Note that difference in predicted log D between R1 and R2 is within fit uncertainties of 0.20 and 0.35, respectively.

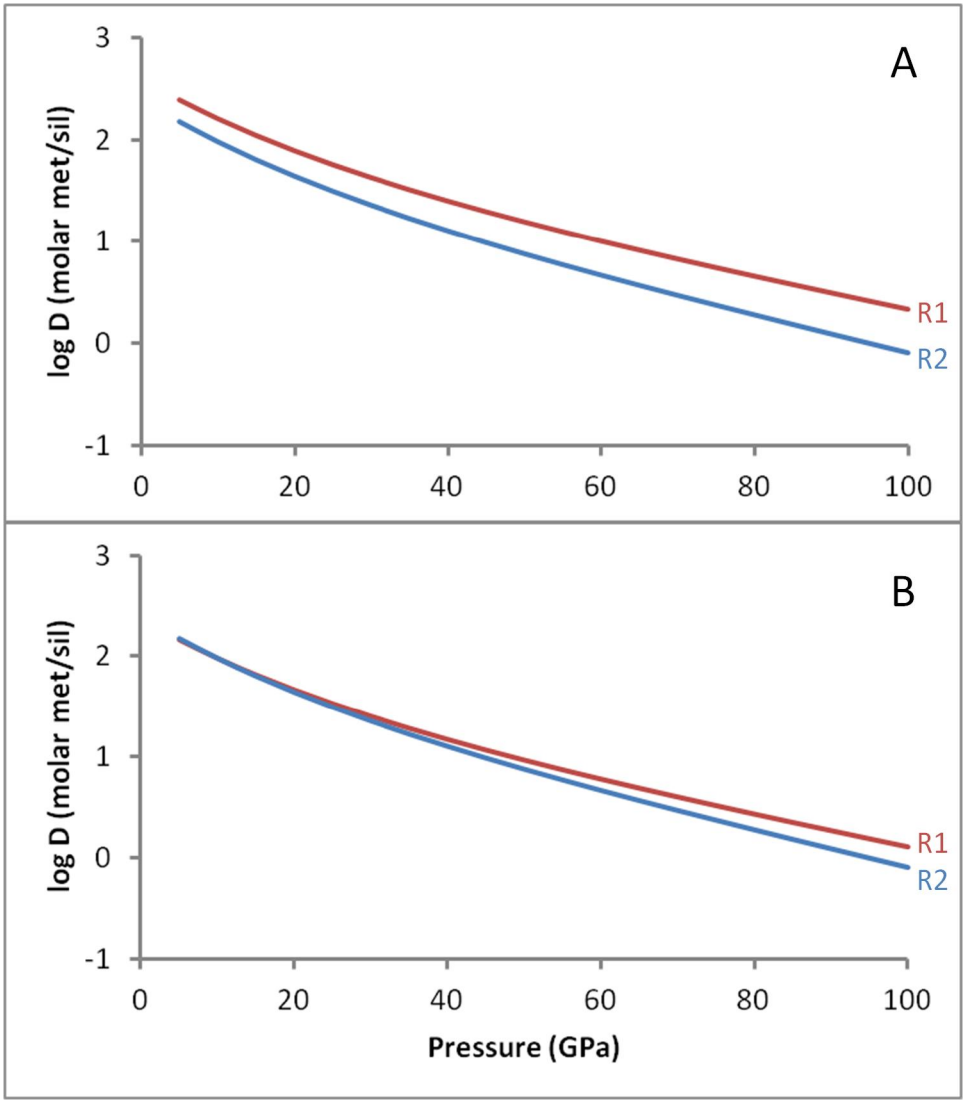

Figure 28. Regressions R2 and R1 plotted on the peridotite liquidus. The liquidus was based on experimental data of Herzberg and Zhang (1996) and Zerr et al. (1998). A) R1 and R2 with mole fraction carbon in R1 = 0.008. B) R1 and R2 with mole fraction carbon in R1 = 0.23.

Referring to Section 1.2 and equation (5), using the exchange partition coefficient allows for modeling W metal/silicate partitioning that is independent of fO_2 in that it does not require an fO_2 term in regressing metal/silicate partition coefficient data. Using the same data set as for regression R1, i.e. data with $P \geq 5$GPa, I calculated exchange partition coefficients for these data and regressed the log of the exchange partition coefficients giving regression R3 (Table 7). Plotting R3 along the peridotite

liquidus shows a similar curve to that of R1, which is in terms of log D and ΔIW (Figure 29). The range of K_D values is approximately two log units across a pressure range of 100 GPa, which is the same as the range of log D shown in Figure 27. This shows that using the exchange partition coefficient gives similar results to that of the molar partition coefficient without the need to specify the fO_2. In fact, fO_2 is implicit in the definition of K_D where the W partition coefficient divided by the Fe partition coefficient where the fO_2 is strongly influenced by the Fe-FeO equilibrium.

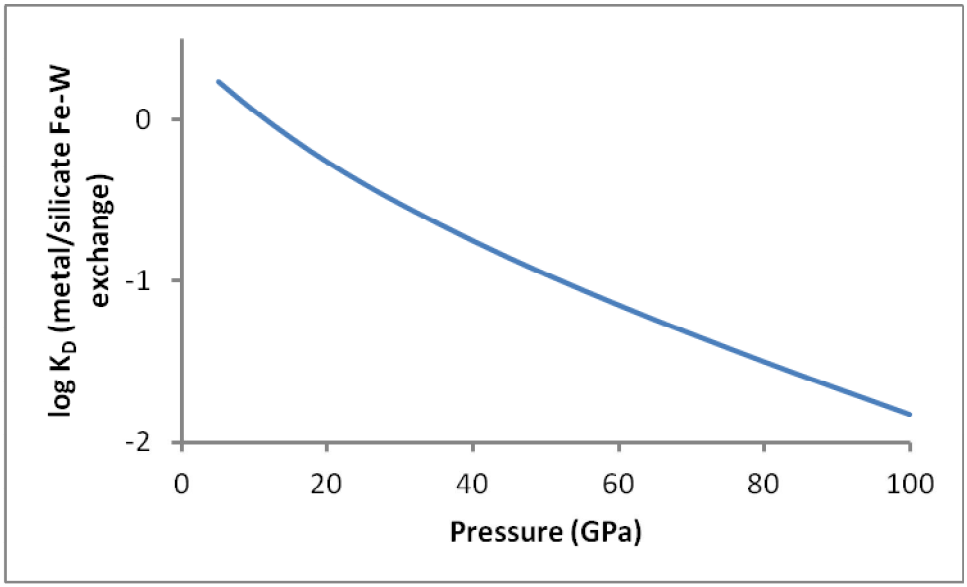

Figure 29. Regression R3 plotted on the peridotite liquidus. The liquidus was based on experimental data of Herzberg and Zhang (1996) and Zerr et al. (1998).

4 The W-WO_2 Buffer System

4.1 Data Analysis

The foundational data for characterizing the W-WO_2 oxygen buffer system (WWO) were x-ray diffraction patterns in the form of either two-dimensional CCD images (Figure 30) or one-dimensional energy spectra collected by a N-cooled, solid-state Ge, energy-dispersive detector. The 2-d diffraction patterns were processed using the Fit2D software, which integrates a diffraction image to produce a 1-d spectrum of 2-theta angle versus intensity (Hammersley et al., 1996). The 1-d energy spectra were converted to *d*-spacing versus intensity spectra by applying energy and 2-theta calibrations. Energy calibrations were based on radioactive Co^{57} and Cd^{109} sources, and Ag K_α and $K_{\beta 1}$ lines. The 2-theta calibration was based on a 1-bar x-ray diffraction pattern of Al_2O_3. The x-ray diffraction peaks in the experimental spectra were fitted using the PeakFit software, which also allowed for background subtraction. The output of the peak fitting procedure is a list of peak positions and intensities, along with statistics on the fit, including uncertainties on individual peak positions.

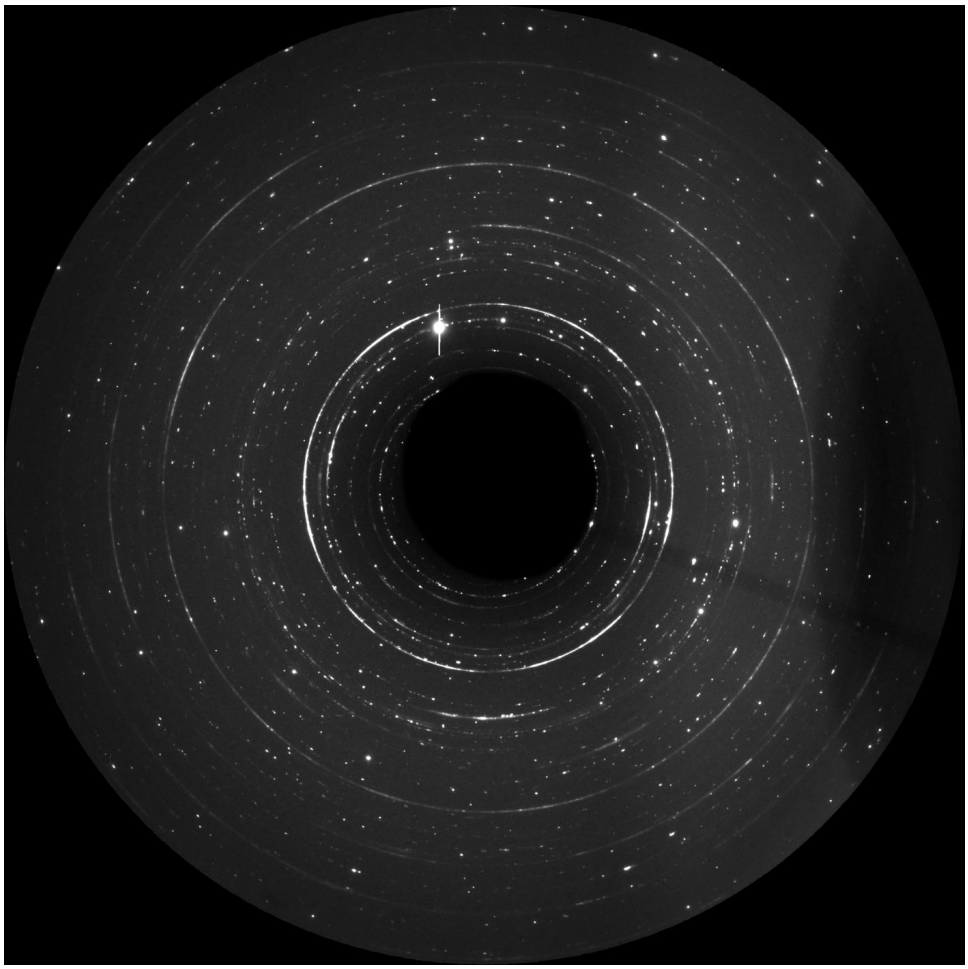

Figure 30. An example x-ray diffraction image for pattern G33_006 collected on CCD detector. Rings are crystal lattice plane reflections. High *d*-spacing reflections are nearest the center and decrease outward.

4.1.1 Unit-cell Determinations

The principal information I needed to obtain was the molar volume for the W and WO_2 phases at each P-T point, because the difference in molar volume between the phases is used to calculate the fO_2 of the WWO buffer. The molar volumes were calculated directly from the unit cell volumes, where the unit cell is the smallest unit of volume in a crystalline solid that contains all of the structural and symmetry information and that by translation can reproduce a pattern in all of space. In addition to unit cell volume, the number of formula units per unit cell, Z, was needed to calculate

molar volume. The value Z is usually known for structures that have been refined, but has to be determined if the structure is unknown or newly discovered.

4.1.1.1 Formula units per unit cell

In cases where Z is unknown, it can be estimated or inferred assuming the unit cell volume is known, and that reasonable constraints can be placed on the phase density. The number of formula units per unit cell can be calculated by $Z = 0.6023\rho V/M$, where ρ is density in g/cm^3, V is unit-cell volume in Å^3, and M is formula unit mass. The density $\rho = 1.66ZM/V = 1.66nzM/V$. In this equation, n is the number of molecules per unit cell and is generally equal to the multiplicity of the general crystal lattice site, which is related to and governed by the symmetry of the unit cell. The variable z is an integer corresponding to the number of molecules with mass M is the asymmetric (1/nth) part of the unit cell. The asymmetric part is the smallest unit of volume that contains all of the structural information and that by application of the symmetry operations can reproduce the unit cell. The density can be calculated if Z is known or vice versa, Z can be calculated if density is known. Alternatively, z can be varied with known values of n, M, and V, and the resulting calculated densities can be compared to probable constraints on density, thus determining an estimate of both Z and density (Pecharsky and Zavalij 2009).

4.1.2 Peak Indexing

4.1.2.1 Tungsten, sodium chloride, and magnesium oxides

For tungsten and the pressure calibrants (sodium chloride or magnesium oxide), peaks were indexed relative to published powder diffraction data (JCPDS). To guide

assignment of Miller indices at high pressures, the decrease in lattice plane spacings due to compression was estimated by using room-temperature equations of state. These phases are all of the isometric crystal system, and the lattice parameter *a* was calculated from the measured lattice plane *d*-spacings and the assigned Miller indices *h k l* by the equation $a = d_{meas}\sqrt{h^2 + k^2 + l^2}$. The average of the calculated lattice parameters for each reflection was taken as the lattice parameter for each phase in each pattern. Uncertainties were calculated as the standard error of the mean of the calculated lattice parameters for all indexed reflections. The quality of peak indexing was based on the difference between measured *d*-spacings and those calculated from the calculated lattice parameter for each reflection $d_{calc} = a_{calc}/\sqrt{h^2 + k^2 + l^2}$. The lattice parameters, calculated volumes and densities of W, and experimental pressures and temperatures are shown in Table 8.

Table 8. Lattice parameters, volumes, and densities of W in x-ray diffraction experiments. Values in parentheses are 1-sigma uncertainties in the least significant digits.

Pattern	*a (Å)*	*Unit-cell volume (Å^3)*	*Molar volume[a] (cm^3/mol)*	*Density (g/cm^3)*	*P (GPa)*	*T (K)*
JCPDS 1-bar	3.165	31.70	9.544	19.25		
T1160.048	3.131 (0)	30.70 (0)	9.244 (1)	19.88	17.9 (2)	2100 (20)
T1160.051	3.130 (1)	30.66 (4)	9.233 (11)	19.91	17.4 (3)	1900 (20)
T1160.052	3.129 (2)	30.63 (5)	9.221 (16)	19.93	17.2 (3)	1700 (20)
T1160.055	3.128 (1)	30.59 (4)	9.211 (11)	19.95	16.7 (3)	1500 (20)
T1160.056	3.125 (0)	30.51 (1)	9.187 (4)	20.00	15.9 (2)	1100 (20)
T1160.059	3.123 (1)	30.47 (3)	9.174 (9)	20.03	14.8 (2)	700 (20)
T1160.060	3.125 (1)	30.52 (3)	9.190 (9)	20.00	12.6 (2)	300 (0)
G33_006	3.116 (0)	30.24 (1)	9.106 (2)	20.18	21.6 (12)	1687 (143)
G33_008	3.114 (0)	30.21 (1)	9.096 (3)	20.20	20.6 (11)	1367 (133)
G33_010	3.113 (1)	30.18 (2)	9.088 (5)	20.22	20.6 (11)	1279 (130)
G33_011	3.113 (1)	30.17 (2)	9.084 (6)	20.23	20.2 (11)	1144 (126)
G33_012	3.113 (0)	30.17 (1)	9.085 (2)	20.23	19.8 (10)	1060 (124)
G33_015	3.108 (1)	30.03 (2)	9.042 (5)	20.32	18.5 (1)	300 (0)
G33_016	3.081 (1)	29.25 (3)	8.808 (9)	20.87	29.0 (2)	300 (0)
G33_017	3.057 (1)	28.58 (4)	8.606 (11)	21.35	39.2 (3)	300 (0)
G33_022	3.062 (0)	28.71 (0)	8.644 (1)	21.26	43.6 (13)	1918 (150)
G33_023	3.060 (0)	28.66 (1)	8.630 (2)	21.29	43.1 (12)	1619 (141)
G33_025	3.059 (0)	28.62 (1)	8.618 (3)	21.32	43.1 (11)	1472 (136)
G33_026	3.059 (0)	28.61 (1)	8.616 (4)	21.33	42.5 (11)	1291 (131)
G33_027	3.058 (1)	28.59 (2)	8.608 (5)	21.35	42.6 (10)	1206 (128)
G33_029	3.058 (1)	28.59 (2)	8.607 (5)	21.35	42.0 (10)	1053 (123)
G33_031	3.056 (0)	28.54 (1)	8.595 (4)	21.38	42.1 (9)	902 (119)
G33_047	3.036 (1)	27.99 (2)	8.429 (6)	21.80	56.7 (14)	2245 (160)
G33_048	3.037 (1)	28.00 (2)	8.432 (6)	21.80	55.4 (13)	1949 (151)
G33_050	3.036 (2)	27.99 (5)	8.428 (15)	21.81	55.0 (13)	1798 (146)
G33_053	3.036 (2)	27.98 (4)	8.424 (13)	21.82	54.9 (12)	1726 (144)
G33_054	3.033 (2)	27.90 (7)	8.402 (20)	21.87	55.3 (13)	1510 (138)
G33_056	3.033 (1)	27.89 (2)	8.397 (7)	21.89	55.2 (11)	1392 (134)

Pattern	*a (Å)*	*Unit-cell volume ($Å^3$)*	*Molar volume[a] (cm^3/mol)*	*Density (g/cm^3)*	*P (GPa)*	*T (K)*
G33_057	3.031 (1)	27.85 (3)	8.387 (10)	21.91	55.4 (11)	1300 (131)
G33_060	3.032 (0)	27.86 (1)	8.388 (4)	21.91	54.0 (9)	980 (121)
G33_061	3.029 (1)	27.80 (2)	8.370 (7)	21.96	52.6 (2)	300 (0)
G33_083	3.012 (1)	27.32 (2)	8.225 (5)	22.34	68.4 (13)	2033 (154)
G33_085	3.009 (1)	27.24 (3)	8.202 (8)	22.41	68.7 (12)	1723 (144)
G33_093	3.005 (0)	27.13 (1)	8.167 (3)	22.50	69.5 (10)	1351 (133)
G33_096	3.005 (1)	27.13 (1)	8.168 (4)	22.50	68.9 (10)	1215 (128)
G33_098	3.004 (0)	27.12 (1)	8.165 (3)	22.51	68.5 (9)	1046 (123)
G33_099	3.002 (0)	27.06 (1)	8.147 (3)	22.56	67.0 (1)	300 (0)
WWO2a_012	3.125 (0)	30.53 (0)	9.193 (1)	19.99	12.7 (1)	375 (10)
WWO2a_013	3.128 (2)	30.62 (4)	9.219 (13)	19.93	12.1 (3)	472 (10)
WWO2a_014	3.129 (2)	30.62 (7)	9.220 (21)	19.93	12.5 (4)	575 (10)
WWO2a_015	3.130 (8)	30.65 (23)	9.230 (69)	19.91	12.1 (13)	575 (10)
WWO2a_018	3.158 (1)	31.51 (3)	9.486 (10)	19.37	3.4 (2)	675 (10)
WWO2a_019	3.162 (5)	31.61 (15)	9.518 (46)	19.31	2.4 (8)	675 (10)
WWO2a_020	3.156 (3)	31.43 (10)	9.464 (29)	19.42	4.2 (5)	675 (10)
WWO2a_021	3.147 (2)	31.16 (4)	9.384 (13)	19.58	6.1 (2)	485 (10)
WWO2b_024	3.082 (1)	29.26 (3)	8.811 (8)	20.86	29.2 (2)	375 (10)
WWO2b_026	3.085 (1)	29.36 (2)	8.839 (7)	20.79	28.2 (2)	475 (10)
WWO2b_028	3.090 (3)	29.52 (9)	8.887 (28)	20.68	26.4 (6)	575 (10)
WWO2b_030	3.099 (1)	29.75 (2)	8.959 (6)	20.51	23.4 (2)	625 (10)
WWO2c_009	3.072 (5)	28.99 (14)	8.729 (42)	21.05	34.4 (10)	715 (10)
WWO2c_011	3.075 (7)	29.09 (20)	8.758 (59)	20.98	33.0 (14)	715 (10)
WWO2c_018	3.064 (2)	28.77 (4)	8.663 (13)	21.21	36.5 (3)	375 (10)
WWO2a_008	3.121 (2)	30.40 (5)	9.154 (14)	20.08	14.0 (3)	300
WWO2a_010	3.124 (2)	30.50 (5)	9.183 (16)	20.01	12.8 (3)	300
WWO2a_023	3.141 (1)	30.98 (2)	9.328 (7)	19.70	7.4 (2)	300
WWO2b_005	3.091 (2)	29.54 (5)	8.895 (15)	20.66	25.0 (4)	300
WWO2b_007	3.094 (1)	29.63 (4)	8.922 (12)	20.60	23.7 (3)	300
WWO2b_033	3.070 (1)	28.93 (2)	8.711 (7)	21.10	33.8 (2)	300
WWO2c_004	3.054 (6)	28.47 (16)	8.573 (49)	21.44	41.0 (13)	300

Pattern	*a (Å)*	*Unit-cell volume ($Å^3$)*	*Molar volume[a] (cm^3/mol)*	*Density (g/cm^3)*	*P (GPa)*	*T (K)*
WWO2c_015	3.089 (5)	29.47 (14)	8.873 (43)	20.71	27.0 (10)	575 (10)
WWO2c_018	3.064 (2)	28.77 (4)	8.663 (13)	21.21	36.5 (4)	375 (10)
WWO_006	3.081 (1)	29.25 (4)	8.807 (12)	20.87	29.1 (3)	300
WWO_008	3.071 (1)	28.97 (3)	8.722 (9)	21.07	33.3 (2)	300
WWO_009	3.060 (1)	28.66 (2)	8.631 (5)	21.29	37.9 (2)	300
WWO_010	3.051 (0)	28.40 (1)	8.552 (2)	21.49	42.1 (1)	300
WWO_015	3.041 (2)	28.13 (7)	8.470 (20)	21.70	46.7 (1)	300
WWO_016	3.031 (1)	27.85 (1)	8.385 (4)	21.92	51.7 (1)	300
WWO_018	3.027 (1)	27.73 (4)	8.348 (11)	22.01	54.0 (3)	300
WWO_019	3.023 (2)	27.62 (5)	8.316 (14)	22.10	55.9 (5)	300
WWO_020	3.019 (1)	27.51 (3)	8.283 (8)	22.19	58.1 (5)	300
WWO_025	3.006 (0)	27.17 (1)	8.180 (4)	22.47	64.8 (1)	300
WWO_026	3.001 (0)	27.03 (1)	8.140 (2)	22.58	67.5 (1)	300
WWO_027	2.996 (0)	26.90 (1)	8.098 (2)	22.69	70.4 (1)	300
WWO_028	2.992 (0)	26.80 (0)	8.068 (1)	22.78	72.5 (0)	300

[a]Molar volumes are cubic cm per mole of formula units.

4.1.2.2 Tungsten dioxide

Indexing of WO_2 was more complex than for the cubic symmetry phases, W, NaCl, and MgO, due to the lower crystal symmetry of WO_2, which results in a greater number of x-ray diffraction peaks than the higher symmetry phases. Also, WO_2 exhibits multiple crystal structural phase changes at higher pressures and temperatures. According to the literature, the crystal structure of WO_2 is either a monoclinic (Bolzan et al. 1995) or an orthorhombic symmetry (Sundberg et al. 1994), and so determination of lattice parameters from x-ray diffraction data requires a more sophisticated method as compared to cubic-structured phases. This is particularly true for the monoclinic phases since the equation for calculating lattice spacings results in a non-linear problem, i.e. it cannot be solved by a linear fit. Miller indices were assigned to each identified peak in the patterns and lattice parameters were calculated using the Solver extension in Microsoft Excel with the Solver target set to minimize the squares of the differences (Δd) of measured and calculated d-spacings. Non-linear solutions in Solver are based on the Generalized Reduced Gradient (GRG2) non-linear optimization code of Lasdon and Warren (1978). Uncertainties were calculated for the Solver-derived lattice parameters and the calculated unit cell volumes using the SolverAid function in the MacroBundle code of de Levie (2008).

The case of WO_2 was made more complex by the discovery of an additional crystal structural transformation in LHDAC data collected for the present study at pressures greater than 40 GPa. Those data could not be indexed to any published crystal structure. Therefore, the method of successive dichotomy as coded in the software DICVOL06

was used to determine the unit cell of this structure (Boultif and Louer, 2004); DICVOL06 will hereafter referred to as DICVOL.

Beginning with the lowest pressure LHDAC data set, WO_2 peak positions as 2-theta angle along with their uncertainties were input to DICVOL powder indexing software. Software parameters were adjusted to obtain a fit based on the greatest number of peaks with the highest resulting figures of merit (FoM). The FoM denoted as *M* is a measure level of misfit between observed and calculated variables relating to reciprocal lattice vectors and Miller indices of individual reflections. The higher the FoM the greater the confidence that a particular solution is the correct representation of the unknown structure. Preference was given to solutions based on the greatest number of peaks as this was thought to most completely represent the diffraction pattern and therefore most fully characterize the structure. Pattern indexing by the dichotomy method were conducted with patterns from each of the temperatures in the 20 GPa cooling cycle. Solutions were determined only in the orthorhombic system, and ultimately solutions were obtained for multiple patterns that were in agreement with the *Pnma* structure of Sundberg et al. (1994). Matching solutions to the Sundberg *Pnma* structure was taken as the ultimate confirmation of the correct solution. Miller indices were assigned to each identified peak in the patterns and lattice parameters were calculated at each temperature using the Solver software in Microsoft Excel. The diffraction spectrum for G33_006 (highest temperature pattern) compared to the 1-bar spectrum calculated using the Sundberg et al. (1994) structure data are shown in Figure 31. See Table 9 for lattice parameters, volumes, densities, and experimental pressure and temperature conditions.

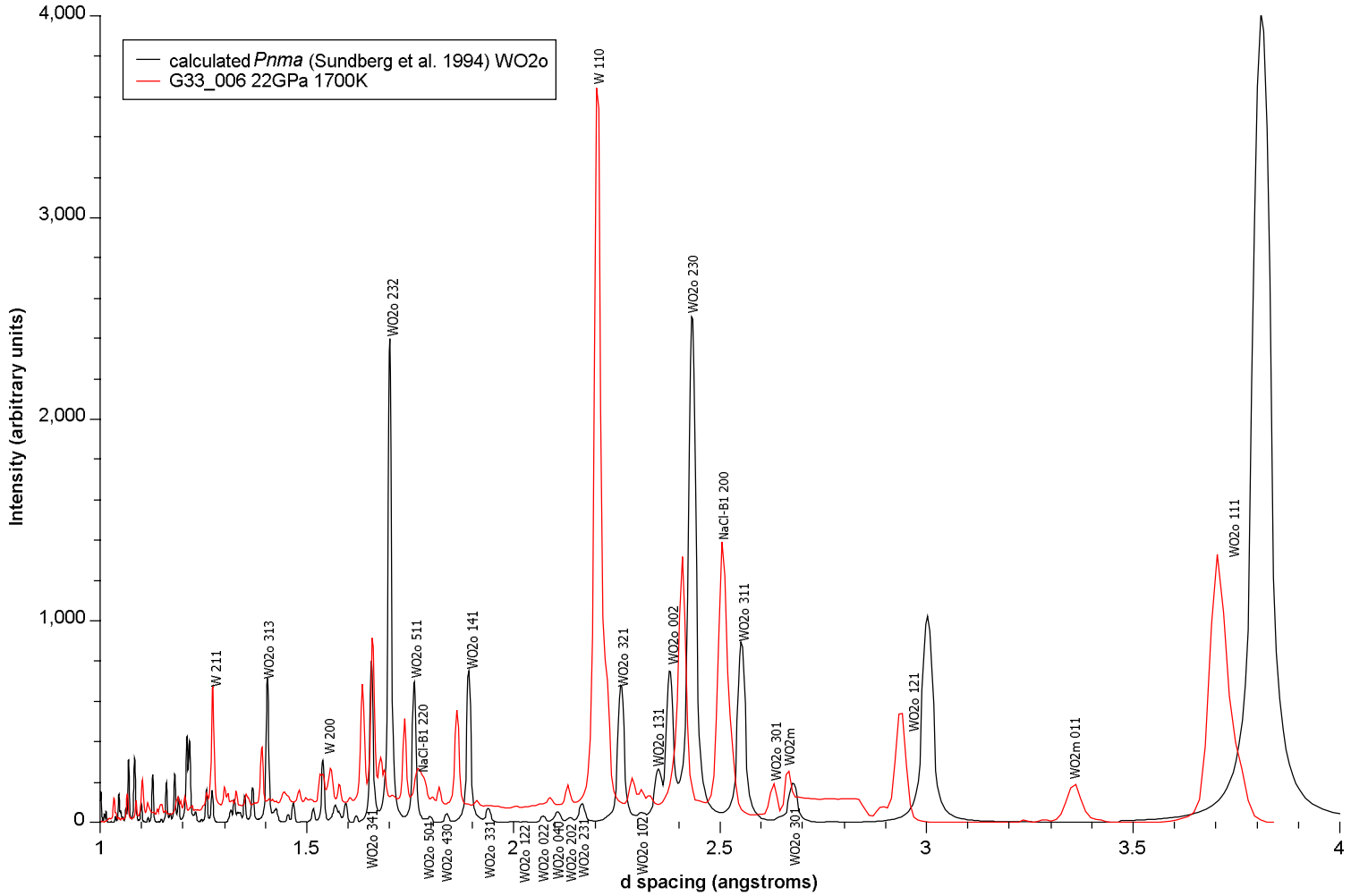

Figure 31. X-ray diffraction spectrum showing G33_006 and a calculated pattern for the *Pnma* structure of WO_2 described by Sundberg et al. (1994). Peaks in high pressure pattern offset in *d*-spacing by approximately -0.1 Å relative to 1-bar pattern due to compression.

Table 9. Lattice parameters, volumes, and densities of WO_2 phases in x-ray diffraction experiments. 1-bar parameters for *Pnma* structure are from Sundberg et al. (1994), and for $P2_1/c$ structure are from Bolzan et al. (1995). Molar volumes are cubic cm per mole of formula units. Values in parentheses are 1-sigma uncertainties in the least significant digits.

$P2_1/c$	**Z=4**								
Pattern	*a (Å)*	*b (Å)*	*c (Å)*	*beta (degrees)*	*Unit-cell volume ($Å^3$)*	*Molar volume (cm^3/mol)*	*Density (g/cm^3)*	*P (GPa)*	*T (K)*
1-bar	5.577	4.899	5.664	120.7	133.1	20.04	10.77	1 bar	300
WWO2a_008	5.492 (6)	4.792 (3)	5.597 (2)	121.2 (1)	126.0 (1)	18.97 (2)	11.37 (1)	13.2 (1)	300
WWO2a_017	5.574 (4)	4.895 (5)	5.653 (6)	120.8 (1)	132.5 (1)	19.95 (2)	10.81 (1)	2.3 (0)	675
WWO2a_019	5.578 (9)	4.910 (8)	5.642 (7)	120.9 (1)	132.5 (3)	19.95 (4)	10.82 (2)	2.3 (0)	675
WWO2a_020	5.604 (6)	4.855 (7)	5.704 (5)	121.1 (1)	132.9 (2)	20.00 (2)	10.79 (1)	2.4 (1)	675
WWO2b_005	5.402 (15)	4.723 (10)	5.526 (9)	121.5 (2)	120.2 (3)	18.10 (5)	11.92 (3)	25.0 (2)	300
WWO2b_007	5.379 (24)	4.745 (5)	5.533 (10)	122.0 (1)	119.8 (5)	18.03 (7)	11.97 (5)	25.0 (2)	300
WWO2b_024	5.344 (12)	4.744 (3)	5.539 (7)	122.0 (1)	119.1 (3)	17.93 (4)	12.03 (3)	25.6 (2)	375
WWO2b_026	5.386 (11)	4.759 (6)	5.553 (11)	122.5 (2)	120.1 (3)	18.08 (4)	11.93 (3)	23.3 (2)	475
WWO2b_028	5.444 (5)	4.763 (4)	5.567 (6)	121.7 (1)	122.8 (1)	18.49 (2)	11.67 (1)	19.8 (1)	575
WWO2b_030	5.491 (11)	4.769 (4)	5.577 (9)	122.0 (1)	123.8 (2)	18.64 (3)	11.58 (2)	18.6 (3)	625
WWO2b_033	5.397 (9)	4.714 (8)	5.507 (7)	121.5 (1)	119.4 (2)	17.98 (3)	12.00 (2)	25.4 (5)	300
WWO2c_004	5.279 (2)	4.659 (1)	5.504 (2)	122.6 (0)	114.1 (0)	17.17 (1)	12.56 (0)	41.5 (9)	300
WWO2c_009	5.403 (10)	4.689 (4)	5.548 (4)	122.7 (1)	118.3 (2)	17.80 (3)	12.12 (2)	32.1 (1)	715
WWO2c_011	5.340 (16)	4.714 (13)	5.513 (10)	121.8 (2)	118.0 (4)	17.76 (6)	12.15 (4)	31.8 (4)	715
WWO2c_015	5.379 (4)	4.737 (6)	5.487 (4)	121.3 (1)	119.4 (1)	17.98 (2)	12.00 (1)	26.7 (8)	575
WWO2c_018	5.368 (9)	4.671 (13)	5.516 (10)	123.1 (2)	115.9 (2)	17.45 (4)	12.36 (3)	35.1 (4)	375
WWO2c_020	5.339 (14)	4.688 (14)	5.516 (9)	123.5 (2)	115.1 (3)	17.34 (4)	12.45 (3)	37.5 (9)	300

Pnma	**Z=12**							
Pattern	*a (Å)*	*b (Å)*	*c (Å)*	*Unit-cell volume (Å3)*	*Molar volume (cm^3/mol)*	*Density (g/cm^3)*	*P (GPa)*	*T (K)*
1-bar	9.716	8.438	4.756	390.0	19.57	11.03	0.0	300
G33_006	9.634 (2)	8.349 (2)	4.575 (1)	368.0 (1)	18.47 (1)	11.68 (1)	21.6 (12)	1687 (143)
G33_008	9.620 (5)	8.344 (2)	4.566 (1)	366.5 (2)	18.39 (1)	11.73 (1)	20.6 (11)	1367 (133)
G33_010	9.609 (5)	8.332 (3)	4.567 (2)	365.6 (3)	18.35 (1)	11.76 (1)	20.6 (11)	1279 (130)

G33_011	9.610 (7)	8.335 (4)	4.567 (2)	365.8 (3)	18.36 (2)	11.75 (1)	20.2 (11)	1144 (126)
G33_012	9.612 (10)	8.330 (5)	4.562 (2)	365.3 (5)	18.33 (2)	11.77 (2)	19.8 (10)	1060 (124)
G33_015	9.583 (8)	8.319 (5)	4.559 (2)	363.4 (4)	18.24 (2)	11.83 (1)	18.5 (1)	300
G33_016	9.359 (12)	8.265 (18)	4.552 (8)	352.1 (7)	17.67 (3)	12.21 (2)	29.0 (2)	300
G33_017	9.315 (8)	8.100 (7)	4.528 (4)	341.7 (6)	17.15 (3)	12.58 (2)	39.2 (3)	300
T1160.048	9.609 (7)	8.275 (7)	4.688 (3)	372.8 (3)	18.71 (2)	11.53 (1)	17.9 (2)	2100 (20)
T1160.051	9.601 (2)	8.283 (1)	4.676 (1)	371.9 (1)	18.66 (0)	11.56 (0)	17.4 (3)	1900 (20)
T1160.052	9.564 (14)	8.272 (23)	4.705 (11)	372.2 (10)	18.68 (5)	11.55 (3)	17.2 (3)	1700 (20)
T1160.055	9.594 (8)	8.263 (10)	4.671 (7)	370.3 (6)	18.58 (3)	11.61 (2)	16.7 (3)	1500 (20)
T1160.056	9.571 (14)	8.290 (13)	4.663 (13)	370.0 (9)	18.57 (5)	11.62 (3)	15.9 (2)	1100 (20)
T1160.059	9.600 (12)	8.258 (13)	4.648 (10)	368.5 (8)	18.49 (4)	11.67 (3)	14.8 (2)	700 (20)
T1160.060	9.543 (12)	8.272 (13)	4.667 (8)	368.4 (6)	18.49 (3)	11.67 (2)	12.6 (2)	300
T1160.081	9.598 (11)	8.389 (24)	4.721 (8)	380.1 (9)	19.08 (5)	11.31 (3)	10.4 (3)	1300 (20)
T1160.085	9.601 (17)	8.345 (9)	4.751 (7)	380.7 (7)	19.10 (4)	11.29 (3)	5.8 (5)	300

P2/m **Z=12**

Pattern	*a (Å)*	*b (Å)*	*c (Å)*	*Beta (degrees)*	*Unit-cell volume ($Å^3$)*	*Molar volume (cm^3/mol)*	*Density (g/cm^3)*	*P (GPa)*	*T(K)*
G33_022	11.586 (5)	3.474 (1)	8.683 (4)	110.8 (0)	326.7 (2)	16.39 (1)	13.16	43.6 (13)	1918 (150)
G33_023	11.569 (7)	3.472 (2)	8.676 (6)	110.8 (0)	325.8 (2)	16.35 (1)	13.20	43.1 (12)	1619 (141)
G33_025	11.567 (7)	3.470 (2)	8.676 (5)	110.8 (0)	325.5 (2)	16.33 (1)	13.21	43.1 (11)	1472 (136)
G33_026	11.581 (5)	3.467 (2)	8.675 (4)	110.8 (0)	325.6 (2)	16.34 (1)	13.21	42.5 (11)	1291 (131)
G33_027	11.567 (6)	3.469 (2)	8.664 (5)	110.7 (0)	325.1 (2)	16.31 (1)	13.23	42.6 (10)	1206 (128)
G33_029	11.566 (5)	3.467 (1)	8.659 (4)	110.7 (0)	324.7 (2)	16.29 (1)	13.24	42.0 (10)	1053 (123)
G33_031	11.567 (5)	3.466 (1)	8.655 (4)	110.7 (0)	324.5 (2)	16.28 (1)	13.25	42.1 (9)	902 (119)
G33_047	11.520 (21)	3.452 (5)	8.570 (18)	110.8 (2)	318.6 (6)	15.99 (3)	13.49	56.7 (14)	2245 (160)
G33_048	11.518 (13)	3.451 (3)	8.575 (10)	110.8 (1)	318.6 (4)	15.99 (2)	13.50	55.4 (13)	1949 (151)
G33_050	11.496 (14)	3.446 (3)	8.582 (11)	110.7 (1)	318.1 (4)	15.96 (2)	13.52	55.0 (13)	1798 (146)
G33_053	11.505 (20)	3.444 (5)	8.585 (16)	110.8 (2)	318.0 (6)	15.96 (3)	13.52	54.9 (12)	1726 (144)
G33_054	11.477 (16)	3.446 (3)	8.578 (12)	110.7 (1)	317.4 (4)	15.93 (2)	13.55	55.3 (13)	1510 (138)
G33_056	11.493 (17)	3.441 (4)	8.579 (13)	110.9 (1)	317.0 (5)	15.91 (2)	13.56	55.2 (11)	1392 (134)
G33_057	11.479 (16)	3.441 (3)	8.578 (12)	110.8 (1)	316.8 (5)	15.90 (2)	13.57	55.4 (11)	1300 (131)

G33_060	11.480 (14)	3.441 (3)	8.564 (11)	110.8 (1)	316.3 (4)	15.87 (2)	13.59	54.0 (9)	980 (121)
G33_061	11.479 (13)	3.434 (3)	8.560 (10)	110.9 (1)	315.2 (4)	15.82 (2)	13.64	52.6 (2)	300 (0)
G33_083	11.230 (32)	3.440 (7)	8.508 (25)	111.7 (3)	305.4 (7)	15.33 (4)	14.08	68.4 (13)	2033 (154)
G33_085	11.214 (28)	3.448 (6)	8.479 (20)	111.3 (2)	305.5 (7)	15.33 (3)	14.07	68.7 (12)	1723 (144)
G33_093	11.235 (23)	3.470 (6)	8.284 (19)	109.8 (2)	303.8 (6)	15.25 (3)	14.15	69.5 (10)	1351 (133)
G33_096	11.164 (32)	3.464 (10)	8.359 (25)	110.3 (3)	303.2 (8)	15.22 (4)	14.18	68.9 (10)	1215 (128)
G33_098	11.119 (19)	3.465 (5)	8.334 (14)	110.0 (2)	301.8 (5)	15.14 (3)	14.25	68.5 (9)	1046 (123)
G33_099	11.123 (36)	3.470 (9)	8.315 (26)	110.0 (3)	301.5 (9)	15.13 (5)	14.26	67.0 (1)	300 (0)

Comparison of peaks in the 20 GPa heating cycle were made to the 40 GPa heating cycle and it was apparent that the *Pnma* structure was not present. The major orthorhombic peaks, *(111)* and *(230)*, present in all 20 GPa patterns were completely absent in the 40 GPa and higher pressure data (Figure 32). Some similarities were observed between the 40, 50 and 60 GPa cycles, though additional peaks are present in the 50 and 60 GPa data suggesting that an additional phase was present at pressures greater than 50 GPa.

Patterns from the 40 GPa data were analyzed using DICVOL and all solutions determined were in the monoclinic system. A wide range of solutions was determined by varying the parameter space for DICVOL, but a single solution was determined based on 20 input peaks with all peaks in the pattern indexing with *delta-d* values less than 0.004 Å. The structure is in the *P2/m* space group as reported in the DICVOL results, and is here termed WO_2-hpm (for high pressure monoclinic). The calculated volumes and densities were in reasonable agreement in comparison to the volumes calculated for the *Pnma* structure at lower presssures, and they followed the guidance that the number of formula units per unit cell should conform to the symmetry of the unit cell. Estimation of *Z* was based on known chemical composition and the approximate density of WO_2 in the pressure range of interest. The calculated densities in the 40 GPa set for WO_2-hpm were approximately 12 percent greater than in the *Pnma* structure at approximately 20 GPa, which is consistent with approximately 20 GPa of compression and a phase change. The density of WO_2 in the *Pnma* structure at 20 GPa is approximately 9 percent greater than at 1-bar in the $P2_1/c$ structure. The $P2_1/c$ and *Pnma* crystal structures are shown in Figure 33.

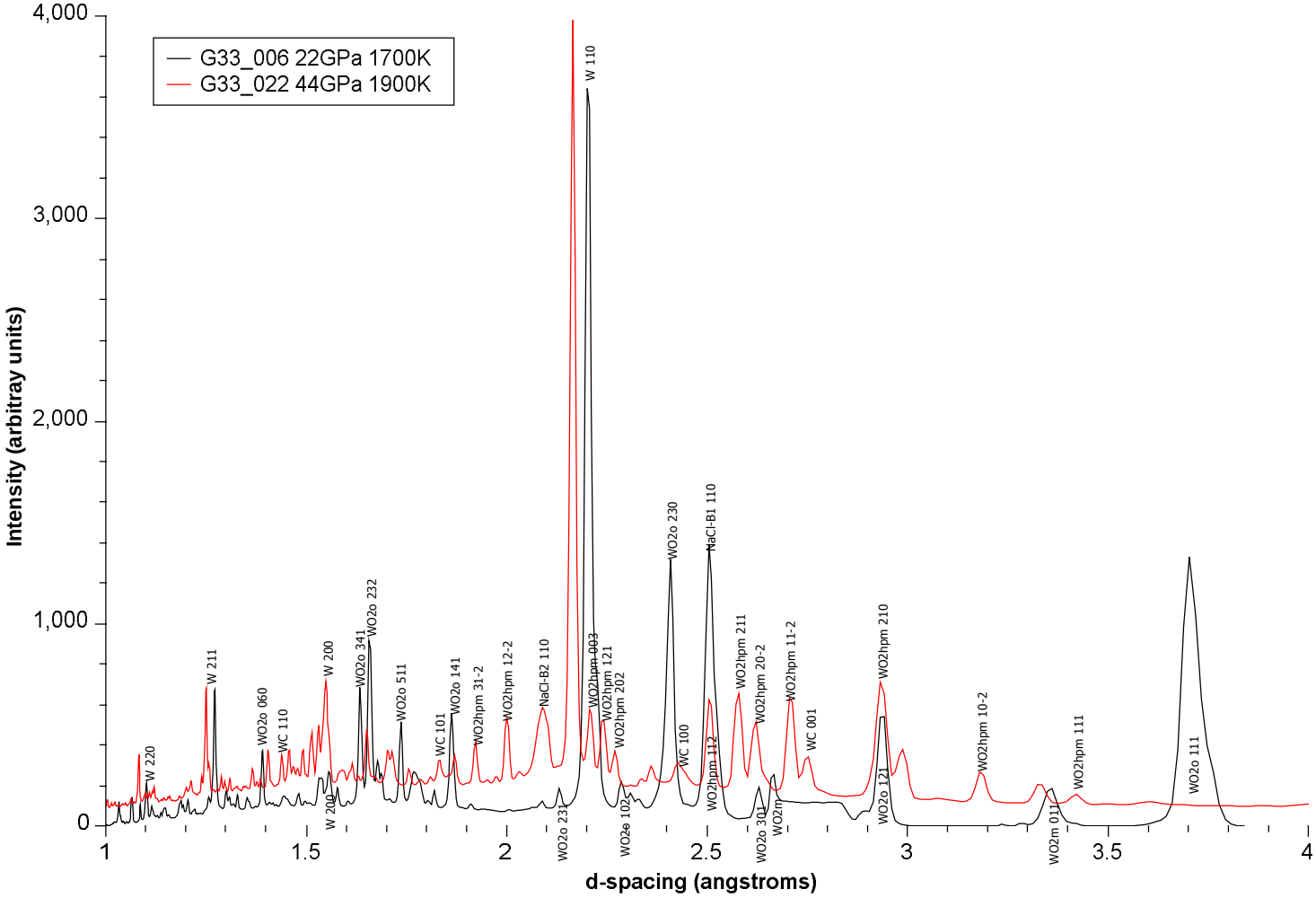

Figure 32. X-ray diffraction spectrum showing patterns G33_006 and G33_022. The *Pnma* structure of WO_2 described by Sundberg et al. (1994) is present in spectrum 006 but is not present in 022. The *d*-spacing offset between these two spectra is due to compression.

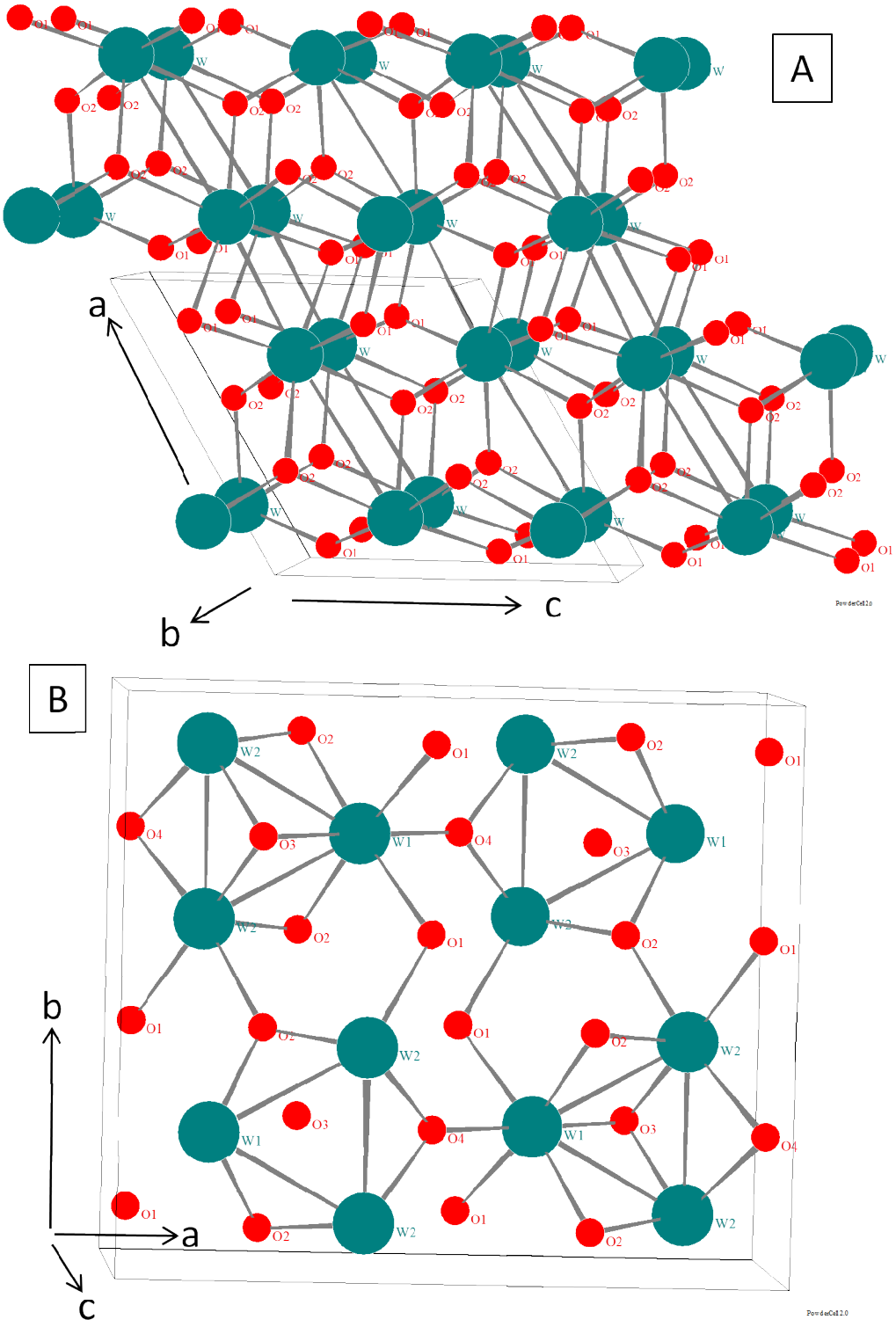

Figure 33. Structure models of WO_2: (A) monoclinic, space group $P2_1/c$ (Bolzan et al., 1995), stable form at ambient conditions; and (B) orthorhombic, space group *Pnma* (Sundberg et al., 1994), high pressure and temperature phase. Unit cells shown by thin black lines and crystallographic axes labeled a, b, and c.

Solutions determined using DICVOL for the 50 and 60 GPa peak sets were not equivalent with the P2/m structure of the 40 GPa set. However, as mentioned previously some of the peaks could be matched based on approximately one to two percent delta-d values between 40 and 50, and 50 and 60 GPa sets, consistent with approximately 10 GPa compressions between these sets. The Miller indices of the matching peaks were propagated to these higher pressure data sets and lattice parameters were determined. The resulting volumes and densities for the 50 and 60 GPa sets formed an approximately linear trend with the 40 GPa data, suggesting that the peak assignments and identification of the P2/m structure in the 50 and 60 GPa data were reasonable. The changes in density between the 40 and 50 GPa, and 50 and 60 GPa sets were approximately three and five percent, respectively. These density changes were consistent with the amounts of compression between these sets. However, propagation of WO2-hpm peak indexing to the 60 GPa data was brought into question during equation of state fitting for the WO2-hpm phase. Therefore, it is not certain whether the WO2-hpm is present in the highest pressure data set.

Attempts were made to index the higher pressure (>40 GPa) data to a monoclinic WO_3 structure. Bouvier et al. (2002) documented three monoclinic structures in WO_3 with phase boundaries at approximately 24 and 31 GPa. The highest pressure structure of Bouvier et al. (2002) was used as the reference for indexing. Many prominent peaks were unindexed and calculated molar volumes were not reasonable in comparison to the data of Bouvier et al. (2002) in the pressure range of 24 to 31 GPa. Additionally, the experimental conditions in the LHDAC were not conducive to producing a more oxidized form of tungsten oxide; i.e. no source of oxygen.

The proposed orthorhombic unit cell of Dewhurst and Lowther (2001) does not fit the high-P-T data collected on WO_2. A list of Miller indices (*hkl*) was calculated based on the Dewhurst and Lowther (2001) structure and simple peak indexing by matching Miller indices to the experimental data did not show any compelling correlation between the *hkl* list and *d*-spacings in the diffraction patterns.

4.1.2.3 Tungsten carbide

For the LHDAC experiments, an additional coexisting phase was present in all spectra of the 40, 50, and 60 GPa data, and was identified as tungsten carbide (WC). This identification is based on least squares minimization of the misfit of calculated lattice spacings using assigned Miller indices from the JCPDS card for WC, and is consistent with calculations of peak positions from a thermal equation of state for WC (Litasov, 2010). The source of the carbon to produce WC was undoubtedly from the diamond anvils due to the high temperatures generated by laser heating. This has been observed in laser heated experiments including melting experiments in this study.

WC was also observed in diffraction data in the MAP experiments. Identification and indexing of these peaks was carried out as for the LHDAC experiments. Unlike the LHDAC experiments, the WC peaks were due to interaction of the xray beam with the WC cubes of the MAP assembly. Consequently, they do not represent a coexisting experimental phase. Identification of these peaks was useful in terms of removing them from consideration as belonging to an experimental phase such as WO_2. Lattice parameter values and unit-cell volumes are listed in Table 10.

Table 10. Lattice parameters, and unit-cell volumes of WC in x-ray diffraction experiments. Values in parentheses are 1-sigma uncertainties in the least significant digits.

Pattern	a (Å)	c (Å)	c/a	Unit-cell volume (Å3)
G33_022	2.811 (6)	2.752 (6)	0.979 (3)	18.84 (7)
G33_023	2.805 (4)	2.758 (4)	0.983 (2)	18.80 (4)
G33_025	2.807 (7)	2.752 (7)	0.980 (3)	18.77 (8)
G33_026	2.806 (7)	2.752 (7)	0.981 (3)	18.76 (8)
G33_027	2.804 (7)	2.752 (7)	0.981 (3)	18.73 (8)
G33_029	2.803 (7)	2.749 (7)	0.981 (4)	18.71 (8)
G33_031	2.801 (6)	2.747 (6)	0.981 (3)	18.67 (8)
G33_047	2.801 (4)	2.760 (10)	0.985 (4)	18.75 (7)
G33_048	2.805 (4)	2.754 (8)	0.982 (3)	18.77 (7)
G33_050	2.802 (3)	2.750 (8)	0.981 (3)	18.70 (6)
G33_053	2.801 (1)	2.763 (2)	0.986 (1)	18.78 (2)
G33_054	2.800 (2)	2.746 (3)	0.981 (1)	18.65 (3)
G33_056	2.797 (2)	2.755 (4)	0.985 (1)	18.66 (3)
G33_057	2.796 (2)	2.754 (3)	0.985 (1)	18.65 (2)
G33_060	2.795 (2)	2.750 (2)	0.984 (1)	18.60 (2)
G33_061	2.791 (2)	2.747 (2)	0.984 (1)	18.54 (2)
G33_083	2.787 (2)	2.738 (6)	0.983 (2)	18.42 (4)
G33_085	2.787 (2)	2.738 (6)	0.982 (2)	18.42 (4)
G33_091	2.779 (3)	2.743 (3)	0.987 (2)	18.34 (4)
G33_093	2.779 (2)	2.740 (2)	0.986 (1)	18.32 (2)
G33_096	2.776 (2)	2.738 (2)	0.986 (1)	18.28 (2)
G33_098	2.774 (4)	2.738 (3)	0.987 (2)	18.25 (4)
G33_099	2.778 (7)	2.733 (4)	0.984 (3)	18.27 (7)
T1160.048[a]	2.817 (4)	2.757 (13)	0.979 (5)	18.94 (8)
T1160.051[a]	2.817 (3)	2.742 (8)	0.973 (3)	18.85 (5)
T1160.052[a]	2.812 (5)	2.746 (19)	0.976 (7)	18.80 (12)
T1160.055[a]	2.808 (6)	2.747 (23)	0.978 (8)	18.76 (14)
T1160.056[a]	2.804 (3)	2.745 (12)	0.979 (4)	18.69 (8)
T1160.059[a]	2.801 (6)	2.740 (21)	0.978 (8)	18.61 (13)
T1160.060[a]	2.806 (3)	2.727 (9)	0.972 (3)	18.60 (6)
T1160.085[a]	2.873 (1)	2.788 (5)	0.971 (2)	19.93 (4)

[a]WC in pattern from interaction with MAP assembly component and not an experimental phase.

4.1.3 Phase Transitions in WO_2

At ambient conditions, WO_2 exists as a monoclinic phase with space group $P2_1/c$ (Bolzan et al. 1995). Under compression at room temperature, a structural transformation is evident beginning at approximately 25 GPa to an orthorhombic structure. These two structures coexist for at least 20 GPa, with the monoclinic mostly disappearing above approximately 45 GPa. This phase transition is evidenced by the

gradual disappearance of x-ray diffraction peaks in the monoclinic phase and the appearance of other peaks presumed to be orthorhombic peaks. Identification of the higher pressure phase as orthorhombic is based on three premises: 1) a high-P orthorhombic phase in space group *Pnma* was synthesized at 1170K and 8 GPa by Sundberg et al. (1994), which they termed the hp-WO_2 modification; 2) a computational study using plane wave pseudopotential calculations proposed that at high pressures WO_2 could exist in the cottunite structure, which is orthorhombic also in space group *Pnma* (Dewhurst and Lowther 2001); and 3) x-ray diffraction patterns from the present study exhibited distributions of peaks suggestive of an orthorhombic structure. However, indexing of the room temperature x-ray diffraction data on the orthorhombic phase was not robust when referenced to either the Sundberg et al.(1994) or Dewhurst and Lowther (2001) high pressure structures. Probable explanations of the difficulty in indexing the high pressure data include: 1) an incomplete phase transition, with a mixture of structural states; 2) structural distortions related to #1and due to increasingly non-hydrostatic conditions; and 3) a sluggish transition.

High pressure x-ray diffraction experiments in a resistively-heated DAC conducted up to approximately 42 GPa and at temperatures up to approximately 715 K also showed the coexistence of the monoclinic ($P2_1/c$) and orthorhombic (*Pnma*) structures above 30 GPa. In the highest pressure, high-temperature data, the monoclinic and orthorhombic phases appeared to have roughly equal contributions to the x-ray diffraction patterns as gauged by relative intensities.

High temperature experiments conducted for the present study using LHDAC and MAP showed markedly contrasting results compared to both the room-temperature

compression and lower-temperature (<715 K) resistively-heated DAC experiments. For the multi anvil and the lowest-pressure LHDAC experiments (<25 GPa), WO_2 was identified with the *Pnma* structure of Sundberg et al. (1994). One or two diffraction peaks in the patterns from these experiments could possibly be attributed to the $P2_1/c$ monoclinic structure, but the relative intensities of these peaks were low. The *Pnma* structure was observed at a pressure of approximately 5 GPa and 300 K in the MAP experiments. This suggests that the $P2_1/c$ to *Pnma* structural transition has a kinetic barrier, and the *Pnma* structure is stable to low pressure and temperature conditions. This is also supported by the fact that Sundberg et al. (1994) recovered their hp-WO_2 phase to ambient conditions for x-ray diffraction analysis and crystal structure refinement. The phase boundary for the $P2_1/c$ to *Pnma* transition is placed at 4 GPa.

In the 40 GPa data from the LHDAC experiments, the *WO_2-hpm* phase was identified replacing the *Pnma* structure present in the 20 GPa data. Some of the peaks for *WO_2-hpm* were present in the 50 GPa data, though other peaks in these data were not indexable as *WO_2-hpm* and represent a coexisting phase assumed to be another tungsten oxide. The abundance of W relative to the oxide decreased in this pressure range, suggesting that the second, non-*WO_2-hpm*, oxide phase was the result of the reduction of WO_2 and oxidation of W to form a lower valence tungsten oxide, perhaps W_2O_3 (W^{3+}). The proposed formation of a second oxide is also supported by the stable relative intensity of the WC peaks across the high pressure data sets. A continued increase in WC abundance would be the other obvious explanation of the reduced W peak intensities. In the 60 GPa data, the *WO_2-hpm* may have been present though work on the EOS brought this identification into question. The intensities of W peaks relative

to tungsten oxide peaks decreased further in the 60 GPa data. This suggests that the reaction observed in the 50 GPa data proceeded further and perhaps to equilibrium. Plots of the highest temperature spectra from the 20, 40, 50 and 60 GPa data are shown in Figure 34, illustrating the changes in the phase complement in the LHDAC experiments. The diffraction spectra show the change in structure observed for WO_2 from *Pnma* to *P2/m*, the decrease in W relative peak intensities, and the appearance of WC peaks at 40 GPa. The *Pnma* structure was identified in both 29 GPa and 39 GPa diffraction patterns at 300 K, but was entirely absent in the high temperature data in the 40 GPa range. This places the possible phase boundary for *Pnma* to *P2/m* over a range of ~23 to 39 GPa. Lack of high temperature data in this pressure range leads to the simplest choice for the phase boundary at approximately 32 GPa. A phase diagram for WO_2 is shown in Figure 35.

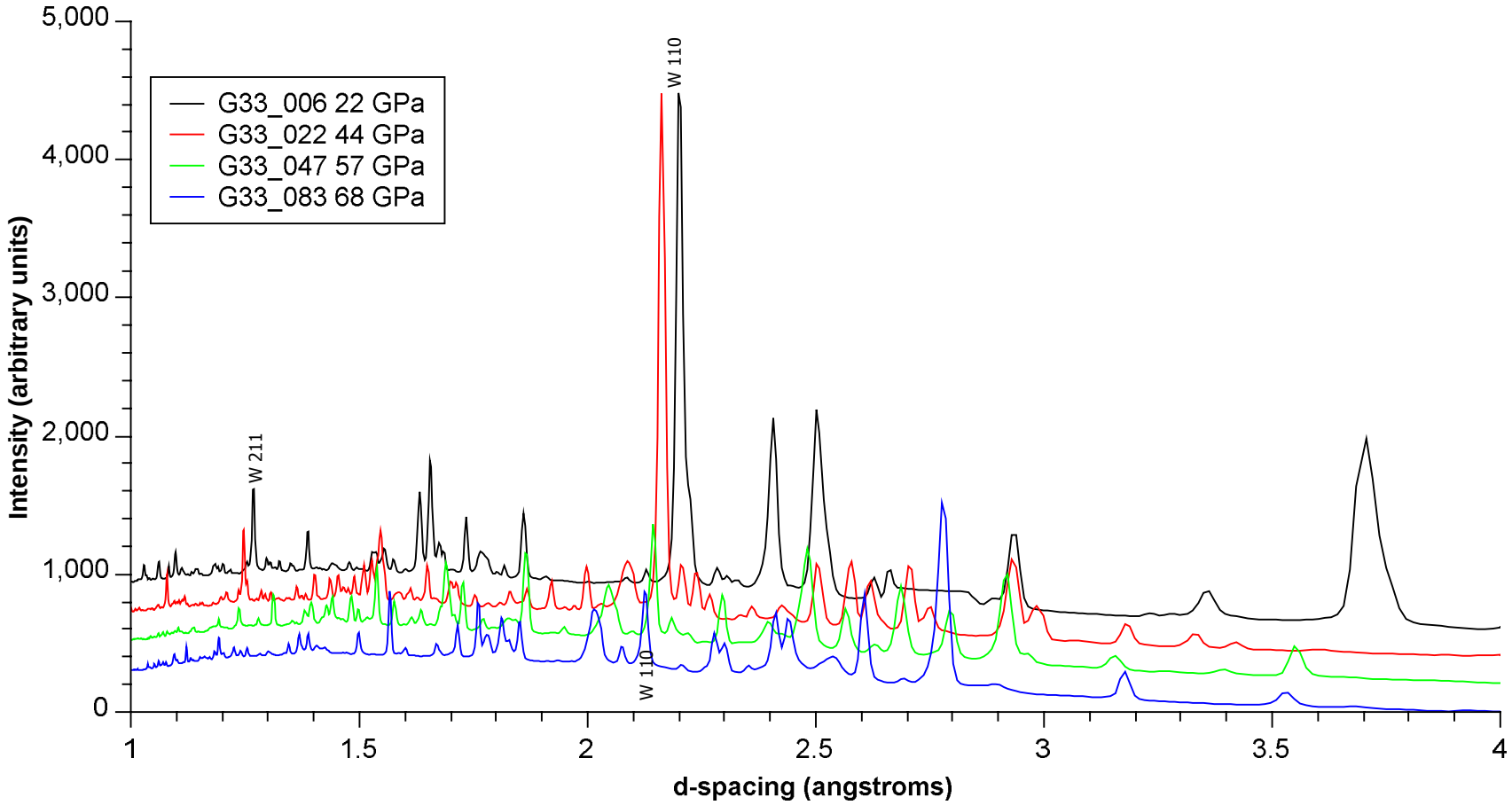

Figure 34. X-ray diffraction spectra from highest temperature pattern at each pressure range. The *d-spacing* offset between the spectra is due to compression. The 110 and 211 peaks for W are labeled to show the change in relative intensity of W to the other phases in the two highest pressure data sets.

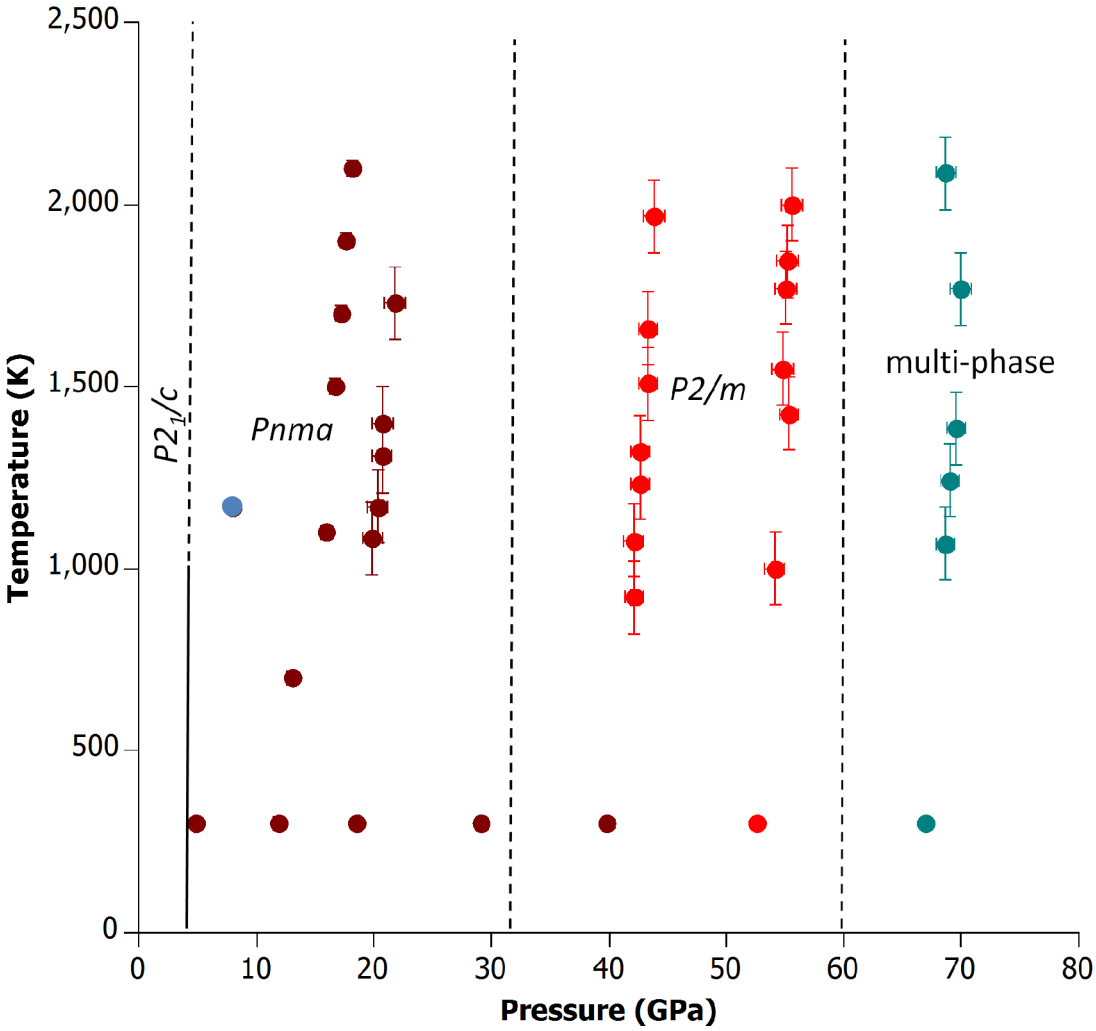

Figure 35. Phase diagram for WO_2. Space group of phases are indicated in italics. The blue symbol indicates the pressure and temperature synthesis conditions of the high pressure orthorhombic phase (*Pnma*) described by Sundberg et al. (1994). At pressures higher than 60 GPa, multiple tungsten oxide phases were present.

4.2 Equations of State

Thermal equations of state (EOS) describe the relationships among pressure, temperature, and volume for a given phase. To calculate the WWO fO_2 buffer, a thermal EOS for each of the observed WO_2 phases and for W were needed. Details pertinent to the individual phases are discussed in the following sections. The general form of the EOS used was $P = P_{300} + P_{th}$, where P_{300} is the ambient-temperature

pressure component and P_{th} is the thermal pressure component. The room-temperature pressure component is represented by a 3rd order Birch-Murnaghan EOS and is a function of volume only: $P_{300} = 3K_0 f(1+2f)^{5/2}(1+1.5(K_0^{'}-4)f)$, where K_0 is the bulk modulus, K_0' is bulk modulus pressure derivative, and f is the Eulerian strain and equals $0.5\left((V/V_0)^{-2/3}-1\right)$ with V = volume and V_0 = zero-pressure volume. The thermal pressure component is a linear function of temperature only, except for W which is described in a later section. The form of P_{th} is A*ΔT, where A is the thermal coefficient and ΔT is the difference between the temperature at which the pressure is being calculated and 300 K. The coefficient A is equal to the partial derivative $\left(\frac{\partial P}{\partial T}\right)_V = \alpha K_T$. All EOS were fitted using a Solver-based approach as described above for lattice parameter determinations (Table 11).

Table 11. Fit parameters for P-V-T equations of state.

Phase	*Parameter*		*+/-*	*%err*	*Fit uncertainty (r.m.s.)*
W	A_0	0.00417	0.000015	0.4	0.04
	A_1	-4.94E-06	3.59E-07	-7.3	
	K_0	306	0.19	0.1	
	K_0'	4.06	0.01	0.2	
WO_2 ($P2_1/c$)	*A*	0.00506	0.00101	20	0.86
	K_0	190	9	5.0	
	K_0'	4.24	0.75	18	
WO_2 (Pnma)	*A*	0.00393	0.000328	8.3	0.66
	K_0	224	11	4.8	
	K_0'	4.34	0.84	19	
WO_2 (P2/m)	*A*	0.00467	0.000150	3.2	0.28
	V_0	18.09	0.03	0.2	
	K_0	300	5.4	1.8	
	K_0'	4	fixed		

4.2.1 Pressure Calibration

Initial EOS fits for W and for the *Pnma* and *P2/m* phases of WO_2 resulted in undesirable levels of misfit, in which the sum of squared residuals had values of exceeding 60, whereas values of less than ten and ideally less than one were desirable. Systematic curvature in the plots of the misfit data suggested that the pressure calibration was causing or contributing to the high levels of misfit. The LHDAC experiments included NaCl as the pressure calibrant (Decker 1971; Fei 2007), and the MAP experiments used MgO (Speziale 2001). The validity of the NaCl and MgO peak indexing was verified, and finding no issues with pressure calibrant peak indexing it was decided to use W as the pressure calibrant. Experimental pressures were calculated based on the calculated W lattice parameter for each data point using the thermal EOS of Dorogokupets and Oganov (2007). Fit qualities improved dramatically after changing the pressure calibrant from NaCl or MgO to W. The cause of the poorer EOS fits using NaCl and MgO versus W for pressure calibration remains undetermined.

4.2.1.1 $P2_1/c$ phase

The EOS for the $P2_1/c$ phase was based on data collected at temperatures ranging from 300 to 715 K and pressures ranging from approximately 2 to 42 GPa. As discussed in the previous section, this phase appears to be stable below some threshold temperature, estimated as 1000 K. Therefore, it is reasonable to calculate an EOS across the pressure range of these experiments, even though its pressure range for calculation of the fO_2 buffer is significantly more limited. Fitted parameters were the isothermal bulk modulus, the thermal coefficient, and the bulk modulus first pressure derivative. See Figure 36 for a plot of the WO_2 EOS.

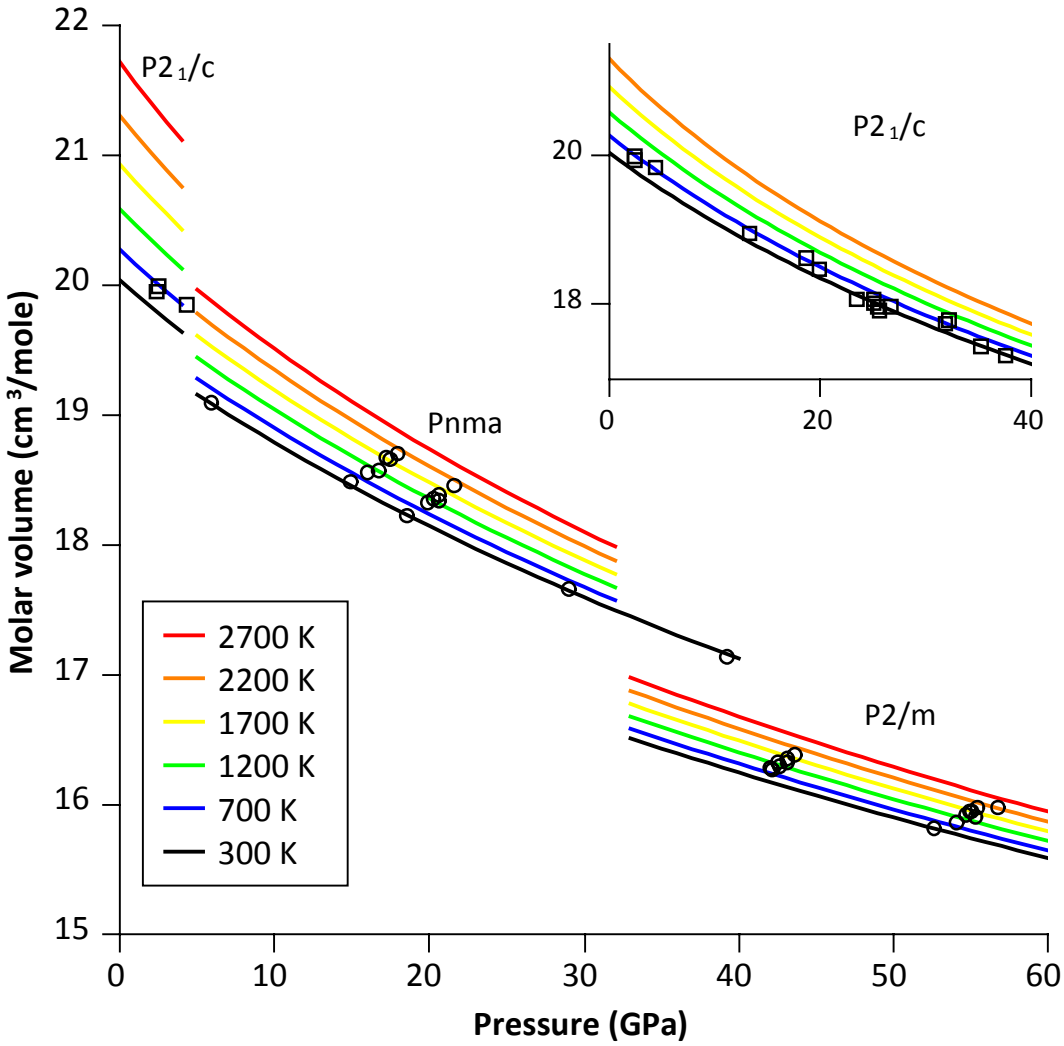

Figure 36. PVT EOS for WO_2 plotted along isotherms as a function of pressure. Each phase is plotted for the pressure ranges as shown in Figure 35. The inset in the upper right is the *$P2_1/c$* phase EOS plotted up to approximately 40 GPa, which exceeds the pressure range shown in Figure 35, because the *$P2_1/c$* WO_2 phase was stable up to approximately 40 GPa at temperatures up to approximately 700 K.

4.2.1.2 Pnma phase

The EOS for the Pnma phase was based on data from MAP and DAC experiments ranging 300 to 2100 K and 6 to 39 GPa. High temperature data extend from approximately 12 to 24 GPa. Data points at ambient temperature above 24 GPa were collected during compression of the diamond cell prior to the 40 GPa heating cycle, and

the data point at 6 GPa was collected at the minimum experimental press force in the multi anvil press. Fitted parameters were the isothermal bulk modulus, the thermal coefficient, and the bulk modulus pressure derivative.

4.2.1.3 P2/m phase

For P2/m, fitted parameters were the bulk modulus, thermal term, and zero-pressure volumes. The zero-pressure volume had to be fitted since it was an unknown. Initial fit qualities were poor, including the inability to constrain K' as a free parameter. Adjusting K' to various fixed values above and below 4 resulted in increasing and decreasing parameter uncertainties, respectively. At K'=2.5, a zero pressure volume V_0 = 18.6 was a reasonable estimate, but the K' was not justified based the pressure range of the data. Examination of a P–V plot of all P2/m data showed that the 60 GPa set volumes were noticeably lower than between the 40 and 50 GPa data suggesting that the phase being modeled as WO_2-hpm may have been misidentified at this pressure. Removing the 60 GPa data from the fit resulted in greatly improved fit to the 40 and 50 GPa data, with root-mean-squared error of approximately 0.2. With K' as a free parameter in the fit, a value of 4 was determined. Since this indicated that the bulk modulus was linear with pressure, K' was fixed at 4 to improve the uncertainties on the other parameters.

4.2.1.4 Tungsten

As discussed above, a thermal EOS was needed for calculation of the WWO buffer. The Dorogokupets and Oganov (2007) EOS could have been used directly in the buffer calculation, but it has more a complex form than those developed here for WO_2.

For coding simplicity, it was thought best to have all EOS of the same form. Therefore, the W data were fitted with the experimental pressures calculated by Dorogokupets and Oganov EOS. This amounted to refitting of the Dorogokupets and Oganov EOS into the simplified $P_{total} = P_{300} + P_{thermal}$ EOS form chosen for the present study. The resulting bulk modulus and pressure derivative were 308 and 3.99, respectively, which compared well with the values 306 and 4.17 from Dorogokupets and Oganov (2007). See plot of W EOS in Figure 37.

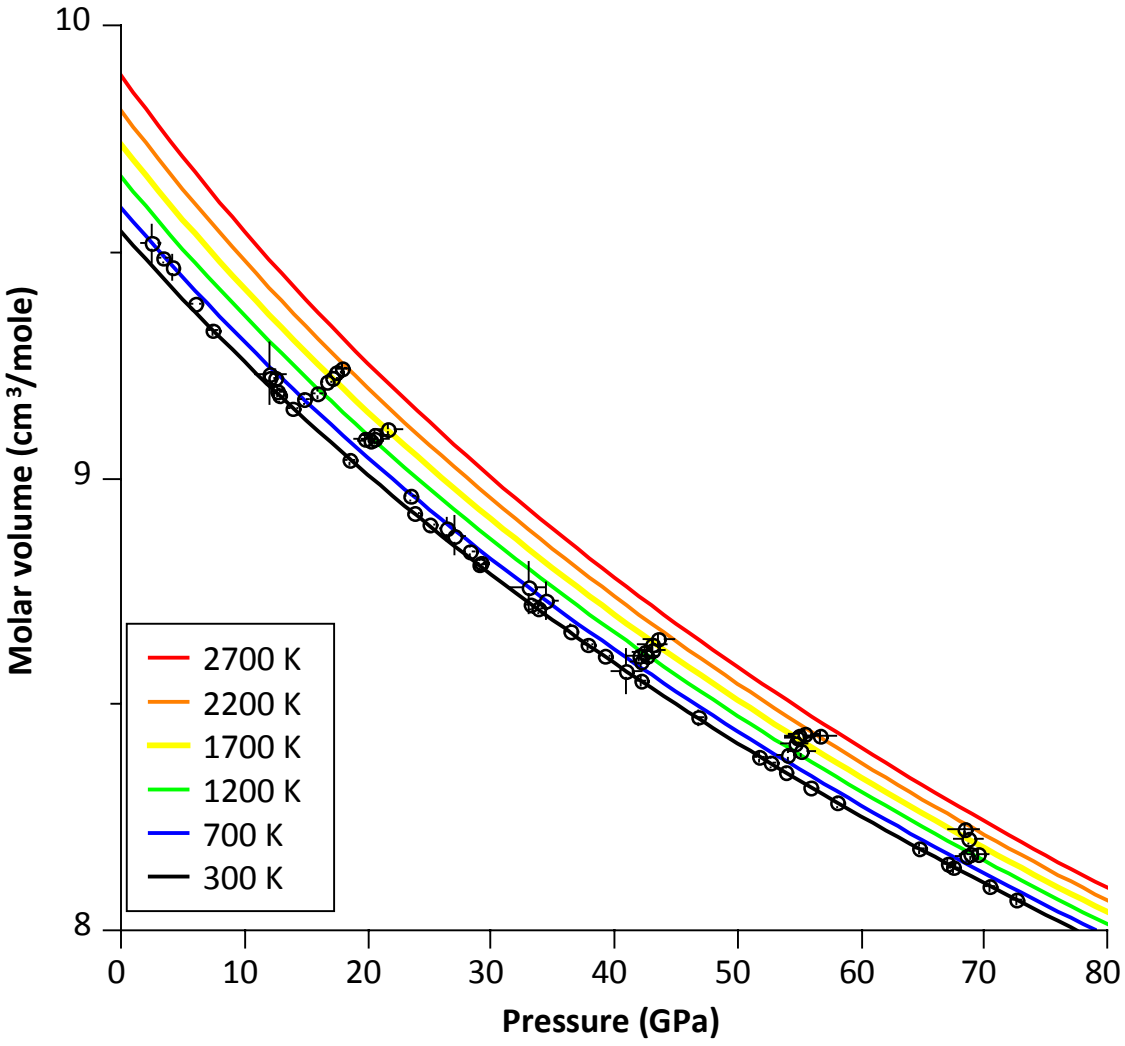

Figure 37. PVT EOS for W plotted along isotherms as a function of pressure.

4.3 The W-WO_2 Oxygen Fugacity Buffer (WWO)

With equations of state for both W and WO_2, a 1-bar fO_2 buffer can be extended to high pressures. This allows for calculating the fO_2 at any P or T conditions. Following Campbell et al. (2009), this is represented in brief by the following. Rearrange equation (3) such that

$$\ln f(O_2) = 2\Delta G_{WWO} / xRT \qquad (6)$$

and given that $dG = -SdT + VdP$, along an isotherm $dT = 0$, so that

$$\Delta G_{WWO} = \int_{P=1bar}^{P} \Delta V dP + \Delta G_0 \qquad (7)$$

As can be seen in (7), the pressure dependence is related to the volume difference (ΔV) between W and WO_2. Combining (6) and (7) gives the expression below that is the difference between the WWO buffer at some P and T and at P = 1 bar:

$$\ln f(O_2) - \ln f(O_2)_{1bar} = 2/xRT \int_{P=1bar}^{P} \Delta V dP \qquad (8)$$

What is needed to solve the integral in (8) is the difference in volume between the oxide and metal as a function of pressure, but the individual equations of state give pressure as a function of volume. The approach taken here is to invert the equation of states for W and WO_2 to determine ΔV at discrete pressures along isotherms. Using these ΔV values, (8) can be integrated to generate a matrix of fO_2 values over a range of pressures and temperatures. The inversion was accomplished using an iterative approach where the input volume to the EOS was varied at fixed pressures and the misfit was minimized between the fixed and calculated pressures. This algorithm was coded in Scilab along with other code to calculate the fO_2 buffer.

The WWO buffer was calculated over a pressure range of 1-bar to 100 GPa in 1 GPa increments and over a temperature range of 200 to 3000 K in 100 K increments. The calculation proceeded as follows: 1) molar volumes for all phases were calculated at each P-T point in 101x25 element matrices; 2) another matrix was generated that contained the delta-V values between WO_2 and W; 3) the 1-bar fO_2 W-WO_2 buffer was calculated in the temperature range of interest based on O'Neill and Pownceby (1993); and 4) the fO_2 was calculated along isotherms using equation (8) rearranged with ln $f(O_2)_{1bar}$ on the right-hand side. To address the issue of three WO_2 phases, code was included to switch to the appropriate EOS at the pressures of the assigned phase boundaries. This is justified thermodynamically because at equilibrium and along a phase boundary the chemical potentials and the oxygen fugacities of the phases are equal. Therefore, the integration in equation (8) simply proceeded across the phase boundaries. The WWO buffer is plotted versus inverse temperature and pressure in Figure 38.

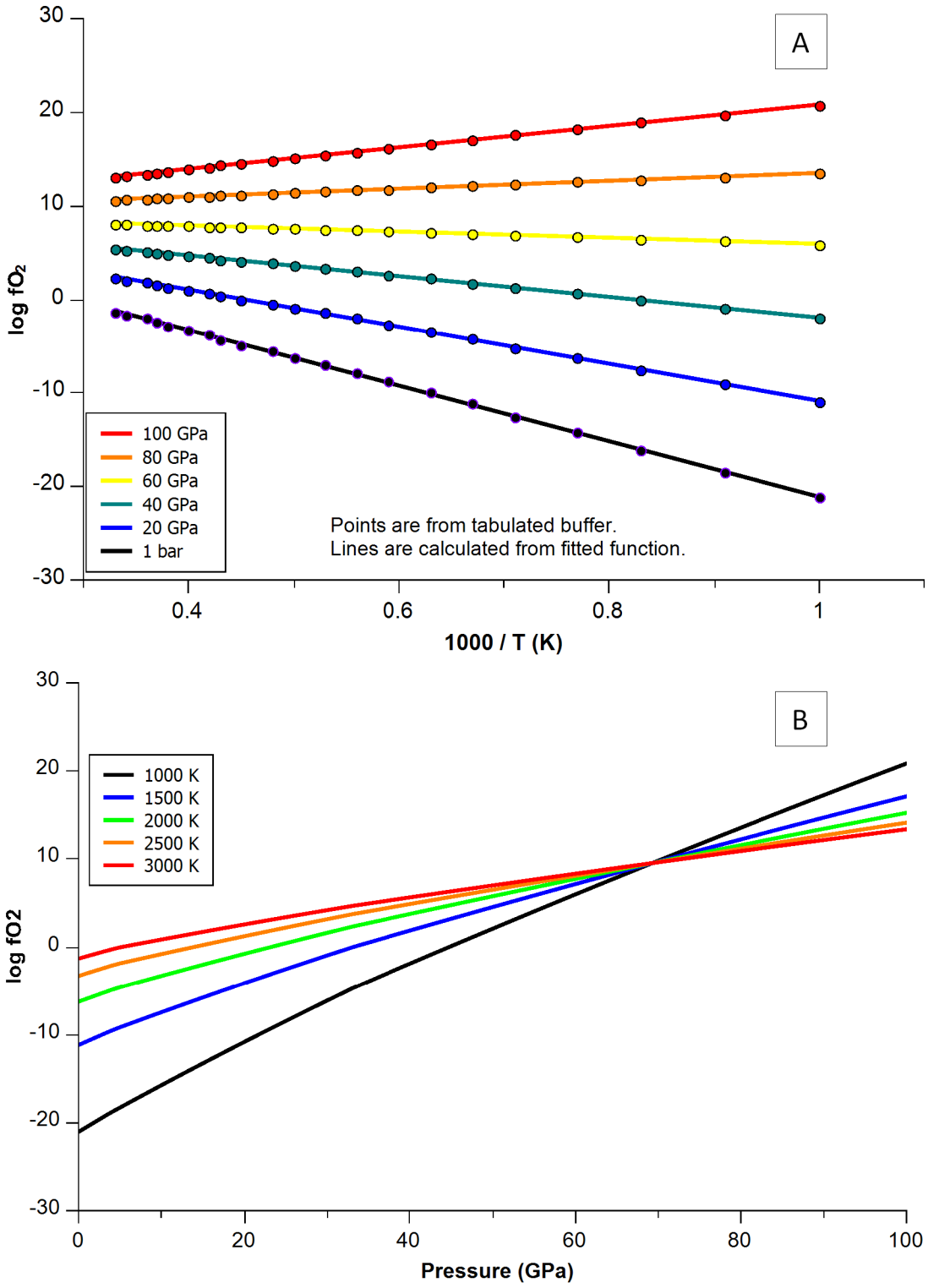

Figure 38. Log of the absolute fO_2 of the WWO buffer plotted as a function of inverse temperature (A) and pressure (B).

4.3.1 Polynomial Expression of fO_2

The calculation method described above produced matrices of fO_2 values with isothermal rows and isobaric columns. These data are adequate for plotting curves, but to allow calculation of the fO_2 of the WWO buffer at any P-T condition, the tabular (matrix) data were fitted to polynomial expressions. Because of the crystal-structural phase transitions in WO_2, separate polynomials were fitted for the pressure range of stability for each phase; $P2_1/c$ stability 0 - 4 GPa, Pnma 5 - 32 GPa, and P2/m 33 - 100 GPa. The general polynomial form used was:

$\log fO_2 = \left(a_0 + a_1P + a_2P^2 + a_3P^3\right) + \left(b_0 + b_1P + b_2P^2 + b_3P^3\right)/T$. To aid in easier application of the WWO buffer in terms of using a single expression to calculate fO_2, an additional polynomial was fitted across the Pnma-P2/m phase boundary encompassing the entire pressure range of 5 to 100 GPa. While fO_2 values calculated in the region of the phase boundary are not strictly correct, the difference between the fitted, multi-phase curve and the two individual curves is small. This is especially true given the uncertainty of the position of the phase boundary, i.e. the differences in calculated fO_2 depending on the phase boundary position are greater than those induced by the two-phase fit.

Parameters for each WO_2 phase and r.m.s. of the misfits are shown in Table 12. All fits were made over the pressure ranges given above and from 1000 - 3000 K. Distribution of misfits was poorer at minimum temperatures less than 1000 K due to significant curvature of the buffer at lower temperatures. Given the likely temperature range of the WWO buffer in application to both experimental and natural systems, this is a reasonable base of temperature for the fits.

Table 12. Parameters of polynomial fits of tabulated fO_2 values for *P2₁/c*, *Pnma*, and *P2/m* WO_2 phases in high pressure W-WO_2 oxygen fugacity buffer. Pnma-P2/m is for fit across phase boundary. The A parameters have only pressure dependence, and the B parameters have pressure and temperature dependences, such that $\log fO_2|_{WWO} = (A_0 + A_1P + ... A_NP^N) + (B_0 + B_1P + ... B_NP^N)/T$.

WO_2 phase		*Parameters*			Fit uncertainty (r.m.s.)
P2₁/c	A_0	8.6162	B_0	-29727	0.041
	A_1	0.030824	B_1	527.1	
	A_2	-0.00054			
Pnma	A_0	8.6919	B_0	-29665	0.038
	A_1	0.012305	B_1	517.47	
	A_2	-0.00015	B_2	-1.2519	
	A_3	1.09E-06	B_3	0.005817	
P2/m	A_0	8.7572	B_0	-27642	0.036
	A_1	0.007753	B_1	437.72	
	A_2	-3.5E-05	B_2	-0.55712	
	A_3	9.02E-08	B_3	0.001008	
Pnma-P2/m	A_0	8.6926	B_0	-29838	0.048
	A_1	0.01222	B_1	546.48	
	A_2	-0.00015	B_2	-2.2413	
	A_3	1.24E-06	B_3	0.009264	
	A_4	-4.3E-09			

The form of the polynomial was determined by following procedure. Beginning with a slope-intercept form, $\log fO_2 = A + B/T$, the tabulated fO_2 data were analyzed as isobars, and *A* and *B* values were determined for each isobar. These A and B values were fitted to polynomials as functions of pressure. The order of the polynomials was varied to maximize the fit qualities, resulting in third order polynomials in A and B, except for $P2_1/c$ which only required a second and first order expressions, and a fifth order expression for the two-phase Pnma-P2/m fit.

4.3.2 Relationship to Iron-wustite

The difference between the WWO and IW (Campbell et al., 2009) buffers is shown in Figure 39. At pressures lower than 40 GPa, the WWO buffer is at a higher fO_2 than the IW buffer. The magnitude of this difference decreases at higher pressures. The

significance of the WWO buffer at higher fO_2 than IW is that it predicts siderophile behavior for W. This is because the fO_2 is the chemical potential of oxygen, so if the W-WO_2 equilibrium is at a higher chemical potential relative to Fe-FeO, and hence has a higher Gibbs free energy then the W-WO_2 equilibrium will tend to shift toward the left side of the equilibrium in equation (2) increasing the stability of W metal.

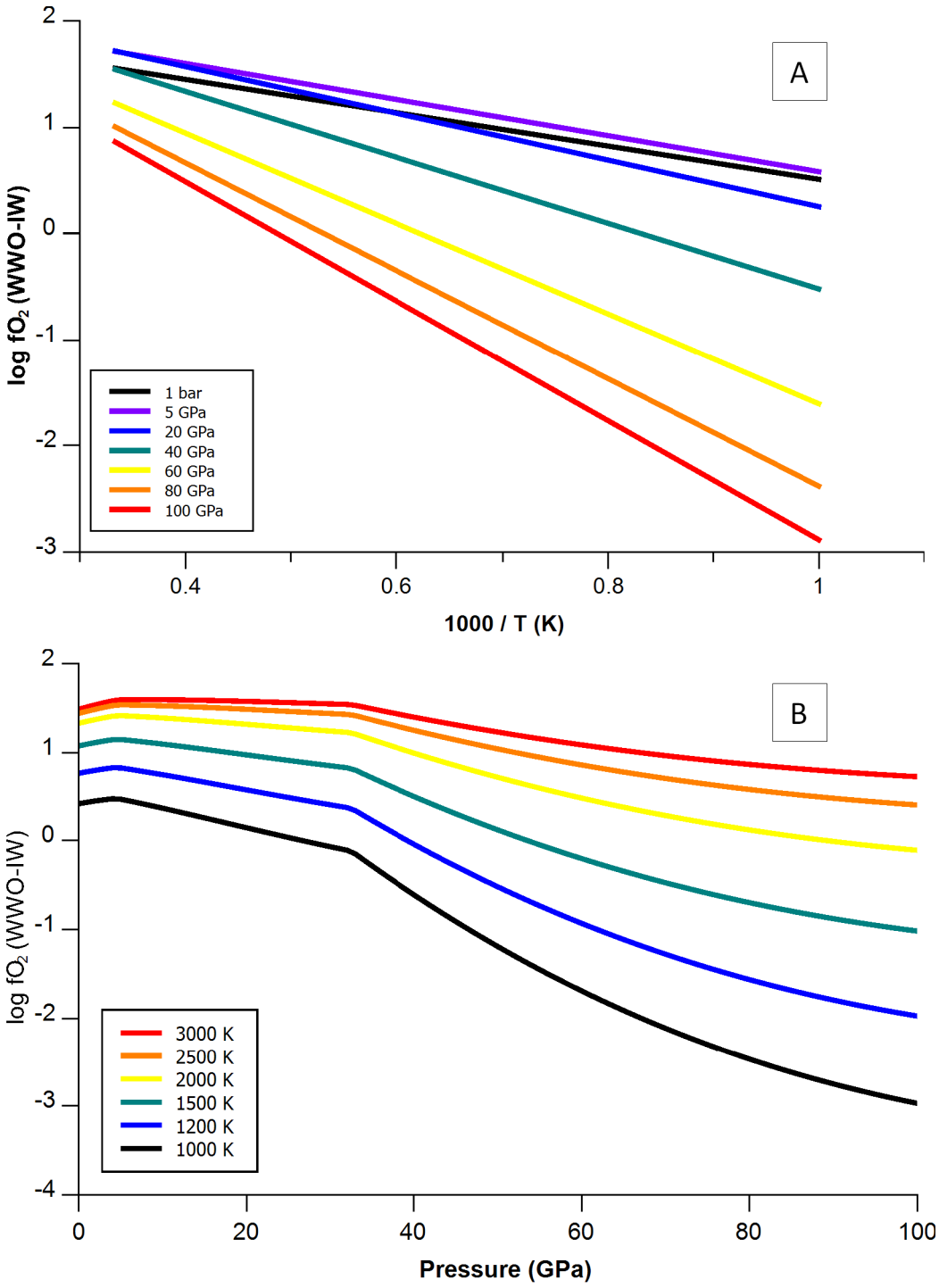

Figure 39. Difference between WWO and IW buffers plotted versus inverse temperature and pressure. IW calculated using Fe-FeO buffer of Campbell et al. (2009).

4.3.3 Application to W Metal/silicate Partitioning

Following Campbell et al. (2009), the log of the exchange coefficient K_D for W as a function of the difference between the W-WO_2 and IW fO_2 buffers and the log of the ratio of activity coefficients is

$$logK_D = \frac{x}{2}(logfO_2^{WWO} - logfO_2^{IW}) + log\left[\left(\gamma_{WO_x}^{sil}/\gamma_W^{met}\right)/\left(\gamma_{FeO}^{sil}/\gamma_{Fe}^{met}\right)^x\right]$$

and after subtracting the WWO-IW term from both sides gives

$$logK_D - \frac{x}{2}(logfO_2^{WWO} - logfO_2^{IW}) = log\left[\left(\gamma_{WO_x}^{sil}/\gamma_W^{met}\right)/\left(\gamma_{FeO}^{sil}/\gamma_{Fe}^{met}\right)^x\right]$$

Using the measured log K_D values from metal/silicate experiments and the calculated differences between the WWO and IW buffers at the P-T conditions of those experiments to calculate the left hand side, the right hand side can be rearranged as a sum of activity coefficients $Z = log\gamma_{WO_x}^{sil} - log\gamma_W^{met} - xlog\gamma_{FeO}^{sil} + log\gamma_{Fe}^{met}$. This is the molar excess Gibbs energy of mixing of the Fe-W exchange reaction $G_{xs} = RT\sum ln\gamma_i$. Oxygen fugacity has a strong effect on metal-silicate partitioning and the fO_2 is addressed by the difference in the WWO and IW buffers including any non-linear dependence in pressure. Assuming that the remainder of the effects on W metal/silicate partitioning are linear, the excess Gibbs energy of mixing can be modeled to the first order with compositional, pressure and temperature dependencies $G_{xs} = RT\sum ln\gamma_i = G_0 + \sum X_i + V_{xs}P - S_{xs}T$ which expressed in terms of Z given above is $Z = \left(Z_0 + \sum_{i,j} z_i^j X_i^j + V_{xs}P - S_{xs}T\right)/RT = (Z_0/RT) + \left(\sum_{i,j} z_i^j X_i^j/RT\right) + (V_{xs}/RT) - (S_{xs}/T)$, where *i* is a component in phase *j* with mole fraction *X*, and V_{xs} and S_{xs} are the excess volume and entropy of mixing, respectively.

Using the phase boundary pressure of 32 GPa (Figure 35) for the *Pnma-P2/m* phase transition, the excess Gibbs energy of mixing was fitted for experimental data from this study and from the literature at pressures ≥ 5 GPa. The phase components modeled as contributing to G_{xs} were SiO_2, Al_2O_3, and CaO in the silicate melt, and C, S, and W in the metallic melt. Inclusion of MgO in the fit resulted in an uncertainty on this parameter that exceeded the value of the parameter indicating that it was not statistically significant, and suggesting that MgO did significantly contribute to G_{xs}. The results of this fit for Z are shown in Table 13.

Table 13. Fit parameter for the excess Gibbs energy of mixing in the W-WO_2 buffer-based expression of the Fe-W exchange coefficient.

Parameter	*Value*	*+/-*	*%err*	*Fit uncertainty (r.m.s.)*
Z_0	-39810	8582	22%	0.19
Z_{SiO_2}	126400	13300	11%	
$Z_{Al_2O_3}$	112300	20920	19%	
Z_{CaO}	174900	23880	14%	
Z_C	-16680	5785	35%	
Z_S	-88820	13580	15%	
Z_W	52810	16580	31%	
V_{XS}	-702.1	144.2	21%	
S_{XS}	-10.53	3.239	31%	

Having fitted the excess Gibbs energy of mixing, an expression of W metal-silicate partitioning as an Fe-W exchange partition coefficient can be made in terms of the difference between the WWO and IW fO_2 buffers and the regressed excess Gibbs energy

$$\log K_D = \frac{x}{2}(logfO_2^{WWO} - logfO_2^{IW}) + \left[\left(\frac{Z_0}{RT}\right) + \left(\frac{\sum_{i,j} z_i^j x_i^j}{RT}\right) + \left(\frac{V_{xs}}{RT}\right) - \left(\frac{S_{xs}}{RT}\right)\right] \quad (9)$$

Equation (9) will be referred to as R4, for consistency with the naming of the linear regressions presented in Chapter 3. The metal/silicate partitioning of W using R4 was calculated along the peridotite liquidus and is shown in Figure 40. Isothermal and

isobaric plots are shown in Figure 41. Regression R3 based on linear dependencies in all parameters is shown for comparison in Figures 40 and 41. The liquidus curves using R4 and R3 have generally the same trend, with R4 predicting a larger decrease in the siderophility of W with increasing pressure. Note the deflection of the R4 curve in the region of 30 GPa that is related to the *Pnma-P2/m* phase transition, which involves a volume decrease and an increase in the bulk modulus. The extent to which this phase change in the solid state is reflected in the liquid state is not clear, but generally solid state structural properties are reflected to some extent in the liquid state.

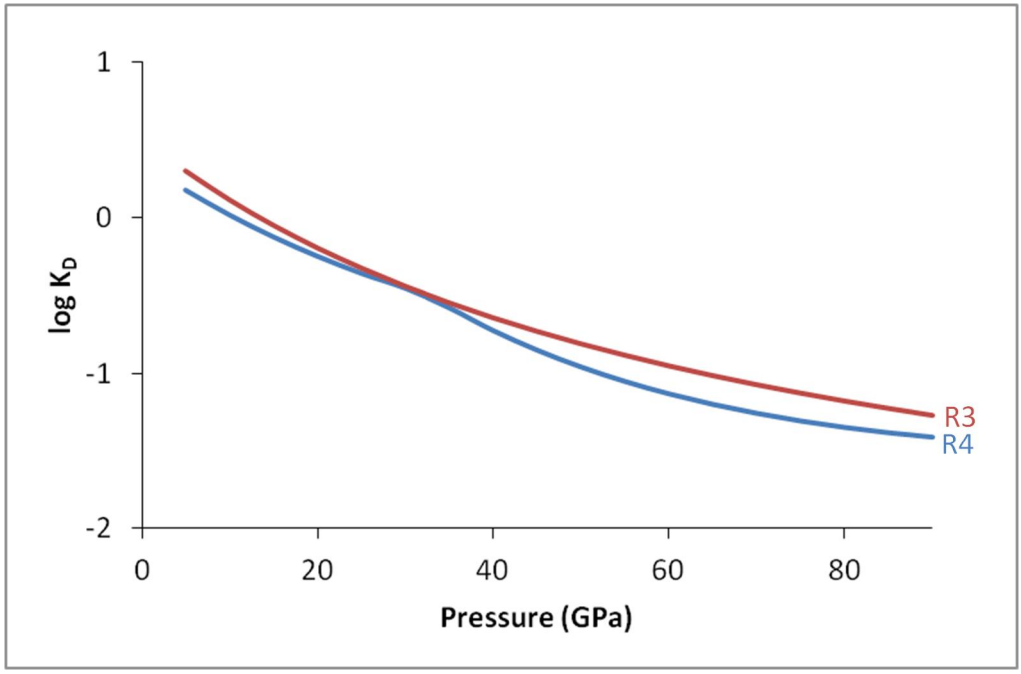

Figure 40. The predicted W metal/silicate partitioning in terms of the log of the Fe-W exchange coefficient calculated along the peridotite liquidus (Wade and Wood, 2005). Blue curve calculated using R4, using the WWO-IW buffer-based approach. Red curve calculated using linear regression R3 for comparison.

Looking at isotherms, log K_D is negatively correlated with pressure where the pressure effect is approximately 3 log units at 2000 K decreasing to approximately 1.5 log units at 3500 K. Along isobars, log K_D is positively correlated with temperature where the temperature effect is approximately 0.5 log units at 10 GPa, increasing to

approximately 3 log units at 60 GPa. Pressure and temperature have competing effects on the metal/silicate partitioning of W, but in the case along the peridotite liquidus, where both pressure and temperature vary, pressure exerts the greater effect.

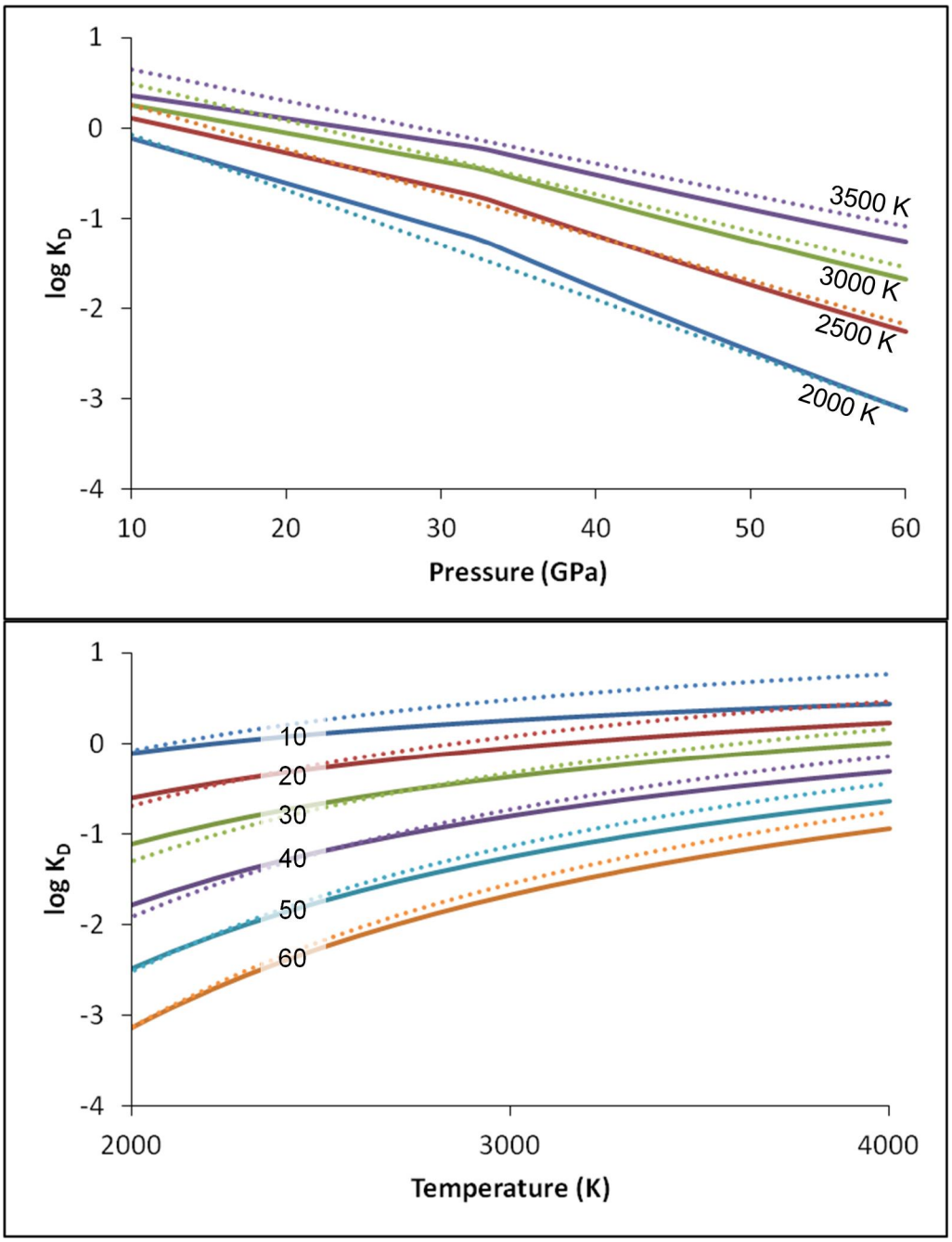

Figure 41. Isothermal and isobaric plots of the predicted W metal/silicate partitioning in terms of the log of the Fe-W exchange coefficient. Solid lines were calculated using R4, based on the WWO-IW buffer-based approach. Dotted lines were calculated from linear regression R3. Labels on isobaric plot are pressures in GPa.

5 Core Formation Modeling

As discussed previously regarding both literature data and the results of the present study, the combined effects of pressure, temperature, silicate and metal compositions, and fO_2 are often difficult to experimentally isolate. A common approach is to parameterize partitioning data sets to characterize these combined effects assuming linear dependencies in all variables. Notable examples of this are Wade and Wood (2005), Wood (2008), Cottrell et al. (2009), and Righter (2011). Following these I have parameterized my data along with literature data and these have been presented as regressions R1, R2, and R3. I have also approached modeling W metal/silicate partitioning from a difference perspective through the use of high pressure fO_2 buffers to capture the non-linear dependence in metal/silicate equilibria.

The utility of regressions, whether linear or non-linear, is that the resulting equations can be used as a predictive tool. Applying regressions determined in this study to the problem of core formation, I examine core-mantle equilibrium in a silicate magma ocean. As discussed in Chapter 1, assuming equilibrium between metal and silicate in an accreting Earth, partition coefficients can be calculated based on modern core and mantle abundances of W and other siderophile elements. Determining the pressure, temperature, fO_2, and melt compositional constraints necessary to produce these partition coefficients can provide insight into conditions present during and processes operating in early Earth history.

5.1 Modeling Approach

That the mantle of the Earth underwent multiple episodes of partial or complete melting has become widely accepted and is based both on physical and geochemical constraints. This molten state of the mantle referred to as a magma ocean is the prevailing paradigm in studies of core formation and it is in the context of a magma ocean that I model core formation in the Earth. The assembly of the Earth by accretion of progressively larger bodies via impacts is supported by dynamic models of solar system formation and the distribution of matter under the influence of gravity (Stevenson, 2008; O'Brien et al., 2006). The chemical composition of the Earth, especially the budget of the moderately and slightly siderophile elements, suggests conditions in the early Earth that are best explained by metal-silicate segregation at high pressure and temperature conditions (Righter, 2011; Siebert et al., 2011). The highly siderophile element abundances in the mantle are much greater than predicted by metal-silicate partitioning associated with core formation, and their mantle abundances are commonly attributed to the addition of a 'late veneer' of chondritic material to the Earth following core formation (Walter and Tronnes, 2004; Bottke et al., 2010; and Walker, 2009).

The simplest model of core formation in the Earth is based on the use of a single element, such as W, which I have characterized at high pressure and temperature conditions. Calculating the conditions where the modern core and mantle abundances of W are explained gives an estimate of the probable conditions of core formation. The use of other elements, however, which have different pressure, temperature, compositional, and oxygen fugacity dependencies provides a more robust solution that

can be considered a more likely indicator of core formation conditions. I will use W, Ni, Co, and Mo because they are all refractory elements and, therefore, their bulk Earth abundances relative to the source materials of the Earth are the least likely to have been affected by volatile loss in the high temperature conditions prevalent during Earth accretion.

Arguably the most important basis of these models is the target values represented by the calculated partition coefficients necessary to explain the modern core and mantle abundances. As discussed in the introduction of this writing, several values for the silicate Earth, or primitive mantle, abundance of W are available in the literature. The choice of element abundances, therefore, will significantly affect the model results. Furthermore, the uncertainties on element abundances in the Earth has the effect of widening or narrowing the possible constraints a given element can place on core formation conditions, depending on larger or smaller abundance uncertainties, respectively. For instance, McDonough and Sun (1995) estimate the silicate Earth abundance of W to be 29 ppb with a level of uncertainty of a factor of two. With this level of uncertainty, the possible pressure and temperature conditions predicted would be so wide as to be essentially useless in constraining core formation conditions. Wade and Wood (2005) listed the probable range of W partition coefficient values for core-mantle equilibration as 15 to 22, referencing the McDonough and Sun (1995) and McDonough (2003) mantle and core abundances, but gave no justification for this constraint relative to the reported factor of two uncertainty mentioned above. More recent estimates of W primitive mantle abundances are given by Lyubetskaya and Korenaga (2007), and Arevalo and McDonough (2008) with significantly lower

uncertainties; 12 ±3 ppb and 13 ±10 ppb, respectively. Clearly, use of either of these uncertainties for W would result in greater constraint on core formation conditions in the modeling scheme discussed here.

Since my modeling is in the context of a magma ocean, pressure and temperature conditions that are to be considered solutions should be at or above the liquidus of the early Earth mantle, which is assumed here to be of peridotite composition. This is an important point because more than one model of the peridotite liquidus are available in the literature. A commonly referenced model is that of Wade and Wood (2005), which calculates the liquidus temperature with a linear dependence in pressure. The Wade and Wood (2005) model was based on fitting the experimentally-derived data on peridotite melting given by Herzberg and Zhang (1996) and on estimated melting temperatures of pyrolite given by Zerr et al. (1998). More recently, Fiquet et al. (2010) have published a model of peridotite melting that was experimentally determined to 140 GPa, which is the modern Earth core-mantle boundary. This arguably a great improvement since the Zerr et al. (1998) data were collected to maximum pressure of approximately 60 GPa. The two models, however, describe vastly different liquidus temperatures, with the Fiquet et al. (2010) model consistently several hundred degrees higher than the Wade and Wood (2005) model. Furthermore, the Fiquet (2010) liquidus temperatures are approximately 1000 degrees above the solidus temperatures also reported in the same model. This is a larger separation of the liquidus and solidus than described by the Herzberg and Zhang (1996) data at lower pressures (<25 GPa), which show an approximately 100 degree region between liquidus and solidus. This discussion has great bearing on any magma ocean model and illustrates another potential uncertainty

on solution in such a model. This issue will be discussed in the following sections where model results are reported.

5.2 Models

Two approaches to modeling siderophile element abundances in a magma ocean have commonly been used. One restricts model solutions to P-T conditions along the peridotite liquidus. The other computes all possible P-T solutions over which the range of target core-mantle partition coefficients are matched.

In the magma ocean scenario, metal-silicate equilibration occurs between descending droplets of metal and surrounding liquid silicate. Final equilibration takes place at the base of the magma ocean (Rubie et al., 2003). Therefore, the P-T-X-fO_2 conditions at the base of the magma ocean exert final control over partitioning of elements between core and mantle. One way to visualize this is to simply plot the predicted partition coefficient along the peridotite liquidus, and compare this curve to the range of core-mantle equilibrium partition coefficient values with the region of intersection giving the range of P-T conditions of core-mantle equilibrium. Examples of this in the literature include Wade and Wood (2005), Corgne et al. (2008), and Cottrell et al. (2009). An alternative technique is to examine the problem in P-T space. Calculating the pressure and temperature conditions where values of the metal/silicate partition coefficient predicted by a regression are equal to the value of partition coefficient consistent with modern core and mantle abundances results in curves that represent possible conditions of core formation. Two curves are calculated representing the range of uncertainty on the modern core and mantle element compositions. This results in a domain of possible P-T conditions.

Combining domains for multiple elements gives further constraint and the intersection of these domains constitutes a solution space of probable core formation conditions for a simple, single-stage, core formation model. The final constraint is found by accepting only solutions above the peridotite liquidus. These two ways of analyzing the problem ultimately provide the same information, but the P-T space technique provides an arguably more visually appealing result.

I present three models here. They are based on regressions from this work and from literature (Kegler et al., 2008; Righter, 2011; Siebert et al., 2011). For W, Ni, and Co, the regressions are in terms of Fe-W, Fe-Ni, and Fe-Co exchange coefficients, and for Mo in terms of a partition coefficient. As discussed in Chapter 1, this has the advantage of being independent of fO_2 in terms of no explicit measure of fO_2 in the regression. In the type of model presented here, however, the target values representing core-mantle equilibration must be calculated with a partition coefficient for Fe. This is in effect choosing a fixed fO_2 since the Fe-FeO equilibrium exerts strong control over the fO_2. For the Siebert et al. (2011) Mo expression, an fO_2 of IW-2.3 was used. The solutions are in terms of pressure, temperature, silicate composition, and metal composition in the case of my regressions that include metal compositional terms. The first two models are meant to compare the W linear regression R3 with the buffer-based expression R4. The third model examines the influence of silicate melt composition on Ni and Co metal/silicate partitioning. Model parameters that were fixed included the silicate composition, metallic composition, and fO_2 as given above for Mo. The silicate composition was set as peridotite with the mole fractions $SiO_2 = 0.38$, $Al_2O_3 = 0.02$, $CaO = 0.03$, and $MgO = 0.51$, which gives and nbo/t = 2.75. The metallic composition

terms were set as the mole fractions of C = 0.008 and S = 0.03, which are consistent with the McDonough (2003) core composition model. The target partition coefficients were calculated based on the silicate Earth and core compositional models of McDonough and Sun (1995) and McDonough (2003), except for the W silicate Earth abundance which was taken from Lyubetskaya and Korenaga (2007). The abundances in core and mantle, and the calculated exchange and partition coefficients are shown in Table 14.

Table 14. Effective metal/silicate partition coefficients and Fe-element exchange coefficients for equilibrium core formation based on bulk silicate Earth and core abundances for W, Ni, Co, and Mo. Abundances are in ppm, except where shown as weight percents.

Element	*Core*	*Mantle*	*D*	*Range of D based on uncertainty of abundance*	K_D	*Range of K_D based on uncertainty of abundance*
W	0.5	0.012	43	33 - 53	0.22	0.17 - 0.28
Ni	52000	1960	27	24-30	1.97	1.77 - 2.17
Co	2500	105	24	22-26	1.75	1.58 - 1.93
Mo	5	0.05	100	60-140		
Fe	85.5%	6.26%	13.7			

As described above, these models are based on domains of pressure and temperature in which the partition coefficient or exchange coefficient calculated using the regression is equal to the coefficient representing bulk core/mantle equilibration. Since the regressions are in terms of the exchange or partition coefficient as functions of pressure and temperature and other parameters, two approaches to determining a P-T solution are appropriate. The first is to invert the regression by iteratively solving for pressures at some number of fixed temperature points or vice versa. The second is to algebraically rearrange the regression equation to give pressure as a function of everything else including the partition or exchange coefficient. In this way, the pressure

and temperature domain can be directly calculated in terms of the target core/mantle coefficient.

The regression equations from the literature sources are included here for reference.

Kegler et al. (2008)

$$logK_D^{Fe-Ni} = 0.26 + 3284\frac{1}{T} - 74\frac{P}{T}$$

$$logK_D^{Fe-Co} = 0.30 + 1405\frac{1}{T} - 40\frac{P}{T}$$

Righter (2011), where the Kegler et al. (2008) data were regressed using nbo/t

$$lnK_D^{Fe-Ni} = 0.41 - 0.18(nbo/t) + 9665\frac{1}{T} - 205\frac{P}{T}$$

$$lnK_D^{Fe-Co} = 0.86 - 0.07(nbo/t) + 3654\frac{1}{T} - 106\frac{P}{T}$$

Siebert et al. (2011)

$$logD_{Mo}^{met/sil} = 0.42 + 3117\frac{1}{T} - 97\frac{P}{T} - 0.27(nbo/t) - \frac{n}{2}log\left(\frac{X_{FeO}}{X_{Fe}}\right) - log\left(\frac{\gamma_{Mo}}{\gamma_{Fe}{}^{n/2}}\right)$$

The last term in the Siebert et al. (2011) expression was set to zero based on assuming ideality of mixing for Fe (Rauoult's Law) and for Mo (Henry's Law).

5.2.1 Model M1

This model is based on regression equation R3 of this study, the Ni and Co equations of Kegler et al. (2008), and the Mo equation of Siebert et al. (2011). All equations were algebraically rearranged to give pressure as a function of temperature, the target exchange or partition coefficient, and composition and fO_2 where applicable. Using the range of target exchange and partition coefficients (Table 14) as upper and

lower bounds, the pressures were calculated at these bounds for a range of temperatures from 2000 to 4000 K for each element. A region of overlap exists for W, Ni, and Co with a pressure range of 41-43 GPa and a temperature range of 2800-3200 K (Figure 42).

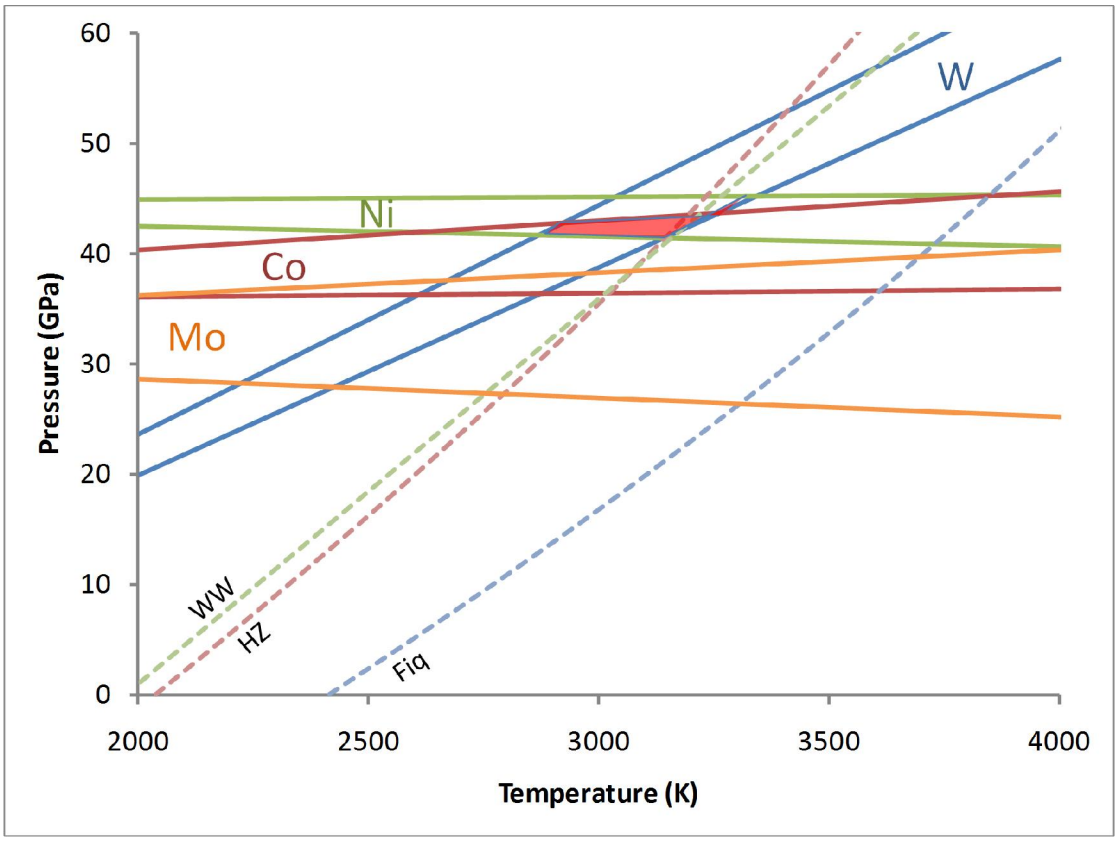

Figure 42. Model M1 for constraining equilibrium core formation conditions. The pairs of same-colored lines are bounds on the P-T conditions that satisfy the D value for the indicated element in the modern Earth (matches core/mantle abundances). The red polygon is a region where elements overlap, indicating the solution, 40-41 GPa and 2800-3200 K. Calculations for elements based on: W using R3 in this study; Ni and Co from Kegler et al. (2008); and Mo from Siebert et al. (2011). Multiple models of the peridotite liquidus are shown as dashed lines for reference: WW = Wade and Wood (2005); HZ = 2nd-order fit of Herzberg and Zhang (1996) and Zerr et al. (1998) data; and Fiq = Fiquet et al. (2010).

Only a small portion of this is above the liquidus, however which constrains the solution to 3200 K at approximately 42 GPa. This solution lies along the peridotite liquidus model of Wade and Wood (2005). The Mo domain lies at lower pressures and overlaps only with Co in the vicinity of the Wade and Wood (2005) liquidus, and

overlaps with Ni and Co at approximately 4000 K which is above the liquidus of Fiquet et al. (2010) by approximately 400 K.

5.2.2 Model M2

This model was based on the same equations from Kegler et al. (2008) and Siebert et al. (2011) for Ni, Co, and Mo, but uses the buffer-based equation R4 for W. The difference in calculating this model was related to R4, because it relies on the fO_2 buffers which are non-linear in pressure, R4 could not be simply rearranged algebraically to solve for pressure. Instead it had to be solved iteratively, which was accomplished using a combination of the Solver code in Microsoft Excel and the ColumnSolver function in the MacroBundle code of de Levie (2008). The ColumnSolver allows for setting up multiple targets in a column of a spreadsheet and then sequentially runs the Solver for each individual target. Using fixed intervals of temperature, the ColumnSolver varied pressure while matching calculated log KD values using R4 to the target value for W as listed in Table 14. The resulting solution space includes W, Ni, and Co overlapping in a pressure range of 42-45 GPa and a temperature range of 3000-3500 K (Figure 43). Constraining the solution to just above the peridotite liquidus the temperature is approximately 3200 K with a pressure range of approximately 42-44 GPa. Another solution just above the liquidus includes W, Co, and Mo at a pressure of approximately 38 GPa and temperature of approximately 3100 K. The total region of overlap for these elements extends from approximately 2700 to 3100 K and 36 to 38 GPa though nearly all of this region is below the peridotite liquidus.

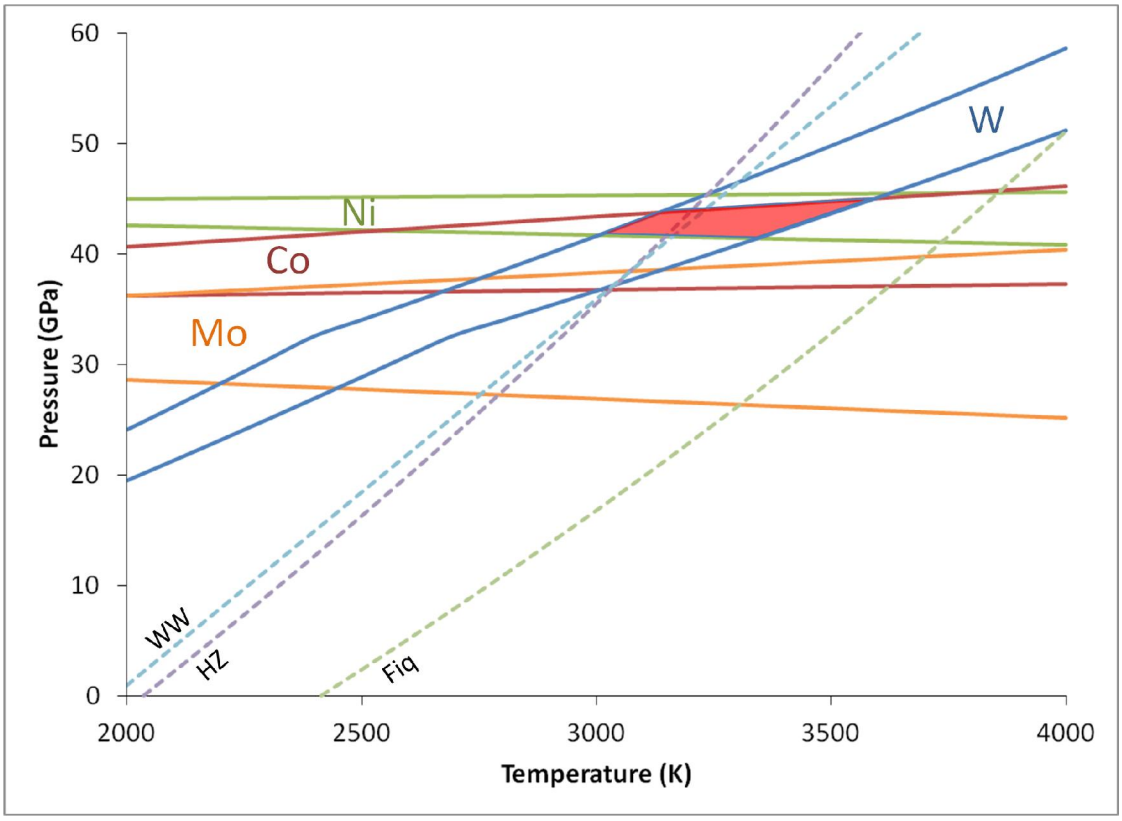

Figure 43. Model M2 for constraining equilibrium core formation conditions. The pairs of same-colored lines are bounds on the P-T conditions that satisfy the D value for the indicated element in the modern Earth (matches core/mantle abundances). The red polygon is a region where elements overlap, indicating the solution, 42-45 GPa and 3000-3500 K. Calculations for elements based on: W using R4 in this study: Ni and Co from Kegler et al. (2008); and Mo from Siebert et al. (2011). Multiple models of the peridotite liquidus are shown as dashed lines for reference: WW = Wade and Wood (2005); HZ = 2nd-order fit of Herzberg and Zhang (1996) and Zerr et al. (1998) data; and Fiq = Fiquet et al. (2010).

5.2.3 Model M3

This model uses equation R4 for W as in model M2 along with the same Mo equation of Siebert et al. (2011). The equations for Ni and Co, however, are from Righter (2011). Righter (2011) found a silicate compositional dependence for both Ni and Co that others have indicated is negligible (Kegler et al., 2008; Chabot et al., 2005). Righter (2011) regressed the Ni and Co metal/silicate partitioning data of Kegler et al. (2008) including a silicate melt compositional term in the form of nbo/t. The resulting model M3 shows a solution domain that include all four elements W, Ni, Co, and Mo.

This solution domain extends from approximately 2600 to 3100 K and 35 to 39 GPa (Figure 44). This domain intersects the peridotite liquidus essentially at a point where the pressure is approximately 38 GPa at a temperature of 3100 K. Comparing this result to M2, it is clear that including the silicate melt compositional term for Ni and Co had an effect on the solution domains, mainly in the pressure region of overlap. Another region of overlap exists just above the Fiquet et al. (2010) liquidus at approximately 35 GPa and 3600 K that includes Ni, Co, and Mo, but not W.

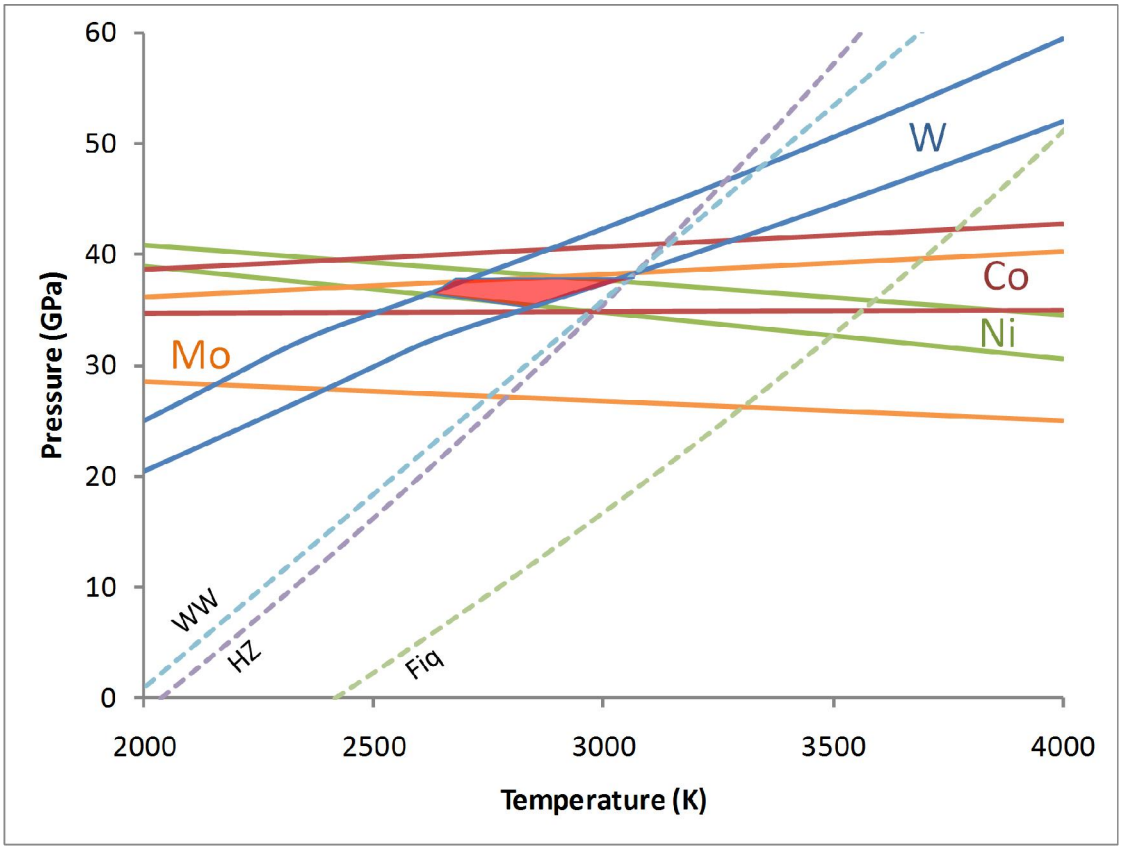

Figure 44. Model M3 for constraining equilibrium core formation conditions. The pairs of same-colored lines are bounds on the P-T conditions that satisfy the D value for the indicated element in the modern Earth (matches core/mantle abundances). The red polygon is a region where elements overlap, indicating the solution, 35-39 GPa and 2600-3100 K. Calculations for elements based on: W using R4 in this study; Ni and Co from Righter (2011); and Mo from Siebert et al. (2011). Multiple models of the peridotite liquidus are shown as dashed lines for reference: WW = Wade and Wood (2005); HZ = 2nd-order fit of Herzberg and Zhang (1996) and Zerr et al. (1998) data; and Fiq = Fiquet et al. (2010).

Comparing the solutions from models M1, M2, and M3, all give solutions above the Wade and Wood (2005) peridotite liquidus at approximately the same temperature and slightly differing pressures. Only M3 gave a solution that included all four elements used in the models, W, Ni, Co, and Mo. This makes M3 the most compelling solution at 38 GPa and 3100 K.

5.3 Implications of Models

The solutions derived from the models in section 5.2 provide constraint on the P-T-X-fO_2 conditions of core formation, which can be compared with previous studies that have used the same, simplified view of a single P-T condition of core formation. Using the same four elements, Righter (2011) reports a pressure of 44 GPa and a temperature range of 3100 to 3400 K at an fO_2 of IW-1.5. Siebert et al. (2011) find a solution of 32 to 42 GPa and 3000 to 3200 K at an fO_2 of IW-2, which is based on seven elements Ni, Co, W, Mo, Cr, Zn, and Mn.

Exactly what these P-T solution means in terms of the physical process of core formation is a matter of debate. The segregation of the Earth's core likely began early in the planetary formation process and so the conditions under which metal-silicate partitioning changed over time. Therefore, the solutions may represent an averaged effect of the changing conditions over the entire period of core formation(Wood, 2008; Rubie et al., 2011; Siebert et al., 2011; Righter, 2011). Or they may represent most strongly the latest stage of core formation. Which of these is more correct depends largely on the magnitude of the contribution of the various parameters to partitioning for the individual elements. For instance, if pressure is a dominant parameter controlling metal/silicate partitioning, then the later stages of core formation are most

relevant due to greater depth of the core-mantle boundary with time. Using multiple elements with differing pressure dependencies such as the group of elements employed here aids in constraining the effect of varying pressure during Earth accretion and core formation. Some argue that determining a single P-T value for core formation is ambiguous because of the complex process of planetary accretion (Wade and Wood, 2005; Wood, 2008; Rubie et al., 2011). It has become common for this type of model to be termed 'single stage', implying that Earth's core formed in a single event (Rubie et al., 2011; Siebert et al., 2011). A popular approach in recent years has been to model Earth accretion and core formation in so-called continuous core formation models and these are held as more realistic and the results as more meaningful than the simple P-T solutions (Wade and Wood, 2005; Wood, 2008; Rubie et al., 2011). Many of the assumptions made in such models, however, do not provide unique solutions, and the arbitrary choices such as progressively increasing oxygen fugacity to make abundances of certain elements in the model fit, do not offer any more certainty in terms a definitive assessment of what caused the current distribution of elements between core and mantle (Righter, 2011).

The prevailing view is that Earth's moon was formed by a massive impact from a large impactor (Canup, 2008; Chambers, 2003). This is thought to have resulted in a final, large-scale, magma ocean on the Earth which may have consisted of complete melting of the mantle. Also, materials from the impacting body were added to the Earth. The combined effect of these is that the signature of differentiation expressed in the distribution of elements between mantle and core prior to this impact may have been effectively reset (Stevenson, 2008). The end result being that the modern core and

mantle abundances of siderophile elements represents the conditions following the moon-forming impact and the influence of any materials accreted by this impact. The simplicity of the single P-T solution is that it treats the problem in a mostly path-independent way and seeks to answer question of what conditions were present during core formation. It is likely that a combination of modeling approaches will be necessary to ultimately explain how the Earth's core formed in terms of specific processes and events. The current results then are one piece of a complicated puzzle.

6 Conclusions

The goals of this project have been achieved. The proposed research was to expand previous knowledge of the behavior of W at high pressures and temperatures through experimentation. The metal/silicate partitioning data set has been extended to pressures more than twice the previously studied maximum. Parameterization of these data along with previous literature data has resulted in improved constraints on the pressure, temperature, and compositional effects on W metal/silicate partitioning. Knowledge of the redox behavior of the W-WO_2 equilibrium at high pressures and temperatures has been greatly improved. In particular, the structure of WO_2 has been studied at conditions not previously explored. A new crystal structure has been identified at high pressure, though atomic coordinates have not been refined (this will require single crystal diffraction studies). Using this information, the W-WO_2 oxygen fugacity buffer has been extended to high pressure, and has been combined with the high pressure metal/silicate partitioning data to give a more thermodynamically robust expression of W metal/silicate partitioning (R4) compared to the linear approaches in common use, and therefore its extrapolation is expected to be more accurate. Additionally, the WWO buffer is also now more suitable for application in high pressure experiments, both as an alternative means to control experimental fO_2 but also as an alternative means to calculate experimental fO_2 especially in conditions where the IW buffer cannot be used such as Fe-free systems.

Application of both the linear and non-linear parameterizations of W to the problem of constraining core formation conditions in the Earth has produced similar,

meaningful results. Combined with parameterizations for other elements has given P-T solutions for an equilibrium core formation in the Earth that is in agreement with other studies employing different parameterizations.

My null hypothesis was that W metal/silicate partitioning was insensitive to pressure at pressures greater than those previously experimentally explored. The test of this hypothesis was that W metal/silicate partitioning as described by a partition coefficient should not vary outside of uncertainties, either analytical or the uncertainty of a parameterized fit. Calculation of the Fe-W exchange coefficient along isotherms using both the linear and non-linear parameterizations shows variations ranging from one to three log units across a pressure range of 60 GPa. This level of variation is significantly greater than the fit uncertainties which are on the order 0.2 log units. Therefore, I reject the null hypothesis. I find that the siderophility of W does decrease with increasing pressure. This finding is in agreement with previous predictions based on lower pressure data, though now based on experimental constraints. Examination of the WWO buffer relative to the IW buffer likewise predicts a decreased siderophility at high pressures. In fact, the pressure range where the WWO buffer approaches the IW buffer is in the vicinity of the predicted core formation pressure determined using the W parameterizations in this study and parameterizations for Ni, Co, and Mo determined by others.

As a result of the investigations in the work, I have pushed metal-silicate partitioning studies to great pressures and temperatures, especially in the diamond anvil cell. The use of diamond cells in experimental petrologic studies of this type is cutting edge research, and the refinements of experimental methods and compositional analysis

will benefit this growing and promising field of study. Future work on W would benefit from further metal/silicate experimentation to better control the experimental temperatures, and to limit the amount of carbon dissolved in the metals. The high pressure crystallography of tungsten oxides deserves further study as well to better refine the identified high pressure phase and to study the complicated phase assemblages present at high temperatures.

Appendices

Appendix A: Additional LHDAC Sample Images

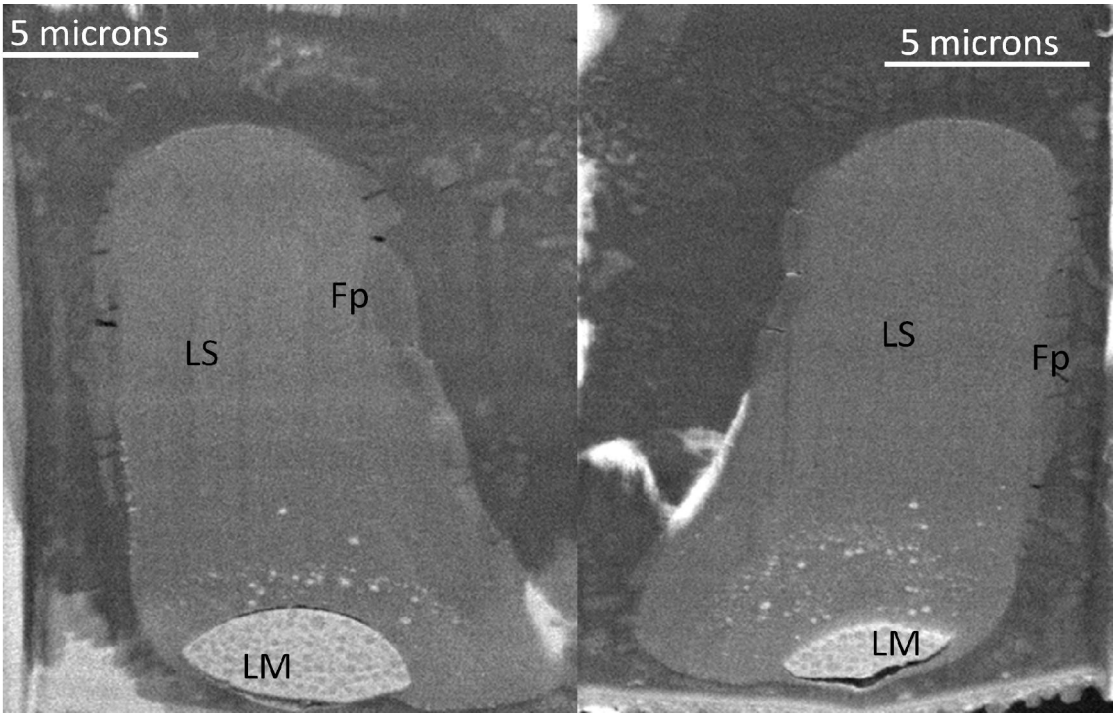

Figure A-1. Backscattered electron images showing obverse sides of LHDAC sample G34, sectioned by FIB. Section thickness is approximately 1 micron. LS – quenched silicate liquid, LM – quenched metallic alloy liquid, and Fp = ferropericlase.

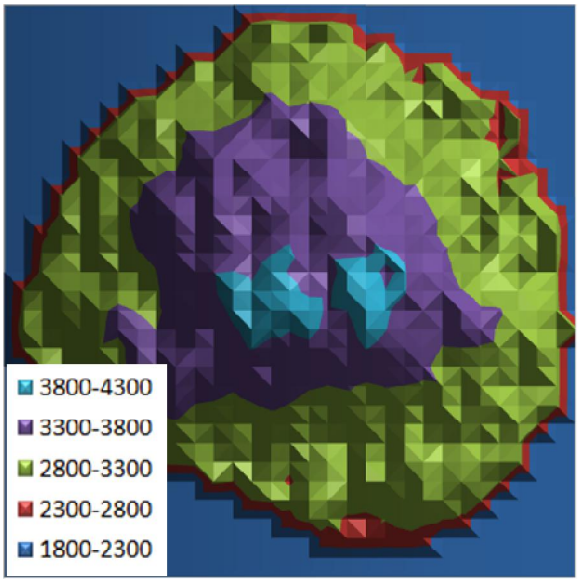

Figure A-2. Temperature map of sample G34 showing radial temperature distribution. The highest temperature region (3800 – 4300 K) corresponds to the quenched metallic alloy liquid shown in the BSE images of Figure A-1. Temperature ranges are in Kelvins.

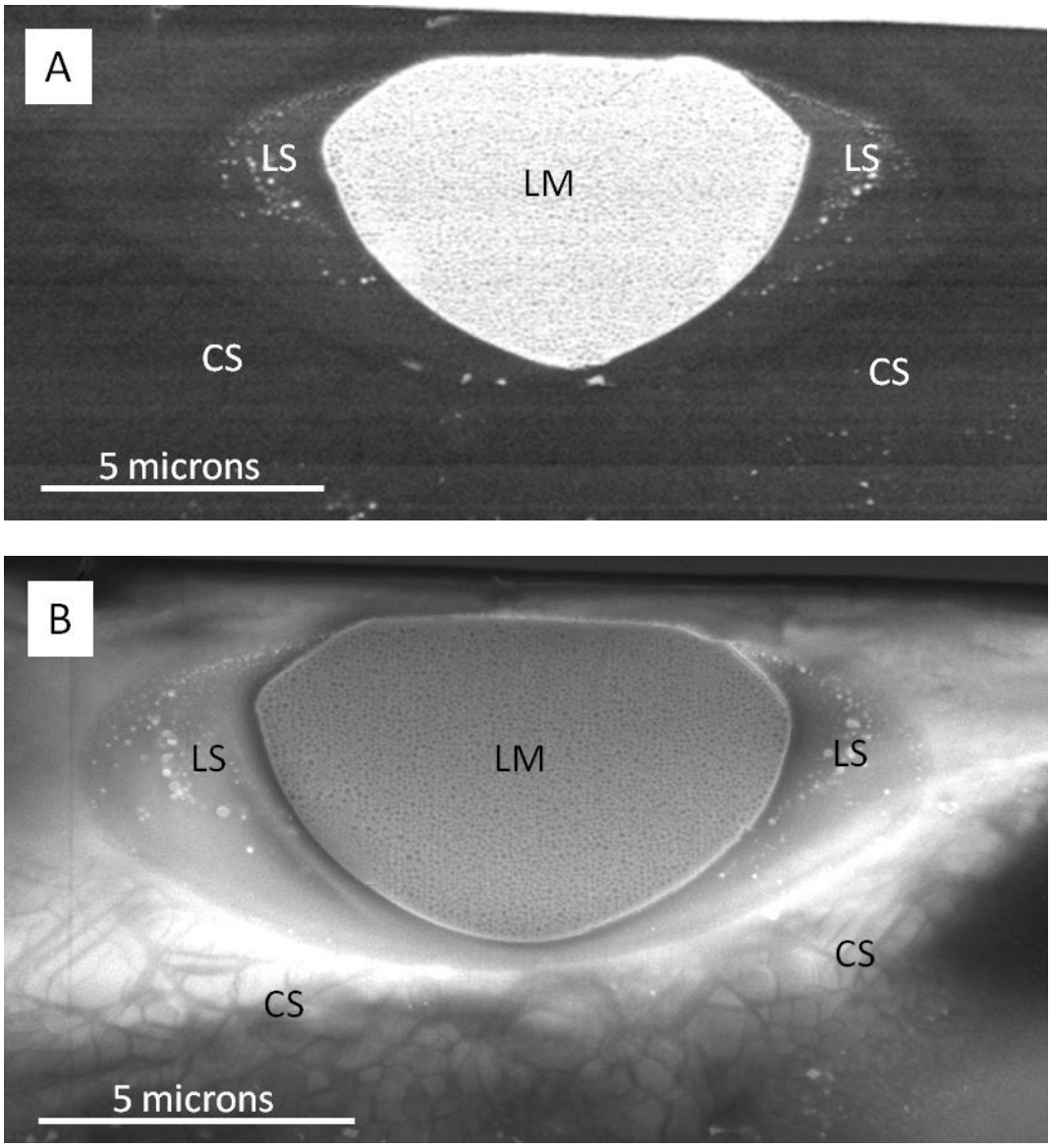

Figure A-3. Backscattered electron (A) and secondary electron (B) images of LHDAC sample G38a, sectioned by FIB. Section thickness is approximately 1 micron. LS – quenched silicate liquid, LM – quenched metallic alloy liquid, and CS – crystalline silicate.

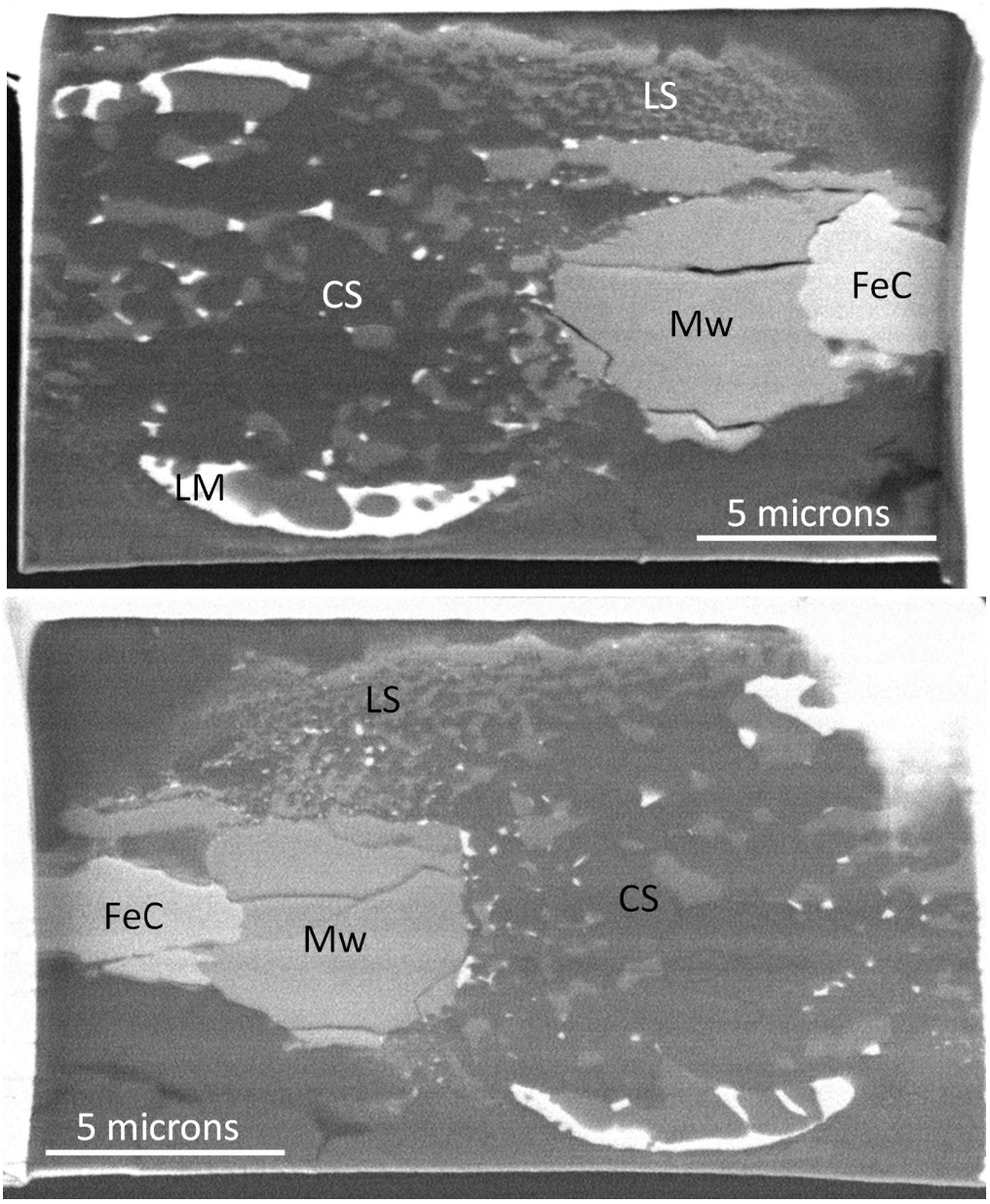

Figure A-4. Backscattered electron images showing observe sides of LHDAC sample G38b. Section thickness is approximately 1 micron. LS – quenched silicate liquid, Mw – magnesiowüstite, FeC – iron carbide, CS – crystalline silicate, and LM – quenched metallic liquid.

References

Arevalo, R., and McDonough, W.F., 2003. Tungsten geochemistry and implications for understanding the Earth's interior. Earth Planet. Sci. Lett. 272, 656-665.

Armstrong, J.T., 1995. CITZAF: A Package of correction programs for the quantitative electron microbeam x-ray analysis of thick polished materials, thin films, and particles. Microbeam Analysis 4, 177-200.

Auzende, A-L., Badro, J., Ryerson, F.J., Weber, P.K., Fallon, S.J., Addad, A., Siebert, J., and Fiquet, G., 2008. Element partitioning between magnesium silicate perovoskite and ferropericlase: New insights into bulk lower-mantle geochemistry. Earth Planet. Sci. Lett. 269, 164 – 174.

Beattie, P., Drake, M., Jones, J., Leeman, W., Longhi, J. Mckay, G., Nielsen, R., Palme, H., Shaw, D., Takahashi, E., and Watson, B., 1993. Terminology for trace element partitioning. Geochim. Cosmochim. Acta 57 (7), 1605 – 1606.

Birch. F., 1952. Elasticity and constitution of the Earth's interior. J. Geophys. Res. 57 (2), 227 – 286.

Boultif, A., and Louer, D., 2004. Powder pattern indexing with the dichotomy method. J. Appl. Cryst. 37, 724 – 731.

Bolzan, A.A., Kennedy, B.J, and Howard, C.J, 1995. Neutron powder diffraction study of molybdenum and tungsten dioxides. Aust. J. Chem. 48, 1473-1477.

Bottke, W.F., Walker, R.J., Day, J.M.D., Nesvorny, D., and Elkins-Tanton, L., 2010. Stochastic late accretion to Earth, the Moon, and Mars. Science, 330, 1527-1530.

Bouvier, P., Crichton, W.A., Boulova, M., and Lucazeau, G., 2002. X-ray diffraction study of WO_3 at high pressure. J. Condens. Matter 14, 6605-6617.

Campbell, A.J, 2008. Measurement of temperature distributions across laser heated samples by multispectral imaging radiometry. Rev. Sci. Instr. 79, 015108.

Campbell, A.J, Danielson, L., Righter, K., Seagle, C.T., Wang, Y., and Prakapenka, V.B., 2009. High pressure effects on the iron-iron oxide and nickel-nickel oxide oxygen fugacity buffers. Earth Planet. Sci. Lett. 286, 556 – 564.

Canup, R.M., 2008. Accretion of the Earth. Phil. Trans. R. Soc. A 366, 4061-4075.

Chabot, N.L., and Drake, M.J., 1997. An experimental study of silver and platinum partitioning between solid and liquid metal, with applications to iron meteorites. Meteor. and Planet. Sci. 32, 637-645.

Chambers, J.E., 2003. Planet formation. In: A.M. Davis (Ed.), Meteorites, Comets, and Planets, Treatise on Geochemistry Vol 1, Elsevier-Pergamon, Oxford, 461-475.

Capobianco, C.J., Jones, J.H., and Drake, M.J., 1993. Metal-silicate thermochemistry at high temperature: magma oceans and the "excess siderophile element" problem of the Earth's upper mantle. J. Geophys. Res. 98 (E3), 5433 – 5443.

Chabot, N.L., and Agee, C.B., 2003. Core formation in the Earth and Moon: new experimental constraints from V, Cr, and Mn. Geochim. Cosmochim. Acta 67 (11) 2077-2091.

Chabot, N.L., Draper, D.S., and Agee, C.B., 2005. Conditions of core formation in the Earth: contraints from Nickel and Cobalt partitioning. Geochim. Cosmochim. Acta 69 (8), 2141-2151.

Corgne, A., Keshav, S., Wood, B., McDonough, W.F., and Fei, Y., 2008. Metal-silicate partitioning and constraints on core composition and oxygen fugacity during Earth accretion. Geochim. Cosmochim. Acta 72, 574-589.

Cottrell, E., Walter, M.J., and Walker, D., 2009. Metal–silicate partitioning of tungsten at high pressure and temperature: implications for equilibrium core formation in Earth. Earth Planet. Sci. Lett. 281, 275-287.

Danielson, L.R., Righter, K., Sutton, S., Newville, M., and Le, L., 2008. L-edge XANES measurements of the oxidation state of tungsten in iron bearing and iron free silicate glasses. 39th Lunar Planet. Sci. Conf., Abstract 2075.

Decker, D.L., 1971. High-pressure equation of state for NaCl, KCl, and CsCl. J. Appl. Phys. 42(8), 3239.

de Levie, R., 2008. Advanced Excel for scientific data analysis, 2nd ed., Oxford University Press.

Dorogokupets, P.I., and Oganov, A.R., 2007. Ruby, metals, and MgO as alternative pressure scales: a semiempirical description of shock-wave, ultrasonic, x-ray, and thermochemical data at high temperatures and pressures. Phys. Rev. B. 75, 024115.

Drake, M.J., 2000. Accretion and primary differentiation of the Earth: a personal journey. Geochim. Cosmochim. Acta 64 (14), 2363 – 2370.

Ertel, W., O'Neill, H.St.C., Dingwell, D.B., and Spettel, B., 1996. Solubility of tungsten in a haploblastic melt as a function of temperature and oxygen fugacity. Geochim. Cosmochim. Acta 60 (7), 1171-1180.

Fei, Y., Ricolleau, A., Frank, M., Mibe, K., Shen, G., and Prakapenka, V., 2007. Toward an internally consistent pressure scale. Proc. Natl. Acad. Sci. 104 (22), 9182 – 8186.

Halliday, A.N., 2003. The origin and earliest history of the Earth. In: Davis A.M. (Ed.), Meteorites, Comets and Planets: Treatise on Geochemistry Vol 1, 509 – 557.

Hammersley, A.P., Svensson, S.O., Hanfland, M., Fitch, A.N., and Häusermann, D., 1996. Two-dimensional detector software: from real detector to idealised image or two-theta scan. High Pressure Res. 14, 235 – 248.

Heinz, D.L., and Jeanloz, R., 1984. Compression of the B2 high-pressure phase of NaCl. Phys. Rev. B. 30 (10), 6045-6050.

Heinz, D.L., and Jeanloz, R., 1987. Temperature measurements in the laser-heated diamond cell. In: Manghnani, M.H., and Y. Syono (Eds.), High-Pressure Research in Mineral Physics, Geophysical Monograph 29, Mineral Physics 2, American Geophysical Union, Washington, D.C.

Herzberg, H., and Zhang, J., 1996. Compositions of magma in the upper mantle and transition zone. J. Geophys. Res. 101 (B4), 8271-8295.

Hillgren, V.J., Drake, M.J., and Rubie, D.C., 1996. High-pressure and high-temperature metal-silicate partitioning of siderophile elements: the importance of silicate liquid composition. Geochim. Cosmochim. Acta 60 (12), 2257 – 2263.

Irfune, T., Isshiki, M., and Sakamoto, S., 2005. Transmission electron microscope observation of the high-pressure form of magnesite retrieved from laser heated diamond anvil cell. Earth Planet. Sci. Lett. 239, 98 – 105.

Jacobsen, S.B., 2005. The Hf-W isotopic system and the origin of the Earth and Moon. Ann. Rev. Earth Planet. Sci. 33, 531 – 570.

Jaeger, W.L., and Drake, M.J., 2000. Metal-silicate partitioning of Ca, Ga, and W, dependence on silicate melt. Geochim. Cosmochim. Acta 64 (22), 3887 – 3895.

Jana, D., and Walker, D., 1997. The influence of sulfur on partitioning of siderophile elements. Geochim. Cosmochim. Acta 61 (24), 5255-5277.

Jones, J.H., and Drake, M.J, 1986. Geochemical constraints on core formation in the Earth. Nature 322, 221 – 228.

Kiefer, B., and Duffy, T.S., 2005. Finite element simulations of the laser-heated diamond anvil cell. J. Appl. Phys. 97, 114902.

Lasdon, L.S., and Warren, A.D., 1978. Generalized reduced gradient software for linearly and nonlinearly constrained problems. In: H.J. Greenberg (Ed.) Design and Implementation of Optimization Software. Sijthoff and Noordhoff, Holland, 335-362.

Lee, D.C. and Halliday, A.N., 1995. Hafnium-Tungsten chronometry and the timing of terrestrial core formation. Nature 378 (6559), 771 – 774.

Leinenweber, K., 2005. Designing multi-anvil assemblies: The COMPRES cell assembly project. GSECARS Multi-Anvil Workshop presentation. http://gsecars.org/LVP/LVP_workshop_05/Prensetations/Kurt_Designing multi-anvil assemblies.ppt, Slide #26.

Li, J., and Agee, C.B., 1996. Geochemistry of mantle-core differentiation at high pressure. Nature 381, 686 – 689.

Lyubetskaya, T., and Korenaga, J., 2007. Chemical composition of Earth's primitive mantle and its variance. J. Geophys. Res. 112, B03211.

Ma, Z., 2001. Thermodynamic description for concentrated metallic solutions using interaction parameters. Metal. Mat. Trans. 32B, 87-103.

Mann, U., Frost, D.J., and Rubie, D.C., 2009. Evidence for high-pressure core-mantle differentiation from the metal-silicate partitioning of lithophile and weakly-siderophile elements, Geochim. Cosmochim. Acta 73, 7360 – 7386.

Mao, H.K., Xu, J., and Bell, P.M., 1986. Calibration of the ruby pressure gauge to 800 kbar under quasihydrostatic conditions. J. Geophys. Res. 91, 4673-4676.

McDonough, W.F., and Sun, S.-s., 1995. The composition of the Earth. Chem. Geol. 120, 223 – 253.

McDonough, W.F., 2003. Compositional model for the Earth's core. In: R. W. Carlson (Ed.), The Mantle and Core, Treatise on Geochemistry Vol 2, Elsevier-Pergamon, Oxford, 547 – 568.

Miyahara, M., Sakai, T., Ohtani, E., Kobayashi, Y., Kamada, S., Kondo, T., Nagase, T., Yoo. J.H., Nishijima, M, and Vashaei, Z., 2008. Application of FIB system to ultra-high-pressure Earth science. J. Min. Pet. Sci. 103, 88 – 93.

Mysen, B.O., 1983. The structure of silicate melts. Ann. Rev. Earth Planet. Sci. 11, 75-97.

Ohtani, E., Yurimoto, H., and Seto, S., 1997. Element partitioning between metallic liquid, silicate liquid, and lower-mantle minerals: implications for the core formation of the Earth. Phys. Earth Planet. Int. 100, 97 – 114.

O'Neill, H.St.C., 1998. Oxide-metal equilibria to 2500ºC and 25 GPa: implications for core formation and the light component in the Earth's core. J. Geophys. Res. 103 (B6), 12239-12260.

O'Neill, H.St.C, and Eggins, S.M., 2002. The effect of melt composition on trace element partitioning: an experimental investigation of the activity coefficients of FeO, NiO, CoO, MoO_2 and MoO_3 in silicate melts. Chem. Geol. 186, 151-181.

O'Neill, H.St.C, and Pownceby, M.I., 1993. Thermodynamic data from redox reaction at high temperatures. I. An experimental and theoretical assessment of the electrochemical method using stabilized zirconia electrolytes, with revised values

for the Fe-"FeO", Co-CoO, Ni-NiO, and Cu-Cu_2O oxygen buffers, and new data for the W-WO_2 buffer. Contrib. Min. Petrol. 114, 296-314.

O'Neill, H.St.C, Berry, H.J., and Eggins, S.M., 2008. The solubility and oxidation state of tungsten in silicate melts: implications for the comparative chemistry of W and Mo in planetary differentiation processes. Chem. Geol. 255, 346 – 359.

Pecharsky, V.K., and Zavalij, P.Y., 2009. Fundamentals of Powder Diffraction and Structural Characaterization of Materials, 2nd Edition. Springer. ISBN 978-0-387-09578-3.

Ricolleau, A., Fiquet, G., Addad, A., Menguy, N., Vanni, C., Perrillat, J-P., Daniel, I., Cardon, H., and Guignot, N., 2008. Analytical transmission electron microscopy of a natural MORB sample assemblage transformed at high pressure and high temperature. Am. Min. 93, 144 – 153.

Righter, K., and Drake, M.J., 1996. Core formation in the Earth's Moon, Mars, and Vesta. Icarus 124, 513 – 529.

Righter, K., and Drake, M.J., 1999. Effect of water on metal-silicate partitioning of siderophile elements, a high pressure and temperature terrestrial magma ocean and core formation. Earth Planet. Sci. Lett. 171, 383 – 399.

Righter, K., 2003. Metal-silicate partitioning of siderophile elements and core formation in the early Earth. Ann. Rev. Earth Planet. Sci. 31, 135 – 174.

Righter, K., 2011. Prediction of metal-silicate partition coefficients for siderophile elements: An update and assessment of PT conditions for metal-silicate equilibrium during accretion of the Earth. Earth Planet. Sci. Lett. 304, 158-167.

Righter, K., and Shearer, C.K., 2003. Magmatic fractionation of Hf and W: Constraints on the timing of core formation and differentiation in the Moon and Mars. Geochim. Cosmochim. Acta, 67 (13), 2497 – 2507.

Ringwood, A.E., 1966. Chemical evolution of the terrestrial planets. Geochim. Cosmochim. Acta 30, 41 – 104.

Rubie, D.C., Melosh, H.J., Reid, J.E., Liebske, C., and Righter, K., 2003. Mechanisms of metal-silicate equilibration in the terrestrial magma ocean. Earth Planet. Sci. Lett. 205, 239 – 255.

Rubie, D.C., Gessmann, C.K., and Frost, D.J., 2004. Partitioning of oxygen during core formation on the Earth and Mars. Nature 429, 58 – 61.

Rubie, D.C., Frost, D.J., Mann, U., Asahara, Y., Nimmo, F., Tsuno, K., Kegler, P., Holzheid, A., and Palme, H., 2011. Heterogeneous accretion, composition and core-mantle differentiation of the Earth. Earth Planet. Sci. Lett. 301, 31 – 42.

Rudnick, R.L., Gao, S., Ling, W., Liu, Y., and McDonough, W.F., 2004. Petrology and geochemistiry of spinel peridotite xenoliths from the Hannuoba and Qixia, North China craton. Lithos 77, 609 – 637.

Sanloup, C., van Westrenen, W., Dasgupta, R., Maynard-Casely, H., Perrillat, J.P., 2011. Compressibility change in iron-rich melt and implications for core formation models. Earth and Planetary Science Letters 306, 118-122.

Schoenberg, R., Kamber, B.S., Collerson, K.D., And Eugster, O., 2002. New W-isotope evidence for rapid terrestrial accretion and very early core formation. Geochim. Cosmochim. Acta, 66 (17), 3151 – 3160.

Shen, G., Rivers, M., Wang, Y., and Sutton, S., 2001. Laser heated diamond cell system at the Advanced Photon Source for in situ x-ray measurements at high pressure and temperature. Rev. Sci. Instr. 72 (2), 1273-1282.

Siebert, J., Corgne, A., and Ryerson, F.J., 2011. Systematics of metal-silicate partitioning for many siderophile elements applied to Earth's core formation. Geochim. Cosmochim. Acta 75, 1451-1489.

Speziale, S., Zha, C-S., Duffer, T.S, 2001. Quasi-hydrostatic compression of magnesium oxide to 52 GPa: implications for the pressure-volume-temperature equation of state. J. Geophys. Res. 106 (B1), 515-528.

Sundberg, M., Werner, P.-E., and Zibrov, I.P, 1994. X-ray powder crystal structure analysis of high pressure tungsten dioxide, on the information in weak reflections. Zeits. für Kristal. 209, 662-666.

Stevenson, D.J., 1981. Models of the Earth's core. Science 214 (4521), 611 – 619.

Stevenson, D.J., 1990. Fluid dynamics of core formation. In: Newsom, H.E. and Jones, J.H. (Eds.), Origin of the Earth, Oxford University Press, New York, 231 – 250.

Stevenson, D.J., 2008. A planetary perspective on the deep Earth. Nature 451, 261 – 265.

The Japan Society for the Promotion of Science and The Nineteenth Committee on Steelmaking, 1988. Part 2: Recommended values of activity and activity coefficients, and interaction parameters of elements in iron alloys. In: Steelmaking Data Sourcebook, Gordon and Breach Science Publishers, New York, 273–297.

Thibault, Y., and Walter, M., 1995. The influence of pressure and temperature on the metal-silicate partition coefficients of nickel and cobalt in a model C1 chondrite and implications for metal segregation in a deep magma ocean. Geochim. Cosmochem. Acta 59 (5), 991-1002.

Vockenhuber, C., Oberli, F., Bichler, M., Ahmad, I., Quitté, G., Meier, M., Halliday, A. N., Lee, D.-C., Kutschera, W., Steier, P., Gehrke, R. J., and Helmer, R. G.,

2004. New half-life measurement of 182Hf: improved chronometer for the early solar system. Phys. Rev. Lett. 93 (17), 172501.

Wade, J., and Wood, B.J., 2005. Core formation and the oxidation state of the Earth. Earth Planet. Sci. Lett. 236, 75 – 95.

Walker, R.J., 2008. Highly siderophile elements in the Earth, Moon, and Mars: update and implications for planetary accretion and differentiation. Chem. der Erde Geochem. 69, 101 – 125.

Walter, M.J., Newsom, H.E., Ertel, W., and Holzheid, A., 2000. Siderophile elements in the Earth and Moon: metal/silicate partitioning and implications for core formation. In: Canup, R.M. and Righter, K. (Eds.), Origin of the Earth and Moon, University of Arizona Press, USA, 265 – 288.

Walter, M.J., and Thibault, Y., 1995. Partitioning of Tungsten and Molybdenum between metallic liquid and silicate melt. Science 270 (5239), 1186 – 1189.

Walter, M.J. and Trønnes, R.G., 2004. Early Earth differentiation. Earth Planet. Sci. Lett. 225, 253 – 269.

Wänke, H., and Dreibus, G., 1988. Chemical composition and accretion history of terrestrial planets. Phil. Trans. R. Soc. 325 (1587), 545 – 557.

Wänke, H., and Gold, T., 1981. Constitution of terrestrial planets [and discussion]. Phil. Trans. R. Soc. 303 (1477), 287 – 302.

Williams, Q., and Jeanloz, R., 1998 Spectroscopic evidence for pressure-induced coordination changes in silicate glasses and melts. Science 239 (4842), 902-905.

Wood, B.J., 2008. Accretion and core formation: constraints from metal-silicate partitioning. Phil. Trans. Royal. Soc. 366, 4339 – 4355.

Zerr, A., Diegeler, A., and Boehler, R., 1998. Solidus of Earth's deep mantle. Science 281, 243 – 246.